

Search for the rare decay  $K^+ \rightarrow \pi^+ \nu \bar{\nu}$   
with  $p_{\pi^+} < 199 \text{ MeV}/c$

A Dissertation Presented

by

Ilektra-Athanasia Christidi

to

The Graduate School

in Partial fulfillment of the

Requirements

for the Degree of

Doctor of Philosophy

in

Physics

Stony Brook University

December 2006

Stony Brook University

The Graduate School

Ilektra-Athanasia Christidi

We, the dissertation committee for the above candidate for the Doctor of Philosophy degree, hereby recommend acceptance of this dissertation.

---

Michael D. Marx

Professor, Department of Physics, Stony Brook University  
Dissertation Director

---

Robert Shrock

Professor, Department of Physics, Stony Brook University  
Chairman of Dissertation

---

Gene D. Sprouse

Professor, Department of Physics, Stony Brook University

---

David E. Jaffe

Physicist, Physics Department, Brookhaven National Laboratory  
Outside Member

---

Laurence S. Littenberg

Physicist, Physics Department, Brookhaven National Laboratory  
Outside Member

This dissertation is accepted by the Graduate School.

---

Dean of the Graduate School

Abstract of the Dissertation

Search for the rare decay  $K^+ \rightarrow \pi^+ \nu \bar{\nu}$   
with  $p_{\pi^+} < 199 MeV/c$

by

Ilektra-Athanasia Christidi

Doctor of Philosophy

in

Physics

Stony Brook University

2006

The rare Kaon decay  $K^+ \rightarrow \pi^+ \nu \bar{\nu}$  is a valuable probe for the flavor structure of the Standard Model (SM) and for new physics. In the SM, its Branching Ratio (BR) is of the order of  $10^{-10}$  and depends on the magnitude of the  $V_{td}$  element of the CKM matrix, which modulates the strength of the charged current coupling between the top and down quark and includes the imaginary phase of the matrix. This phase is the only significant source of CP violation in the SM, given that the strong CP phase must be very small. This rare decay is being searched for by the experiment E949 at

BNL's Alternating Gradient Synchrotron in two kinematic regions, "PNN1" with  $211\text{MeV}/c < p_{\pi^+} < 229\text{MeV}/c$  and "PNN2" with  $p_{\pi^+} < 199\text{MeV}/c$ . This thesis describes the analysis of the PNN2 region. A "blind analysis" approach is taken, in which the expected backgrounds are determined a priori. In order to avoid bias, selection criteria ("cuts") to suppress the backgrounds are developed based on 1/3 of the data, uniformly selected throughout the total sample. During this process, potential signal events (any events in the multidimensional signal region defined by these cuts) are masked out. Then the expected background in the signal region is measured with data, using the final version of the cuts in a bifurcated analysis, and verified by examining the number of events close to (but still outside of) the signal region. For some background processes that are difficult to distinguish in real data, Monte Carlo simulation is used. The expected background level found in this analysis is  $0.630 \pm 0.119$  events, an improvement of a factor of 2 compared to previous analyses. Finally the acceptance loss of the offline cuts and the online trigger is measured using special background samples of data and signal simulation, and the single event sensitivity (S.E.S.) is calculated to be  $1.019 \times 10^{-9}$ . The S.E.S. is the lowest BR for the  $K^+ \rightarrow \pi^+ \nu \bar{\nu}$  decay that this analysis can detect, in the absence of background. Using the BR measured by E949 in the past, the expected ratio of signal to background in the signal region is about 1/5, a significant improvement compared to the value of previous analyses of 1/10.

# Contents

|   |            |
|---|------------|
| <b>List of Figures</b>  | <b>xx</b>  |
| <b>Acknowledgements</b>   | <b>xxi</b> |
| <b>1 Introduction</b>   | <b>1</b>   |
| <b>2 Theory</b>   | <b>4</b>   |
| 2.1 CP violation in the Standard Model . . . . .                          | 5          |
| 2.2 $K^+ \rightarrow \pi^+ \nu \bar{\nu}$ in the Standard Model . . . . . | 12         |
| 2.3 Physics beyond the Standard Model . . . . .                           | 17         |
| <b>3 The experiment</b>   | <b>20</b>  |
| 3.1 Experimental Overview . . . . .                                       | 20         |
| 3.2 The beam . . . . .  | 26         |
| 3.3 The detector . . . . .  | 28         |
| 3.3.1 Beam detectors . . . . .  | 30         |
| 3.3.2 Target (TG) . . . . .   | 36         |
| 3.3.3 Drift Chamber (UTC) . . . . .                                       | 38         |
| 3.3.4 Range Stack (RS) . . . . .  | 40         |

|          |  |           |
|----------|--|-----------|
| 3.3.5    | Photon Veto . . . . .  | 45        |
| 3.4      | Trigger . . . . .  | 49        |
| 3.5      | Monte Carlo Simulation (UMC) . . . . .                       | 54        |
| 3.6      | Summary of 2002 Data Taking . . . . .                        | 55        |
| <b>4</b> | <b>Analysis overview</b>                                     | <b>58</b> |
| 4.1      | Event Reconstruction . . . . .                               | 58        |
| 4.2      | Background overview . . . . .                                | 67        |
| 4.3      | Analysis technique . . . . .                                 | 72        |
| 4.3.1    | Background estimation from data . . . . .                    | 72        |
| 4.3.2    | Validity checks: outside-the-box study . . . . .             | 75        |
| 4.3.3    | Acceptance measurement . . . . .                             | 75        |
| <b>5</b> | <b>Background estimation</b>                                 | <b>80</b> |
| 5.1      | $K^+ \rightarrow \pi^+ \pi^0$ Target scatters . . . . .      | 80        |
| 5.2      | $K^+ \rightarrow \pi^+ \pi^0$ Range Stack scatters . . . . . | 86        |
| 5.3      | Beam background . . . . .                                    | 88        |
| 5.3.1    | Single beam . . . . .  | 88        |
| 5.3.2    | Double beam . . . . .  | 91        |
| 5.3.3    | Total beam background . . . . .                              | 95        |
| 5.4      | Muon backgrounds . . . . .                                   | 95        |
| 5.5      | $K^+ \rightarrow \pi^+ \pi^- e^+ \nu$ background . . . . .   | 96        |
| 5.5.1    | Background estimate using data . . . . .                     | 98        |
| 5.5.2    | Background study with UMC . . . . .                          | 99        |
| 5.6      | $K^+ \rightarrow \pi^+ \pi^0 \gamma$ . . . . .               | 103       |
| 5.7      | Charge Exchange (CEX) background . . . . .                   | 107       |

|          |   |            |
|----------|---|------------|
| 5.8      | Background summary . . . . .  | 109        |
| 5.9      | Outside-the-box study . . . . .   | 110        |
| <b>6</b> | <b>Acceptance measurement</b>   | <b>112</b> |
| 6.1      | $K_{\mu 2}$ based acceptance . . . . .  | 112        |
| 6.2      | $\pi_{scat}$ based acceptance . . . . .                                       | 116        |
| 6.2.1    | Kinematic and reconstruction acceptance . . . . .                             | 117        |
| 6.2.2    | TD acceptance . . . . .   | 118        |
| 6.3      | $K_{\pi 2}$ based acceptance . . . . .  | 121        |
| 6.4      | UMC based acceptance . . . . .  | 122        |
| 6.5      | $T \cdot 2$ efficiency . . . . .  | 125        |
| 6.6      | Acceptance summary and Single Event Sensitivity (S.E.S.) . .                  | 127        |
| <b>7</b> | <b>Conclusion</b>   | <b>128</b> |
| <b>8</b> | <b>Appendix</b>   | <b>130</b> |
| A        | Analysis cuts . . . . .   | 130        |
| A.1      | PASS1 level . . . . .   | 130        |
| A.2      | PASS2 level . . . . .   | 132        |
| A.3      | Kinematic Cuts (KCUT) . . . . .   | 134        |
| A.4      | Beam Cuts (PSCUT06) . . . . .   | 138        |
| A.5      | Target Quality Cuts (TGCUT06) . . . . .                                       | 142        |
| A.6      | $\pi^+ \rightarrow \mu^+ \rightarrow e^+$ Decay Sequence Cuts (TDCUT02) . . . | 150        |
| A.7      | Photon Veto Cuts (PVCUTPNN2) . . . . .  | 152        |
| B        | The $\pi\nu\bar{\nu}(2)$ Photon Veto . . . . .                                | 154        |
| B.1      | Choosing the cuts . . . . .   | 154        |

|     |   |            |
|-----|---|------------|
| B.2 | Limits of the Photon Veto rejection . . . . . | 156        |
| C   | The Active Degradar . . . . .                 | 165        |
| C.1 | Timing peaks in the AD . . . . .              | 166        |
| C.2 | Applying the cut . . . . .                    | 167        |
| C.3 | Correlation with the EC . . . . .             | 173        |
|     | <b>Bibliography</b>                           | <b>189</b> |



# List of Figures

|     |   |    |
|-----|---|----|
| 2.1 | Unitarity triangle in the $\rho - \eta$ plane. Two sides of the triangle can be expressed by the CKM matrix elements $ V_{td} /A\lambda^3$ and $ V_{ub}/V_{cb} /\lambda$ , respectively, where $A$ and $\lambda$ are parameters in the Wolfenstein parameterization. . . . .  | 9  |
| 2.2 | The global CKM fit results for the unitarity triangle, using the latest B and K measurements ( [9]). The results of constraints from the following measurements can be seen: the green annular area comes from the rates of tree-level semileptonic B decays, the orange and yellow ones from B meson oscillation parameters, the blue wedge around angle $\beta$ , as well as the light blue and brown constraints in the other angles, from CP asymmetries in the rates of hadronic B decays, and the light green hyperbola from indirect CP violation in $K^0 - \bar{K}^0$ mixing. . . . . | 11 |
| 2.3 | Unitarity triangle determined by $B$ and $K$ decays. . . . .  | 11 |
| 2.4 | Feynman diagram for the weak decay $K^+ \rightarrow \pi^0 e^+ \nu_e$ , which is allowed in the SM (left). Feynman diagram for the $K^+ \rightarrow \pi^+ \nu \bar{\nu}$ decay in a tree level, which is not allowed (right). . . . .  | 13 |

|     |  |    |
|-----|--|----|
| 2.5 | Second-order weak processes that contribute to the $K^+ \rightarrow \pi^+ \nu \bar{\nu}$ branching ratio: the "box" diagram (upper) and two "Z-penguin" diagrams (bottom). . . . .   | 13 |
| 2.6 | Schematic determination of the unitarity triangle apex $(\rho, \eta)$ from the B system (blue) and from the $K \rightarrow \pi \nu \bar{\nu}$ decays (red). Both determinations can be performed with small theoretical uncertainties, therefore any discrepancy between them, as illustrated in this hypothetical example [16], would indicate new physics. . . . .   | 18 |
| 3.1 | History of the search for $K^+ \rightarrow \pi^+ \nu \bar{\nu}$ . The vertical axis is the $\pi \nu \bar{\nu}$ Branching Ratio and the horizontal one the publication year. The triangles represent upper limits for the BR at the 90% confidence level, the boxes represent the central value of the measured BR and the dot represents an expected value with the full E949 running period, assuming that the central value of the branching ratio remains what the combined E787 and E949 results have found up to now, $BR = (1.47_{-0.89}^{+1.30}) \times 10^{-10}$ [23]. The error bars show the 68% CL intervals. . . . . | 21 |
| 3.2 | Momentum spectra of the charged product of the top 7 $K^+$ decay modes. The SM $K^+ \rightarrow \pi^+ \nu \bar{\nu}$ spectrum is also shown (not in scale). . . . .  | 22 |
| 3.3 | Schematic view of the AGS complex, which consists of a 200 MeV LINAC, a booster and a synchrotron. The secondary beam lines are located in the experimental area. . . . .  | 27 |

|      |   |    |
|------|---|----|
| 3.4  | Low-energy separated beam line III at BNL. . . . .  | 28 |
| 3.5  | Side view of the E949 detector. . . . .   | 29 |
| 3.6  | Side view of the Čerenkov counter. . . . .  | 31 |
| 3.7  | Cross-sectional view of the two beam wire chambers (BWPCs):<br>BWPC1 (left) and BWPC2 (right). . . . .  | 33 |
| 3.8  | End view of the B4 Hodoscope. . . . .   | 35 |
| 3.9  | Schematic cross section of the B4 Hodoscope. . . . .  | 35 |
| 3.10 | End (left) and side (right) views of the target. The CCD pulse-<br>shape information is used to find kaon and pion clusters, as<br>shown in the left figure. The lower two plots ((a) and (b)), are<br>CCD pulses for a kaon, and the upper two plots ((c) and (d)),<br>are those for a pion. Two layers of 6 plastic scintillators, the<br>I-Counter (IC) and V-Counter (VC), surround the target. . . .   | 37 |
| 3.11 | Schematic view of the Ultra Thin Chamber. . . . .   | 39 |
| 3.12 | End view of the Range Stack. The two layers of the Range<br>Stack Straw Chambers are located after layers 10 and 14. . . .  | 41 |
| 3.13 | Pulses in and around the stopping counter recorded by the TDs<br>of the upstream and downstream ends. The $\pi^+ \rightarrow \mu^+ \rightarrow e^+$<br>decay sequence is recorded in the stopping counter (Layer 12<br>in this case). The $\mu^+$ from the $\pi^+ \rightarrow \mu^+$ decay is contained<br>in the stopping counter. The positron from the $\mu^+ \rightarrow e^+$ de-<br>cay should also be found in the counters around the stopping<br>counter (Layers 13 and 14 in this case). . . . . | 44 |

|      |  |    |
|------|--|----|
| 3.14 | Schematic side (left) and end (right) views of the upper half of the E949 detector. Newly installed or upgraded photon detectors for E949 are in blue. . . . .   | 46 |
| 3.15 | End view (left) and back view (right) of the upstream End Cap. . . . .   | 48 |
| 3.16 | Number of kaon decays in the target as a function of the data-taking days for E787 and E949. . . . .   | 56 |
| 4.1  | Reconstruction of an event in the x-y view: the reconstruction in the target, UTC and Range Stack (top), and the reconstruction in the target (bottom). . . . .  | 60 |
| 4.2  | Double-pulse fit to the TD pulse shape in the stopping counter for the upstream (top) and downstream (bottom) end. . . . .   | 63 |
| 4.3  | Triple-pulse fit to the TD pulse shape in the stopping counter for the upstream (top) and downstream (bottom) end. . . . .   | 63 |
| 4.4  | Double-pulse fit to the CCD pulse shape in the Kaon decay vertex fiber for the high (top) and low (bottom) gain readout. The energy of the second pulse is a typical one for the energy deposit of a decay pion heading directly towards the detector acceptance. . . . .  | 64 |
| 4.5  | Double-pulse fit to the CCD pulse shape in the Kaon decay vertex fiber for the high (top) and low (bottom) gain readout. The energy of the second pulse is significantly higher than the typical energy deposit of a decay pion heading directly towards the detector acceptance, and may signify a scatter (see section 4.2). . . . . | 65 |

|      |  |    |
|------|--|----|
| 4.6  | The range in plastic scintillator ( $rtot$ ) versus momentum ( $ptot$ ) distribution of the outgoing charged particle (pion or muon) for the events which passed the $\pi\nu\overline{\nu}(1)$ or (2) trigger. . . . . | 68 |
| 4.7  | Schematic diagrams of the Single Beam background: a Single Kaon Beam background (top) and a Single Pion Beam background (bottom). . . . .  | 70 |
| 4.8  | Schematic diagrams of the Double Beam background: a $K - K$ Double Beam background (top) and a $K - \pi$ Double Beam background (bottom). . . . .  | 70 |
| 4.9  | Schematic diagram of the charge exchange interaction background. . . . .   | 70 |
| 4.10 | A schematic of a $K_{\pi 2}$ scattering event in the target in which the pion travels along the fibers, and thereby the neutral pion escapes through the weak photon detection region of the detector.                 | 72 |

|      |  |    |
|------|--|----|
| 4.11 | A background estimate resulting from a bifurcated analysis.<br>The letters signify both the samples and the number of events in them.<br>Top: If a certain background is suppressed by cut1 and cut2, then the data sample can be represented in the parameter space of these two cuts as 4 sub-samples A, B, C and D. If these cuts are uncorrelated, then the number of background events in region A relative to that in B is equal to that in C relative to D.<br>Middle: Count events that fail cut1 and pass cut2 to get the normalization B.<br>Bottom: Select events that fail cut2, and measure the rejection of cut1 via $R = (C + D)/C$ . Region A is never examined in this procedure. The background estimated to be present in region A is given by $BC/D = B/(R - 1)$ . . . . . | 78 |
| 4.12 | Schematic representation of the outside-the-box study. . . . .   | 79 |
| 5.1  | Energy distribution of the second pulse in the Kaon fiber for class 12 of the $K_{\pi 2}$ TG scatter rejection branch (top), for $K_{\pi 2}$ peak events (middle) and for $K_{\mu 2}$ events (bottom). . . . .   | 82 |

|     |  |     |
|-----|--|-----|
| 5.2 | Top: $p_{tot}$ distribution of the events remaining in the normalization branch of the $K_{\pi 2}$ TG scatter study after the inversion of PVCUTPNN2 (black), after the application of all the TGCUT06 except CCDPUL (red), and after the application of CCDPUL (blue). Bottom: $p_{tot}$ distribution of the events in class 12 of the rejection branch of the $K_{\pi 2}$ TG scatter study before (black) and after (red) PVCUTPNN2. . . . . | 85  |
| 5.3 | Tpi-tk distribution of events in the single beam background rejection branch before (black) and after (red) the inversion of B4DEDX. . . . .   | 89  |
| 5.4 | Single beam bifurcations: (a) rejection branch, with the values of the DELCO3 rejection obtained for the 3 sub-branches, and (b) normalization branch. Numbers under the boxes are the number of events remaining after the cuts were applied. TD is the TDCUT02 cut, and KIN the KCUT cut. . . . .  | 90  |
| 5.5 | Double beam Bifurcations: (a) rejection branch, and (b) normalization branch, for both K-K and K- $\pi$ . Numbers under the boxes are the number of events remaining after the cuts were applied. The K- $\pi$ numbers are for the early runs (before the change in trigger) and the K-K numbers are from all runs. . .  | 92  |
| 5.6 | Total kinetic energy ( $T_2$ ) of the $\pi^-$ and the $e^+$ versus the momentum of the $\pi^+$ ( $P_{tot}$ ) for $K^+ \rightarrow \pi^+\pi^-e^+\nu$ Monte Carlo events that pass the $\pi\nu\bar{\nu}(2)$ trigger. . . . .   | 97  |
| 5.7 | Observable absorption energy of $\pi^-$ stopped in the target. . .   | 100 |

|      |   |     |
|------|---|-----|
| 5.8  | $E_{hide}$ versus $T_{xtg}$ (top) and projections on $T_{xtg}$ (bottom left) and $E_{hide}$ (bottom right) for the $K^+ \rightarrow \pi^+ \pi^- e^+ \nu$ Monte Carlo events that survive all analysis cuts applicable in UMC. . . . | 102 |
| 5.9  | Pion energy spectrum from $K_{\pi 2 \gamma}$ generated by MC, using only the inner Bremsstrahlung process. . . . .  | 104 |
| 5.10 | Energy vs polar angle of the non- $\pi^0$ photon from the $K_{\pi 2 \gamma}$ MC events that passed all the cuts. . . . .  | 106 |
| 5.11 | The method used to calculate the expected CEX background. The shaded boxes are not accessible in data, since they are the signal region, but they are in MC. . . . .  | 108 |
| 6.1  | The reconstructed pion mass distributions from $\pi_{scat}$ (top) and $K_{\pi 2}$ events (bottom). . . . .  | 120 |
| 8.1  | Schematic of the PV optimization process. . . . .   | 155 |
| 8.2  | Offline rejection vs acceptance profile for the $K_{\pi 2}$ peak, with each subsystem contribution. . . . .   | 157 |
| 8.3  | Offline rejection vs acceptance profile for the CLASS 2, with each subsystem contribution. . . . .  | 158 |
| 8.4  | Offline rejection vs acceptance profile for the CLASS 5, with each subsystem contribution. . . . .  | 159 |
| 8.5  | Offline rejection vs acceptance profile for the CLASS 7, with each subsystem contribution. . . . .  | 160 |
| 8.6  | Offline rejection vs acceptance profile for the CLASS 9, with each subsystem contribution. . . . .  | 161 |



|      |  |     |
|------|--|-----|
| 8.7  | Offline rejection vs acceptance profile for CLASS 12, with each subsystem contribution. . . . .  | 162 |
| 8.8  | Radiation length of the material of the E949 detector as a function of polar angle. The higher curve is after the addition of the BVL, which adds crucial radiation lengths in the weak region around 45 degrees. . . . .  | 163 |
| 8.9  | Time distributions (in ns) of the AD TDC hits with respect to tk (top row) and tpi (bottom row) for sectors on the incoming Kaon path. Black histograms are for the acceptance sample and red for the two rejection samples ( $K_{\pi 2}$ peak on the left and kinks on the right). The units on the vertical axis are arbitrary.  | 168 |
| 8.10 | Time distributions (in ns) of the AD TDC hits with respect to tk (top row) and tpi (bottom row) for sectors off the incoming Kaon path. Black histograms are for the acceptance sample and red for the two rejection samples ( $K_{\pi 2}$ peak on the left and kinks on the right). The units on the vertical axis are arbitrary. | 169 |
| 8.11 | Time distributions (in ns) of the AD CCD hits with respect to tk (top row) and tpi (bottom row) for sectors on the incoming Kaon path. Black histograms are for the acceptance sample and red for the two rejection samples ( $K_{\pi 2}$ peak on the left and kinks on the right). The units on the vertical axis are arbitrary.  | 170 |

|      |  |     |
|------|--|-----|
| 8.12 | Time distributions (in ns) of the AD CCD hits with respect to tk (top row) and tpi (bottom row) for sectors off the incoming Kaon path. Black histograms are for the acceptance sample and red for the two rejection samples ( $K_{\pi 2}$ peak on the left and kinks on the right). The units on the vertical axis are arbitrary. | 171 |
| 8.13 | Time distributions (in ns) with respect to tpi for sectors off the incoming Kaon path, from TDCs (top) and CCDs (bottom). Black histograms are for $K_{\pi 2}$ peak and red for kinks. The units on the vertical axis are arbitrary.   | 172 |
| 8.14 | Time distributions (in ns) with respect to tk (left) and tpi (right) of the TDC hit closest to tk or tpi, vs total ADC energy for $K_{\mu 2}$ (top), $K_{\pi 2}$ peak (middle) and kinks (bottom).   | 175 |
| 8.15 | Time distributions (in ns) with respect to tk (left) and tpi (right) of the CCD hit closest to tk or tpi, vs total CCD energy for $K_{\mu 2}$ (top), $K_{\pi 2}$ peak (middle) and kinks (bottom).   | 176 |
| 8.16 | Total ADC energy in time with tk ( $\pm 5ns$ , left), and in time with the photon ( $0-8ns$ from tpi, right) for $K_{\mu 2}$ (top), $K_{\pi 2}$ peak (middle) and kinks (bottom).  | 177 |
| 8.17 | Total CCD energy in time with tk ( $\pm 5ns$ , left), and in time with the photon ( $0-8ns$ from tpi, right) for $K_{\mu 2}$ (top), $K_{\pi 2}$ peak (middle) and kinks (bottom).  | 178 |

|      |   |     |
|------|---|-----|
| 8.18 | Acceptance*rejection vs total ADC or CCD energy threshold,<br>for different sector selection, for $K_{\pi 2}$ peak events. The different<br>sets of points correspond to ADC cases a-d and CCD cases a-b<br>explained in the text, from bottom to top. The points for ADC<br>cases a and b (black and red), as well as c and d (green and<br>blue), completely overlap. . . . .   | 179 |
| 8.19 | Acceptance*rejection vs total ADC or CCD energy threshold,<br>for different sector selection, for kink events. The different sets<br>of points correspond to ADC cases a-d and CCD cases a-b ex-<br>plained in the text, from bottom to top. The points for ADC<br>cases a and b (black and red), as well as c and d (green and<br>blue), completely overlap. . . . .   | 180 |
| 8.20 | Acceptance*rejection vs total ADC or CCD energy threshold,<br>for different sector selection, for $K_{\pi 2}$ peak events with tight setup<br>PV. The different sets of points correspond to ADC cases a-d<br>and CCD cases a-b explained in the text, from bottom to top.<br>The points for ADC cases a and b (black and red), as well as c<br>and d (green and blue), completely overlap. . . . .   | 181 |
| 8.21 | Acceptance*rejection vs total ADC or CCD energy threshold,<br>for different sector selection, for $K_{\pi 2}$ peak events with tight setup<br>EC1 PV, with the rest of the systems at a loose setting. The<br>different sets of points correspond to ADC cases a-d and CCD<br>cases a-b explained in the text, from bottom to top. The points<br>for ADC cases a and b (black and red), as well as c and d (green<br>and blue), completely overlap. . . . . | 182 |

|      |   |     |
|------|---|-----|
| 8.22 | Percentage of events with zero energy deposit in the EC1 as a function of energy deposit in the AD (left) and the scatter plots of EC1 energy vs AD CCD energy that these graphs were created from (right), for $K_{\mu 2}$ (top), $K_{\pi 2}$ peak (middle) and kinks (bottom).                                  | 183 |
| 8.23 | Percentage of events with zero energy deposit in the upstream EC (without the inner ring) as a function of energy deposit in the AD (left) and the scatter plots of EC1 energy vs AD CCD energy that these graphs were created from (right), for $K_{\mu 2}$ (top), $K_{\pi 2}$ peak (middle) and kinks (bottom). | 184 |

# Acknowledgements

First of all I would like to thank all my collaborators from the E949 and E787 experiment for making this measurement a reality, and developing the analysis tools to carry out such an interesting measurement. Special thanks go to David Jaffe, for his valuable guidance and remarkable knowledge that he provided me with. This analysis would have never reached this point without his persistence and scrutiny. Also thanks to Benji Lewis, Wang Zhe, Joss Ives and Dima Patalakha who shared the weight of the analysis with me; to Steve Kettell, Laurie Littenberg, George Redlinger and Jim Frank, for their helpful insights and patience to provide me with the information I needed and teach me how to understand it; to Joe Mildenerger, Kentaro Mizouchi, Toshio Numao and the rest of the collaborators; to Milind Diwan and Bipul Bhuyan, who did the E787 PNN2 analysis and were always willing to share their knowledge and experience with me. I would also like to thank my advisor, Mike Marx, for the continuing financial support throughout the years of my graduate studies.

The other people I owe much of my development to are my friends and family, here and in Greece. I would like to thank James, Elli, Ryan, Sofia and all the others that have been a breeze of fresh air during my difficult graduate years, and especially my dearest friend and colleague, Jorge. Without his

support, unconditional love and stimulating discussions, I would have never found the strength and motivation to keep going. Finally I would like to express my appreciation to my parents, who formed me into who I am and taught me to strive to achieve my dreams.

# Chapter 1

## Introduction

The decay  $K^+ \rightarrow \pi^+ \nu \bar{\nu}$  is a flavor-changing neutral current process, therefore it is forbidden at the tree level in the Standard Model (SM). It proceeds only through second order diagrams at a very low rate, because of the GIM mechanism (see chapter 2.1). Since u, c and t quarks are included in the loop, this decay is a useful probe of the flavor structure of the SM, which is epitomized in the  $3 \times 3$  CKM matrix (see chapter 2.1). It turns out that  $K^+ \rightarrow \pi^+ \nu \bar{\nu}$  can give an unambiguous measurement of the smallest element of the CKM matrix,  $|V_{td}|$ , and, combined with the neutral mode  $K^0 \rightarrow \pi^0 \nu \bar{\nu}$ , of the CP violating phase of the matrix. This is because the long range effects contribution to the rate are negligible, and the hadronic matrix element can be factored out using the well-measured decay  $K^+ \rightarrow \pi^0 e^+ \nu$ , therefore the Branching Ratio of the  $K^+ \rightarrow \pi^+ \nu \bar{\nu}$  decay has very small theoretical uncertainties. In the SM, it is calculated to be  $BR(K^+ \rightarrow \pi^+ \nu \bar{\nu}) = (8.0 \pm 1.1) \times 10^{-11}$ .

Any extra particles from beyond-the-SM physics would also contribute to the amplitude of  $K^+ \rightarrow \pi^+ \nu \bar{\nu}$ . Most beyond-the-SM theories include extra

sources of CP violation, and there are also models that allow direct flavor violation (see chapter 2.3). Such effects could cause a higher BR for this decay, and in some cases predict discrepancies in the CKM matrix elements values measured by Kaon and B meson processes. Therefore,  $K^+ \rightarrow \pi^+ \nu \bar{\nu}$  is also a valuable probe for new physics.

The detection of such a rare decay is extremely challenging. An intense and pure Kaon beam is needed, and a detector that will precisely identify and measure the kinematics of both the incoming particle and the decay products. Since the signature of  $K^+ \rightarrow \pi^+ \nu \bar{\nu}$  is one charged track and nothing else, the detector should also be able to veto on any extra activity due to the rest of the  $K^+$  decay modes. The E949 detector in Brookhaven National Laboratory's (BNL) Alternating Gradient Synchrotron is such an apparatus. It is the upgrade of the E787 detector, which detected the first 2  $K^+ \rightarrow \pi^+ \nu \bar{\nu}$  decay candidates of the total of 3 that have been observed up to now.

From the approximately  $10^{12}$  Kaon decays recorded by the E949 detector during its running time, only a handful of  $K^+ \rightarrow \pi^+ \nu \bar{\nu}$  decays are expected to be accepted by the trigger. In order to isolate these events and predict the number of background expected to be observed together with them, Monte Carlo simulation is not adequate. At such level of precision, uncertainties in the simulation of nuclear processes and detector defects make the prediction unreliable. Therefore, most of the background estimations will be performed with real data, following a “blind” analysis, during which the signal region will not be examined until the very end. For some classes of background, however, that have similar signatures, Monte Carlo will have to be used to some extent, in order to estimate how efficiently such backgrounds are suppressed by the



analysis selection criteria (“cuts”). But the data are ultimately used for scaling the background measurement.

In E949’s analysis, in order to further avoid bias, the cuts are first optimized in a subset of  $1/3$  of the data, based on minimizing the background while still keeping as much signal acceptance as possible. The expected background in the signal region and the Single Event Sensitivity are measured, then the cuts are “frozen” and the measurements are repeated on the remaining  $2/3$  of the data, and the results are checked for consistency. The signal region is examined at the very end, when all the background estimations are final, and the cuts are not allowed to vary any more.

This thesis describes the analysis of the  $1/3$  sample. The background estimations, cut correlation studies and acceptance measurements based on this sample are shown.

# Chapter 2

## Theory

The Standard Model of particle physics [1] has accounted for almost all particles and their interactions that have been observed. Matter is built of 3 generations of leptons and their respective neutrinos, and 3 generations of quarks. The interactions between them are explained by two gauge theories: Quantum Chromodynamics (QCD), with 8 gauge bosons called gluons, which accounts for the strong interaction between quarks, and the Glashow-Weinberg-Salam (GWS) theory, which accounts for the electromagnetic (carried by the photon between electrically charged particles) and the weak interactions (which are carried by the  $W^\pm$  and  $Z^0$  bosons and affect all particles) and their unification. In the context of the SM, the masses of all particles, except for the photon and gluon which are massless, arise from spontaneous symmetry breaking that occurs due to the existence of a scalar particle called the Higgs boson.

It has been evident from as early as 1956 that the weak interaction differs from the other ones in the non-conservation of parity  $P$ , as it is a vector-axial ( $V - A$ ) interaction. However, the combined charge conjugation - parity ( $CP$ )

symmetry was thought to be conserved until the astonishing result of the BNL E-0181 experiment in 1964 [2], that discovered CP violation in the neutral Kaon system. Since then, an elegant explanation has been incorporated in the SM, where CP violation arises naturally from the existence of 3 families of quarks that “mix”<sup>1</sup> with each other through the weak interactions: the Kobayashi-Maskawa (KM) theory [3] introduces a  $3 \times 3$  unitary matrix for this “mixing”, called the Cabibbo-Kobayashi-Maskawa (CKM) matrix. Particle flavors are still conserved in the strong and electromagnetic interactions.

As  $K^+ \rightarrow \pi^+ \nu \bar{\nu}$  is a Flavor Changing Neutral Current (FCNC) weak process, the flavor structure of the SM and its predictions for the Branching Ratio  $BR$  of this decay will be presented in this chapter. The particular aspects and parameters of the SM that can be measured with this decay will be pinpointed and the potential physics beyond the SM that could be accessed will be reviewed.

## 2.1 CP violation in the Standard Model

There are charged and neutral current processes in the weak interaction, mediated by the  $W^+$  or  $W^-$  and the  $Z^0$  bosons respectively. In the charged-current processes, one quark can transform into another quark of the same family with a different electric charge/flavor (e.g.,  $u \rightarrow d$ ), and one lepton can transform into the respective neutrino (e.g.,  $e^- \rightarrow \nu_e$ ) and vice versa. However, as the fact that heavier quarks decay into lighter ones shows, the charged-current weak

---

<sup>1</sup>Quarks from different families do not mix with each other literally, but they can transform to one another through the charged Weak interaction, whose strength is modulated by the CKM matrix elements. The term “mix” will be used here in that sense.

interaction allows transformation of quarks between different generations (e.g.,  $c \rightarrow d$ ), with the strength of the interaction depending on the parameters of the CKM matrix  $V$ :

$$\begin{pmatrix} d' \\ s' \\ b' \end{pmatrix} = V \begin{pmatrix} d \\ s \\ b \end{pmatrix} = \begin{pmatrix} V_{ud} & V_{us} & V_{ub} \\ V_{cd} & V_{cs} & V_{cb} \\ V_{td} & V_{ts} & V_{tb} \end{pmatrix} \begin{pmatrix} d \\ s \\ b \end{pmatrix} \quad (2.1)$$

which connects the weak eigenstates  $d'$ ,  $s'$ ,  $b'$  to their mass eigenstates  $d$ ,  $s$ ,  $b$ . Thus the quark that couples to the weak interaction charged bosons is a linear combination of the free (mass) eigenstates, and it can transform to another flavor through the interaction. In this picture, since  $V$  is unitary and  $3 \times 3$ , there is one irreducible imaginary phase in it. CP invariance of the Lagrangian for weak interactions is violated when the CKM matrix is a complex one, therefore CP violation is naturally explained. A similar structure is speculated to exist also in the leptonic sector, since the neutrinos have been found to possess mass, described by the  $3 \times 3$  Maki-Nakagawa-Sakata (MNS) matrix [4].

In the neutral-current weak processes, however, when a single  $Z^0$  is exchanged, a quark cannot transform into another quark with the same charge and a different flavor (e.g.,  $s \rightarrow d$ ). These FCNC processes are forbidden in the first order (see Fig. 2.4), and suppressed at the one-loop level due to the Glashow-Iliopoulos-Maiani (GIM) mechanism [5]: the weak eigenstates,  $d'$  and  $s'$ , not the mass eigenstates,  $d$  and  $s$ , participate in the weak interaction. Their relation is written as

$$\begin{pmatrix} d' \\ s' \end{pmatrix} = \begin{pmatrix} \cos \theta_C & \sin \theta_C \\ -\sin \theta_C & \cos \theta_C \end{pmatrix} \begin{pmatrix} d \\ s \end{pmatrix}, \quad (2.2)$$

where  $\theta_C$  is called the Cabibbo angle [6]. The neutral current  $J^0$ , is expressed by the following description (omitting the  $\gamma$ -matrices):

$$\begin{aligned} J^0 &= \bar{u}u + \bar{c}c + \bar{d}'d' + \bar{s}'s' \\ &= \bar{u}u + \bar{c}c + (\bar{d}d + \bar{s}s) \cos^2 \theta_C + (\bar{d}d + \bar{s}s) \sin^2 \theta_C \quad : \text{ (flavor conserving term)} \\ &\quad + (\bar{d}s + \bar{s}d - \bar{d}s - \bar{s}d) \sin \theta_C \cos \theta_C \quad : \text{ (flavor changing term)} \\ &= \bar{u}u + \bar{c}c + \bar{d}d + \bar{s}s. \end{aligned} \quad (2.3)$$

The term that accounts for the FCNC processes vanishes, and therefore the absence of first order FCNC processes is explained by this description. The GIM cancellation can also work at 1-loop diagrams (see Fig. 2.5), where the initial-to-final quark transitions are effectively the FCNC processes, if the quarks in the intermediate state (e.g., the  $u$  and  $c$  quarks in the  $K^0 - \bar{K}^0$  mixing) have the same mass. Since the quark masses depend on the quark flavors, this cancellation is not perfect, and thus the FCNC processes are allowed as "rare decays" at higher orders.

The unitary CKM matrix has four independent parameters, which in leading order of the Wolfenstein parameterization [7] are  $A$ ,  $\lambda$ ,  $\rho$  and  $\eta$ . In terms of these parameters, the CKM matrix can be written as

$$\begin{pmatrix} V_{ud} & V_{us} & V_{ub} \\ V_{cd} & V_{cs} & V_{cb} \\ V_{td} & V_{ts} & V_{tb} \end{pmatrix} \simeq \begin{pmatrix} 1 - \lambda^2/2 & \lambda & A\lambda^3(\rho - i\eta) \\ -\lambda & 1 - \lambda^2/2 & A\lambda^2 \\ A\lambda^3(1 - \rho - i\eta) & -A\lambda^2 & 1 \end{pmatrix} \quad (2.4)$$

where  $\lambda = \sin \theta_c = 0.22$  is the sine of the Cabibbo angle, the “mixing” angle for the case of 2 quark generations initially studied by Cabibbo. One sole parameter  $\eta$  describes CP violation in the SM, since a non-zero value of this parameter breaks the CP invariance for weak interactions.

The values of the CKM matrix elements are not defined by any first principles, and can only be experimentally measured and constrained. The present values of the magnitudes are:

$$\begin{pmatrix} |V_{ud}| & |V_{us}| & |V_{ub}| \\ |V_{cd}| & |V_{cs}| & |V_{cb}| \\ |V_{td}| & |V_{ts}| & |V_{tb}| \end{pmatrix} \simeq \begin{pmatrix} [0.9736, 0.9741] & [0.2262, 0.2282] & [0.0039, 0.0041] \\ [0.2261, 0.2281] & [0.9727, 0.9732] & [0.0414, 0.0423] \\ [0.0075, 0.0085] & [0.0409, 0.0417] & [0.9991, 0.9991] \end{pmatrix} \quad (2.5)$$

at the 90% confidence level interval [8]. These values can either be determined directly from tree-level decays (e.g., the simplest, neutron beta decay, or  $B \rightarrow \pi l \nu$ ), or (particularly those involving couplings to the top quark) indirectly from flavor-changing second-order weak processes that involve the up-type quarks in an internal loop (e.g.,  $K^+ \rightarrow \pi^+ \nu \bar{\nu}$ ). It is assumed that the dominant contribution to the processes comes from the  $t$  quark loop. The agreement or disagreement between the measured and predicted (based on

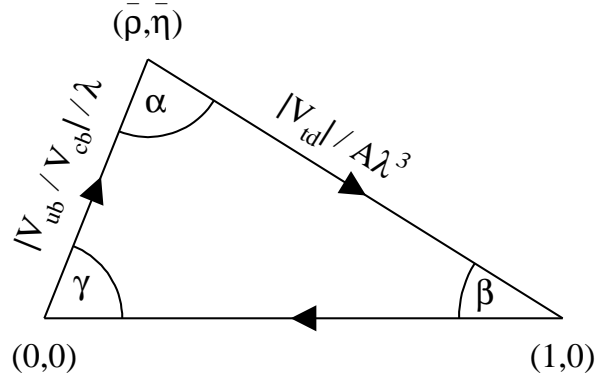


Figure 2.1: Unitarity triangle in the  $\rho - \eta$  plane. Two sides of the triangle can be expressed by the CKM matrix elements  $|V_{td}|/A\lambda^3$  and  $|V_{ub}/V_{cb}|/\lambda$ , respectively, where  $A$  and  $\lambda$  are parameters in the Wolfenstein parameterization.

independent measurements) quantities can put constraints on new physics.

All of the information concerning the CKM matrix elements can be summarized in terms of "unitarity triangles". The unitarity of this matrix can be expressed with 9 conditions, 6 of which (the ones for the off-diagonal elements) can be represented graphically in the form of triangles, all of which must have the same area. Applying the unitarity property  $V^\dagger V = 1$  to the CKM matrix in (2.4), the relation including the matrix element of interest  $V_{td}$  is

$$V_{ub}^* V_{ud} + V_{cb}^* V_{cd} + V_{tb}^* V_{td} \simeq V_{ub}^* - \lambda V_{cb}^* + V_{td} = 0, \quad (2.6)$$

where the approximations  $V_{ud} \simeq V_{tb}^* \simeq 1$  and  $V_{cd} \simeq -\lambda$  have been made. This equation can be represented graphically, as shown in Fig. 2.1, where both sides of the equation have been divided by  $\lambda V_{cb}^*$ . The apex of the triangle in the  $\rho - \eta$  plane is given by two improved Wolfenstein parameters,  $\bar{\rho}$  and  $\bar{\eta}$ , where  $\bar{\rho} = \rho(1 - \lambda^2/2)$  and  $\bar{\eta} = \eta(1 - \lambda^2/2)$ .

The values of these parameters currently come from several measurements of  $B$  meson decays, as well as a measurement of the indirect CP violation

parameter from  $K^0 - \bar{K}^0$  mixing,  $\epsilon_K$ , as shown in Fig. 2.2. All these measurements agree to a very good level and the  $\rho - \eta$  parameters are well constrained. However, it is desirable to over-constrain the position of the apex in as many independent ways as possible, because any disagreement among the independent measurements would indicate the presence of new physics that contains new sources of CP violation. Such sources are expected to exist, because the parameters for CP violation in the SM are not sufficient to explain the observed matter-antimatter asymmetry of the Universe. An especially powerful probe for such new physics is the comparison of the results from  $B$  meson and kaon decays with small theoretical ambiguities. In other words, since the CKM phase should be the only source of CP violation within the SM, precise measurements of all the CKM matrix elements are crucial.

The determination of  $\rho$  and  $\eta$  independently from  $B$  and  $K$  decays, as shown in Fig. 2.3, can be examined in two ways:

- A comparison of the angle  $\beta$  from the ratio  $BR(K_L^0 \rightarrow \pi^0 \nu \bar{\nu})/BR(K^+ \rightarrow \pi^+ \nu \bar{\nu})$  and from CP violation asymmetry ( $\mathcal{A}_{CP}$ ) in the decay  $B_d^0 \rightarrow J/\psi K_s^0$ .
- A comparison of the magnitude  $|V_{td}|$  from  $K^+ \rightarrow \pi^+ \nu \bar{\nu}$  and from the mixing frequencies of  $B_s$  and  $B_d$  mesons, expressed in terms of the ratio of the mass differences,  $\Delta M_{B_s}/\Delta M_{B_d}$ .

The motivation to search for  $K^+ \rightarrow \pi^+ \nu \bar{\nu}$  also stems from a desire to measure the small, imprecisely-determined CKM matrix element  $|V_{td}|$ , as well as to search for non-SM physics.



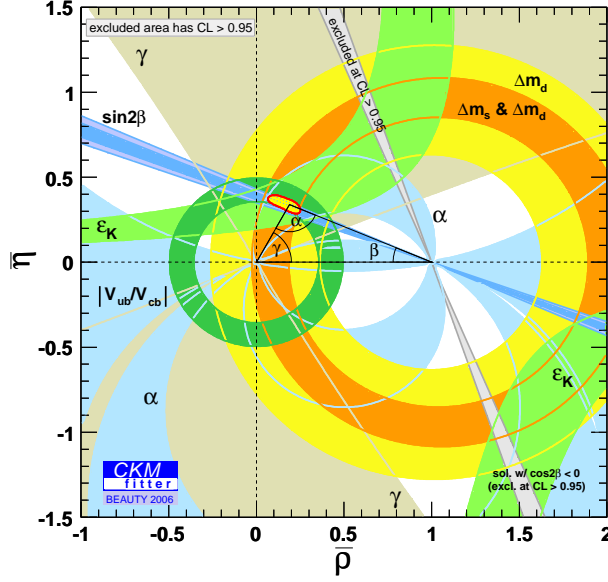


Figure 2.2: The global CKM fit results for the unitarity triangle, using the latest B and K measurements ([9]). The results of constraints from the following measurements can be seen: the green annular area comes from the rates of tree-level semileptonic B decays, the orange and yellow ones from B meson oscillation parameters, the blue wedge around angle  $\beta$ , as well as the light blue and brown constraints in the other angles, from CP asymmetries in the rates of hadronic B decays, and the light green hyperbola from indirect CP violation in  $K^0 - \bar{K}^0$  mixing.

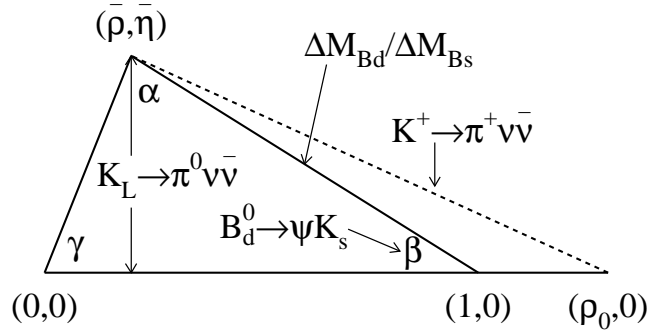


Figure 2.3: Unitarity triangle determined by  $B$  and  $K$  decays.

## 2.2 $K^+ \rightarrow \pi^+ \nu \bar{\nu}$ in the Standard Model

The decay  $K^+ \rightarrow \pi^+ \nu \bar{\nu}$  is a FCNC process that is prohibited in the first order (see Fig. 2.4). However, this decay is allowed in the second order, and is described by a box diagram and two Z-penguin diagrams, as shown in Fig. 2.5.

Taking into account only the  $\bar{s} \rightarrow (\bar{u}, \bar{c}, \bar{t}) \rightarrow \bar{d}$  part of the box diagram, the part of the weak amplitude for this process directly involving quarks is represented as

$$\mathcal{M} \sim \bar{s} \left( \sum_{i=u,c,t} V_{is}^* V_{id} (\gamma^\mu P_L \frac{\not{p} + m_i}{p^2 - m_i^2} \gamma^\nu P_L) \right) d \quad (2.7)$$

where the  $V_{ij}$ 's are the CKM matrix elements, the  $\gamma$ s are the Dirac matrices,  $P_{L/R} = \frac{1 \mp \gamma^5}{2}$  is the left/right-handed projection operator,  $p$  is the momentum transfer, and the  $m_i$ 's are the quark masses. Using Dirac algebra, the term in the parenthesis can be written as

$$\gamma^\mu P_L \frac{\not{p} + m_i}{p^2 - m_i^2} \gamma^\nu P_L = \frac{1}{p^2 - m_i^2} (\gamma^\mu P_L \not{p} P_R \gamma^\nu + m_i \gamma^\mu P_L P_R \gamma^\nu) \quad (2.8)$$

where the relation  $\gamma^\nu P_L = P_R \gamma^\nu$  has been used. The second term vanishes because  $P_L P_R = 0$ , therefore equation 2.7 can be written as

$$\mathcal{M} \sim \bar{s} \left( \sum_{i=u,c,t} \frac{V_{is}^* V_{id}}{p^2 - m_i^2} \gamma^\mu P_L \not{p} \gamma^\nu \right) d \quad (2.9)$$

$\mathcal{M}$  vanishes if all of the quark masses  $m_i$ , are equal, because of the unitarity of the CKM matrix. However, the breaking of flavor symmetry, which results

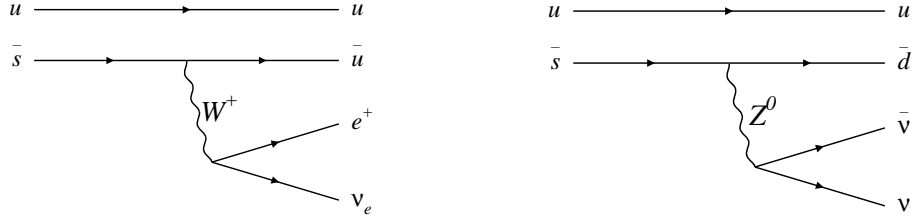


Figure 2.4: Feynman diagram for the weak decay  $K^+ \rightarrow \pi^0 e^+ \nu_e$ , which is allowed in the SM (left). Feynman diagram for the  $K^+ \rightarrow \pi^+ \nu \bar{\nu}$  decay in a tree level, which is not allowed (right).

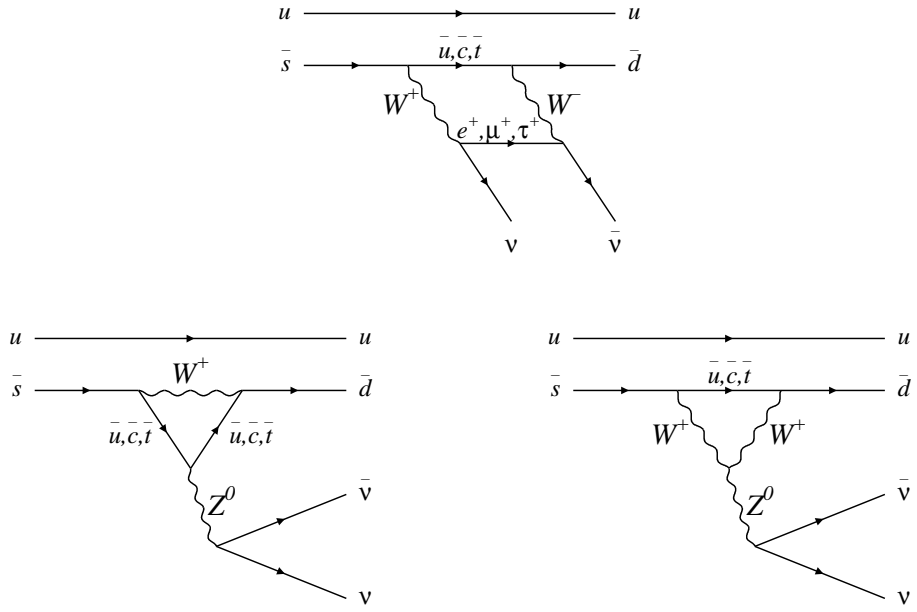


Figure 2.5: Second-order weak processes that contribute to the  $K^+ \rightarrow \pi^+ \nu \bar{\nu}$  branching ratio: the "box" diagram (upper) and two "Z-penguin" diagrams (bottom).

in the different quark masses, allows this decay to proceed at a very small rate. Since the top quark mass is the most different (largest) of the three, its contribution to the  $K^+ \rightarrow \pi^+ \nu \bar{\nu}$  branching ratio is the largest. This decay is sensitive to the weak coupling of top to down quarks, given by the CKM matrix element  $V_{td}$ .

The branching ratio for  $K^+ \rightarrow \pi^+ \nu \bar{\nu}$  is calculated by following the convention in [10] and [11]. The effective Hamiltonian in the SM can be written as

$$\mathcal{H}_{eff}^{SM} = \frac{G_F}{\sqrt{2}} \frac{\alpha}{2\pi \sin^2 \Theta_W} \sum_{l=e,\mu,\tau} (V_{cs}^* V_{cd} X^l(x_c) + V_{ts}^* V_{td} X(x_t)) (\bar{s}d)_{V-A} (\bar{\nu}_l \nu_l)_{V-A}, \quad (2.10)$$

where  $X(x_j)$  are functions of  $x_j \equiv m_j^2/M_W^2$  summarizing the top and charm quark contributions in the loop, including QCD corrections at the next-to-next-to-leading-order (NNLO) level. The up quark term has been removed using the unitarity of the CKM matrix. The dependence on the charged lepton mass in the loop is negligible for the top quark contribution, but not for the charm quark for the case of tau lepton. Therefore the perturbative charm contribution is described in terms of the parameter

$$P_c(X) \equiv \frac{1}{\lambda^4} \left( \frac{2}{3} X^e + \frac{1}{3} X^\tau \right) = 0.375 \pm 0.009_{theory} \pm 0.031_{m_c} \pm 0.009_{a_s} \quad (2.11)$$

where  $\lambda = \sin \theta_c = 0.2248$  has been used. The errors on the right-hand side of (2.11) correspond to the uncertainty in the charm mass,  $m_c$  and the

coupling constant,  $\alpha_s(M_Z^2)$ . As can be seen from this equation, the theoretical uncertainty in the charm contribution, that used to be the dominant uncertainty in estimating  $\text{BR}(K^+ \rightarrow \pi^+ \nu \bar{\nu})$ , has been drastically reduced by recent next-to-next-to-leading-order (NNLO) calculations described in [11], and it has been brought to the same order as the other contributions.

The theoretical uncertainty in the dominant top contribution is very small, and is essentially determined by the experimental error on the top quark mass,  $m_t$ . With the top quark mass  $m_t = (163.0 \pm 2.8) \text{ GeV}$  ([11]),

$$X(x_t) = 1.464 \pm 0.041 \quad (2.12)$$

is obtained, and its contribution to the uncertainty in the BR is about 4%.

The hadronic part of the  $K^+ \rightarrow \pi^+ \nu \bar{\nu}$  amplitude can be factored out using the tree level  $K^+ \rightarrow \pi^0 e^+ \nu$  decay, whose BR is well known and which is the isospin-rotated  $K^+ \rightarrow \pi^+ \nu \bar{\nu}$  one:

$$\langle \pi^+ | \mathcal{M} | K^+ \rangle = \sqrt{2} \langle \pi^0 | \mathcal{M} | K^+ \rangle \quad (2.13)$$

With these definitions the branching ratio for  $K^+ \rightarrow \pi^+ \nu \bar{\nu}$  can be written as

$$\text{BR}(K^+ \rightarrow \pi^+ \nu \bar{\nu}) = \kappa_+ \left[ \left( \frac{\text{Im} \lambda_t}{\lambda^5} X(x_t) \right)^2 + \left( \frac{\text{Re} \lambda_c}{\lambda} P_c(X) + \frac{\text{Re} \lambda_t}{\lambda^5} X(x_t) \right)^2 \right] \quad (2.14)$$

where

$$\kappa_+ \equiv r_+ \frac{3\alpha^2 BR(K^+ \rightarrow \pi^0 e^+ \nu)}{2\pi^2 \sin^4 \theta_W} \lambda^8 = (5.04 \pm 0.17) \times 10^{-11} \left[ \frac{\lambda}{0.2248} \right]^8 \quad (2.15)$$

and the  $\lambda_j$ 's ( $\equiv V_{js}^* V_{jd}$ ) are from the CKM matrix elements. The  $r_+$  ( $= 0.901$ ) represents isospin breaking corrections in relating  $K^+ \rightarrow \pi^+ \nu \bar{\nu}$  to the well-measured leading decay  $K^+ \rightarrow \pi^0 e^+ \nu$  [12]. In obtaining the numerical value in (2.15), we used [13]

$$\sin^2 \theta_W = 0.231, \quad \alpha = \frac{1}{127.9}, \quad BR(K^+ \rightarrow \pi^0 e^+ \nu) = (4.93 \pm 0.07) \times 10^{-2}. \quad (2.16)$$

Expression (2.14) describes in the  $\bar{\rho} - \bar{\eta}$  plane an ellipse with a small eccentricity, namely

$$(\sigma \bar{\eta})^2 + (\bar{\rho} - \bar{\rho}_0)^2 = \frac{\sigma \mathcal{B}(K^+ \rightarrow \pi^+ \nu \bar{\nu})}{\bar{\kappa}_+ |V_{cb}|^4 X^2(x_t)}, \quad (2.17)$$

where

$$\bar{\rho}_0 \equiv 1 + \frac{\lambda^4 P_c(X)}{|V_{cb}|^2 X(x_t)}, \sigma \equiv \left(1 - \frac{\lambda^2}{2}\right)^{-2}, \bar{\kappa}_+ \equiv \frac{\kappa_+}{\lambda^8} = (7.64 \pm 0.09) \times 10^{-6}. \quad (2.18)$$

Using (2.14) and the NNLO calculations in [11] for  $P_c(X)$ , the branching ratio of  $\pi \nu \bar{\nu}$  is predicted to be

$$\mathcal{B}(K^+ \rightarrow \pi^+ \nu \bar{\nu}) = (8.0 \pm 1.1) \times 10^{-11} \quad (2.19)$$

within the SM. It should be noted that, for an uncertainty of 15% in (2.19), the theoretical uncertainty is  $\sim 7\%$  at present, mainly due to the charm quark contribution.

The measurement of  $\text{BR}(K^+ \rightarrow \pi^+ \nu \bar{\nu})$  is regarded to be one of the cleanest ways to extract  $|V_{td}|$  for the following reasons:

- Long-distance contributions to the branching ratio are negligible (at most  $10^{-13}$ ) [14], [15].
- The uncertainty from the hadronic matrix element has been removed by using  $BR(K^+ \rightarrow \pi^0 e^+ \nu)$ .
- The remaining theoretical uncertainties (7%) are relatively small and reliable as compared with the errors in other  $K$  and  $B$  decays.

## 2.3 Physics beyond the Standard Model

Since  $K^+ \rightarrow \pi^+ \nu \bar{\nu}$  is a second order process, a precise measurement of the branching ratio can investigate whether there are non-SM effects involved in this decay mode or not. A possible discrepancy between the measured branching ratio and the SM prediction would indicate the existence of new physics beyond the SM. In the past, when the  $K^+ \rightarrow \pi^+ \nu \bar{\nu}$  BR was first measured, its value put limits in fourth generation theories, SUSY and fifth force theories ([14]). Nowadays that the Unitarity triangle measurements from the  $B$  sector are precise, what can be performed is to determine  $\rho$  and  $\eta$  independently from the  $K$  and  $B$  decays, as shown in Fig. 2.6.

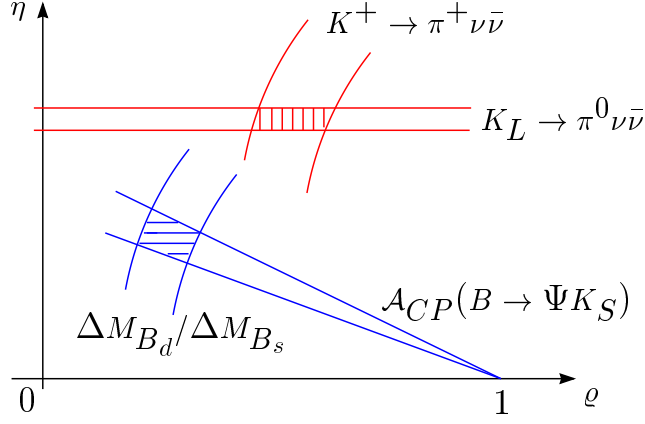


Figure 2.6: Schematic determination of the unitarity triangle apex  $(\rho, \eta)$  from the B system (blue) and from the  $K \rightarrow \pi\nu\bar{\nu}$  decays (red). Both determinations can be performed with small theoretical uncertainties, therefore any discrepancy between them, as illustrated in this hypothetical example [16], would indicate new physics.

The information that is currently being used to constrain the unitarity triangle is obtained only from the charged current processes (i.e. tree-level amplitudes) and the  $\Delta S, \Delta B = 2$  loop-induced processes. For example, determinations of  $\rho$  and  $\eta$  can be obtained from the  $B_d^0 - \bar{B}_d^0$  mixing and the CP violating asymmetry in  $B_d^0 \rightarrow J/\psi K_s^0$ , both of which are mediated by  $\Delta B = 2$  loop-induced processes. On the contrary,  $K^+ \rightarrow \pi^+ \nu \bar{\nu}$  and  $K_L^0 \rightarrow \pi^0 \nu \bar{\nu}$  are mediated via the  $\Delta S = 1$  FCNC transition. New physics may therefore be seen in a discrepancy between  $K$  and  $B$  decays [16].

Several SM extensions to new physics would affect the  $\pi\nu\bar{\nu}$  branching ratio. In the Minimal Flavor Violation (MFV) model, the  $\pi\nu\bar{\nu}$  branching ratio is allowed to be as large as  $1.9 \times 10^{-10}$  [17]. In this model, the origin of CP violation and quark “mixing” comes from the CKM matrix as in the SM, and from process-independent universal master functions, which are real and which in the SM reduce to the Inami-Lim functions [19].



In the "Enhanced  $Z^0$  Penguin" model [18], where a new imaginary phase is introduced, the  $\pi\nu\bar{\nu}$  branching ratio is expected to be almost the same as the SM prediction. However, the  $K_L^0 \rightarrow \pi^0\nu\bar{\nu}$  branching ratio is predicted to be  $(3.1 \pm 0.1) \times 10^{-10}$ , which is 10-times larger than the SM prediction, and is close to the Grossman-Nir limit,  $BR(K_L^0 \rightarrow \pi^0\nu\bar{\nu})/BR(K^+ \rightarrow \pi^+\nu\bar{\nu}) < 4.4$  [20]. Another interesting prediction derived from this model is that the value of  $\sin 2\beta$  obtained from  $K \rightarrow \pi\nu\bar{\nu}$  is not equal to that obtained from  $B_d^0 \rightarrow J/\psi K_s^0$ .

Since a detection of the  $K^+ \rightarrow \pi^+\nu\bar{\nu}$  decay in practice detects the transition  $K^+ \rightarrow \pi^+ + \text{nothing}$ , limits can also be set for the  $K^+ \rightarrow \pi^+ X^o$ , where  $X^o$  is a massless weakly interacting particle such as a familon [14]. Such a limit from the E949 measurements currently exists at  $BR(K^+ \rightarrow \pi^+ X^o) < 0.73 \times 10^{-10}$ . Limits have also been set for massive  $X^o$ .

It is worth mentioning that the lower  $\pi^+$  momentum phase space studied in this thesis, is also sensitive to a different shape of the pion spectrum, resulting from scalar or tensor interactions as opposed to the SM vector spectrum. Therefore, extra information in addition to just the value of the BR can be extracted by such a measurement.

# Chapter 3

## The experiment

The rare decay  $K^+ \rightarrow \pi^+ \nu \bar{\nu}$  has been searched for by experiments for more than thirty years, but only BNL's E787 [22] and E949 [21] have managed to find events and get a central value for the Branching Ratio. Figure 3.1 summarizes the history of this search.

The BR found by E787 and E949 is consistent with the SM prediction (equation 2.19), but the central value is twice the SM prediction. It would be worth to confirm the consistency between the measured branching ratio and the SM prediction by running the E949 experiment longer to achieve better precision, as shown by the last point in Fig. 3.1.

### 3.1 Experimental Overview

The experimental signature of the  $K^+ \rightarrow \pi^+ \nu \bar{\nu}$  decay is a single  $\pi^+$  track and no other particle from a  $K^+$  decay, because the two neutrinos in the final state cannot be detected in the apparatus.  $K^+ \rightarrow \pi^+ \nu \bar{\nu}$  is a three-body decay with

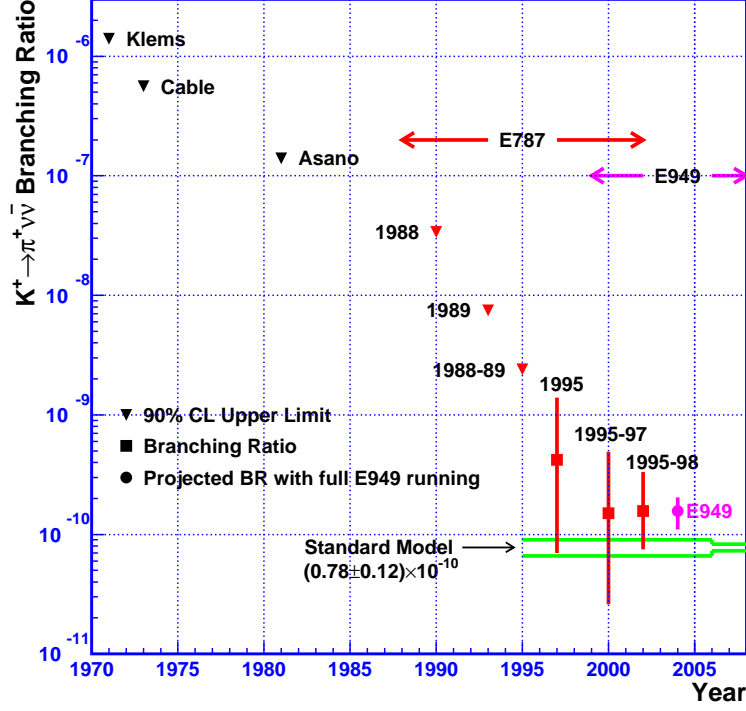


Figure 3.1: History of the search for  $K^+ \rightarrow \pi^+ \nu \bar{\nu}$ . The vertical axis is the  $\pi \nu \bar{\nu}$  Branching Ratio and the horizontal one the publication year. The triangles represent upper limits for the BR at the 90% confidence level, the boxes represent the central value of the measured BR and the dot represents an expected value with the full E949 running period, assuming that the central value of the branching ratio remains what the combined E787 and E949 results have found up to now,  $BR = (1.47^{+1.30}_{-0.89}) \times 10^{-10}$  [23]. The error bars show the 68% CL intervals.

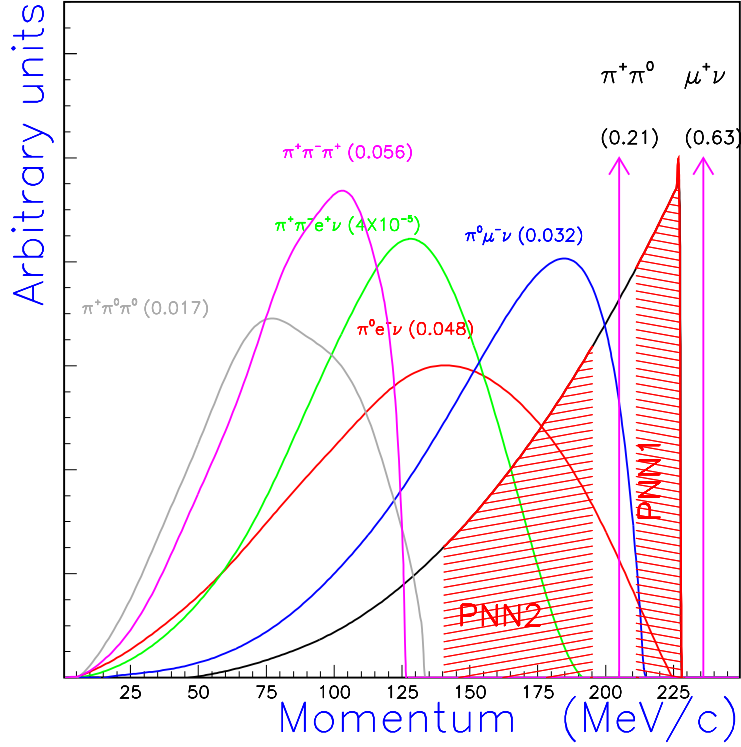


Figure 3.2: Momentum spectra of the charged product of the top 7  $K^+$  decay modes. The SM  $K^+ \rightarrow \pi^+ \nu \bar{\nu}$  spectrum is also shown (not in scale).

a maximum momentum of 227 MeV/c, and it has been traditionally searched for by the experiments E787 and E949 in two kinematic regions: “PNN1” and “PNN2” (the region studied in this analysis). The momentum definition of these regions, together with the momentum spectra of the outgoing charged particle (pion or muon) of the main background mechanisms relevant to PNN2, are shown in Fig. 3.2. Their Branching Ratios are listed in Table 3.1. As it can be seen, the upper bound of PNN2 is very close to the momentum (and energy and range) of the major 2-body decay  $K_{\pi 2}$ .

| Background  | Branching Ratio ( $\times 10^{-3}$ ) |
|---|--------------------------------------|
| $K^+ \rightarrow \pi^+ \pi^0 (K_{\pi 2})$               | 209.2                                |
| $K^+ \rightarrow \pi^+ \pi^0 \gamma (K_{\pi 2 \gamma})$ | 0.275                                |
| $K^+ \rightarrow \pi^0 \mu^+ \nu (K_{\mu 3})$           | 33.2                                 |
| $K^+ \rightarrow \mu^+ \nu \gamma (K_{\mu 2 \gamma})$   | 6.2                                  |
| $K^+ \rightarrow \pi^+ \pi^- e^+ \nu (K_{e 4})$         | 0.041                                |
| Beam backgrounds  | -                                    |
| CEX: $K^+ n \rightarrow K^0 p$                          | $R_{K_L} = 2.8 \times 10^{-5}$       |
| $K_L^0 \rightarrow \pi^+ \mu^- \bar{\nu}$               | 135.0                                |
| $K_L^0 \rightarrow \pi^+ e^- \bar{\nu}$                 | 194.0                                |

Table 3.1: Background processes to the decay  $K^+ \rightarrow \pi^+ \nu \bar{\nu}$  in the kinematic region below the  $K_{\pi 2}$  peak, with their Branching Ratios [8]. CEX stands for Charge Exchange, and  $R_{K_L}$  is the  $K_L$  production rate as found in [24].

Since, in the SM, the branching ratio of  $K^+ \rightarrow \pi^+ \nu \bar{\nu}$  is expected to be at  $\sim 10^{-10}$ , all other kaon decay modes, as well as beam pions that scatter into the detector acceptance, could be sources of background. Therefore, precise kinematic measurements, positive particle identification of the incoming  $K$  and the outgoing  $\pi$ , and efficient vetoing of all other decay products (mainly photons) is required to suppress these backgrounds to an acceptable level. The E949 detector has been designed with these requirements in mind, specifically:

- The beam intensity should be as high as the detector and data acquisition system could handle, since the decay rate is extremely rare.
- Pion contamination in the kaon beam should be reduced to be as low as possible to minimize events with the scattered pion beam (Pion Scattering events).
- Detectors along the beam path are installed, in order to assure the identity of the incoming particle (particle identification, PID) and to veto on

other particles arriving around the Kaon decay time.

- A series of detectors give precise kinematic measurements, in order to suppress the  $K^+ \rightarrow \pi^+ \pi^0$  background: the active Target (TG) and two momentum degraders are designed to stop the incoming Kaon and measure its arrival time. The TG is surrounded by a drift chamber (UTC) immersed in a 1T magnetic field, in order to measure the outgoing particle momentum. Then the charged decay product comes to a rest in a stack of scintillators (RS), where its total energy and range are measured.
- The charged particle should be identified as  $\pi^+$ , which is achieved by observing the  $\pi^+ \rightarrow \mu^+ \rightarrow e^+$  decay sequence in the counter in which it stops and decays. This helps to suppress muon backgrounds.
- Any particles other than  $\pi^+$  from  $K^+$  decay should be detected and rejected. Photon veto detectors cover the detector at  $4\pi$ , and the TG can detect extra short-range charged decay products.

The BNL-E949 experiment [21] is a successor to the experiment BNL-E787 [22], whose data taking was completed in 1998. The beam and apparatus are similar to those of E787, but several upgrades have been made:

### **Beam**

- The proton intensity increased by a factor of two compared to E787, which resulted in a twice higher kaon intensity than that in E787.

### **Detector**

- A new lead/scintillator sandwich sampling calorimeter (Barrel Veto Liner, BVL) was installed in the barrel region, which added 2.3 radiation lengths to the photon vetos. Also installed were photon detectors that cover small solid angles near the beam line: the Active Degradar (AD), Upstream Photon Veto (USPV) and Downstream Photon Veto (DSPV).
- One third of the plastic scintillators in the  $\pi^+$  range counters were replaced, which enabled us to achieve greater light output.
- A gain monitor system, operated by blue LED flashers, was installed in the RS. The gain fluctuations of a phototube could be tracked down spill by spill, or even within a spill. This resulted in more precise energy calibration.
- The electronics for the drift chamber and straw chambers embedded in the RS were modified to meet the high rates.
- Signals from several beam counters were read out by waveform digitizers. Signal pileup due to the high beam intensity was solved by pulse-shape analysis.

### **Trigger and DAQ**

- The level 0 trigger board was upgraded [25].
- Digital mean-timer modules were used for online photon rejection [25]. This helped to avoid any accidental loss in the trigger.

In the following sections, details concerning the E949 experiment are described.

## 3.2 The beam

The  $K^+$  beam is produced by a high-intensity proton beam from the Alternating Gradient Synchrotron (AGS) at BNL. A schematic view of the AGS accelerator complex is shown in Fig. 3.3.

Protons are accelerated to a momentum of 21.5 GeV/c.  $65 \cdot 10^{12}$  protons (Tp) are extracted in a 2.2-second long "spill" once every 5.4 seconds from the AGS. The slow extracted beam (SEB) is transported to the kaon production target for E949. The platinum production target extends 6 cm in the beam direction, and is located on a water-cooled copper base. Under typical AGS running conditions, 65 Tp hit the production target every 2.2 second spill at 21.5 GeV/c.

The Low Energy Separated Beam line III [26] (LESBIII, shown in Fig. 3.4) collects and focuses kaons produced at the production target. The beam emitted toward 0 degrees contains about 500 pions and 500 protons for every kaon, and is momentum-selected by a dipole magnet (D1 in Fig. 3.4). Two electrostatic separators (Separators 1 and 2 in Fig. 3.4) sweep pions and protons out of the beam. The resulting beam is further selected by a second dipole magnet (D2 in Fig. 3.4). LESBIII contains a number of focusing quadrupole (Q1-10), sextupole (S1-3), and octupole (O1) magnets and collimating slits, and has a total length of 19.6 m from the production target to the E949 target. Kaons with 710 MeV/c momentum were transported down this beamline.

The angular acceptance of LESBIII is 12 msr and the momentum acceptance is 4.5% FWHM. LESBIII provides the world's highest-intensity kaon beam of 710 MeV/c with a flux of about  $5 \times 10^5$   $K^+$ 's per Tp on the production



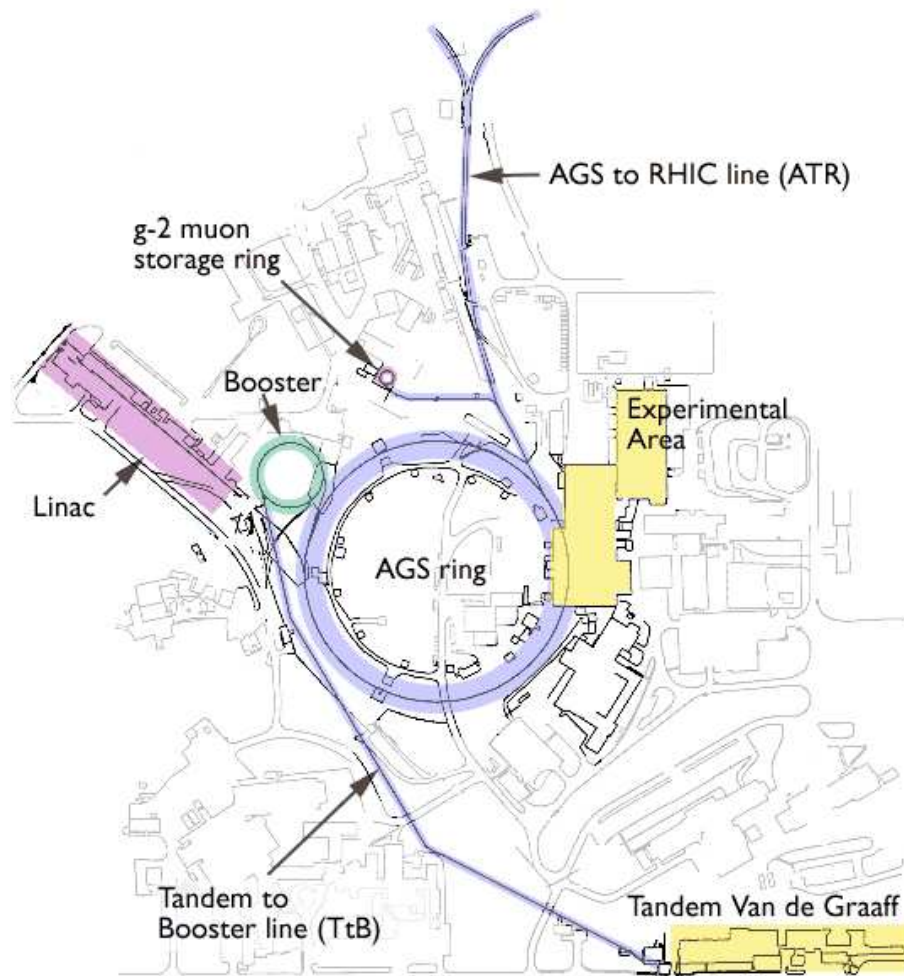


Figure 3.3: Schematic view of the AGS complex, which consists of a 200 MeV LINAC, a booster and a synchrotron. The secondary beam lines are located in the experimental area.

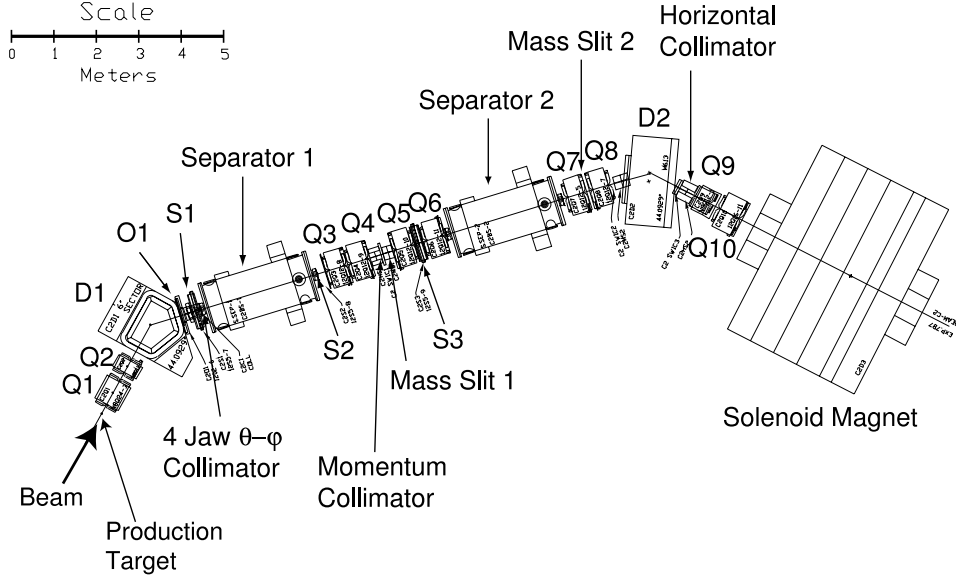


Figure 3.4: Low-energy separated beam line III at BNL.

target. The  $K^+ : \pi^+$  ratio in the beam is about 3:1<sup>1</sup>. Proton contamination is negligible due to a large deflection of protons by the separators. Under the typical AGS running condition of 45 Tp on the production target per spill,  $1.3 \times 10^7$   $K^+$ 's emerge from LESBIII.

### 3.3 The detector

A side view of the E949 detector is shown in Fig. 3.5. The E949 detector consists of beam instrumentation, a target of scintillating fibers, a central drift chamber, a stack of plastic scintillators (Range Stack), and hermetic photon detectors.

The whole detector is surrounded by a solenoid magnet with a 1 Tesla magnetic field along the beam line for momentum measurements. The coordinates

<sup>1</sup>The  $K/\pi$  ratio in E787 was 4:1. This worse  $K/\pi$  ratio was due to a problem with the second separator.



of the detector are defined such that the origin is at the center of the target; the z-axis is along the beam direction and the x-axis and y-axis are set in the horizontal and vertical directions, respectively.

### 3.3.1 Beam detectors

Since the beam intensity is very high and the beam contains pions with a ratio of  $K^+ : \pi^+ = 3 : 1$ , a single kaon entering the target should be identified by the beam instrumentation. It has three roles: kaon identification, slowing down the kaon, and the detection of extra beam particles if they exist at the kaon beam time or the kaon decay time. The beam instrumentation from upstream to downstream consists of a Čerenkov counter, the Upstream Photon Veto detector, beam wire chambers, degraders and a beam hodoscope.

The kaon beam from LESBIII first enters the Čerenkov counter located just downstream of the last quadrupole magnet (Q10) and 2 m upstream of the target. A side view of the Čerenkov counter is shown in Fig. 3.6.

The reflection index ( $n$ ) of the radiator is 1.49, which gives a threshold of Čerenkov radiation  $\beta_{\check{C}} = 1/n = 0.671$  and a reflection threshold  $\beta_{ref} = \sqrt{\frac{1}{n^2-1}} = 0.905$ . Kaons and pions with a momentum of 710 MeV/c have  $\beta_{K^+} = 0.821$  and  $\beta_{\pi^+} = 0.981$ , respectively. Therefore, the Čerenkov light from kaons is not reflected at the inner surface of the radiator, but the Čerenkov light from pions is reflected. The light from a kaon exits the radiator and is reflected by a parabolic mirror to the outer ring of 14 photomultiplier (PMT) tubes (Kaon Čerenkov Counter), while that from a pion is internally reflected within the radiator and detected in the inner ring of 14 PMTs (Pion Čerenkov

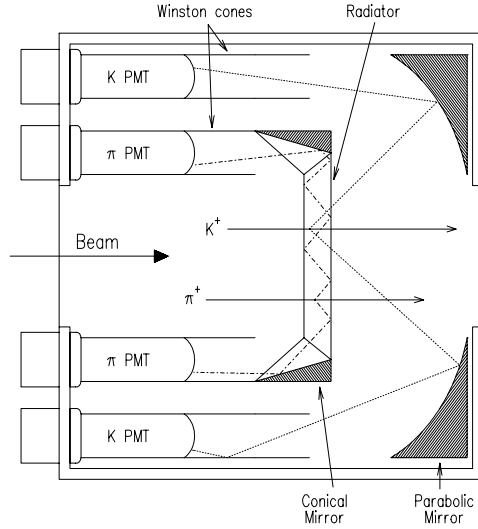


Figure 3.6: Side view of the Čerenkov counter.

Counter).

The PMT signals are fed to time-to-digital converters (TDCs) via discriminators, as well as to 500 MHz transient digitizers based on gallium-arsenide (GaAs) charge-coupled devices (CCDs) [27]. The pulse-height information in every 2 ns interval is recorded in the CCDs to reproduce the time development of the pulses.

A charged particle passing through the Čerenkov counter gives a signal in a number of PMTs in the Kaon or Pion Čerenkov Counters; PMT hits coincident with each other are called a "cluster". A kaon is identified by requiring that the Kaon Čerenkov Counter has a hit cluster and the Pion Čerenkov Counter has no hit cluster.

Two incoming particles close in time can give a signal in the same PMTs, and a pileup signal may not be found by the TDCs. In this case, the pulse shapes recorded in the CCDs can be used to discriminate such pileup signals.

Right downstream of the Čerenkov counter there is the Upstream Photon Veto (USPV) detector. This is made of 12 layers of  $28.4\text{ cm}^2$  plastic scintillator sheets, 2 mm thick, alternating with 1 mm (the 6 most downstream ones) or 2 mm (the 5 most upstream ones) thick lead sheets. The downstream-most layer of lead was replaced by 2.2 mm thick copper, which formed part of the box holding the layers together. The upstream side of the box is made by 3.175 mm thick aluminum. The detector has a 175 mm wide by 40 mm high slot in the center to allow the beam to pass through, and is divided horizontally in 2 modules, each read out by one PMT. Each scintillator layer was read out by 21 wavelength shifting (WLS) fibers going to one of these 2 PMTs. Then the signals from each PMT were fed to a TDC, an ADC and a CCD.

Although the USPV was originally designed as a photon veto detector for the photons that might escape in the beam direction, it was found that its rate was overwhelmed by beam particles and its segmentation into only 2 modules did not give enough space resolution to distinguish between beam particles and upstream-going photons. Therefore its time, energy and CCD pulse information was used to veto beam particles coincident with the kaon decay time.

Behind the USPV, two Beam Wire Projection Chambers (BWPCs) are located, and allow to monitor the beam profile and to identify multiple incoming particles. Cross-sectional views of the BWPCs are shown in Fig. 3.7.

The first chamber (BWPC1) consists of 3 planes of anode wires, labeled U, V and X. The direction of the wires in the X-plane is vertical, and in the U- and V-planes are at  $\pm 45^\circ$  to the vertical plane respectively. The wires are made of gold-plated tungsten with 0.012 mm diameter. The BWPC1 has 72,

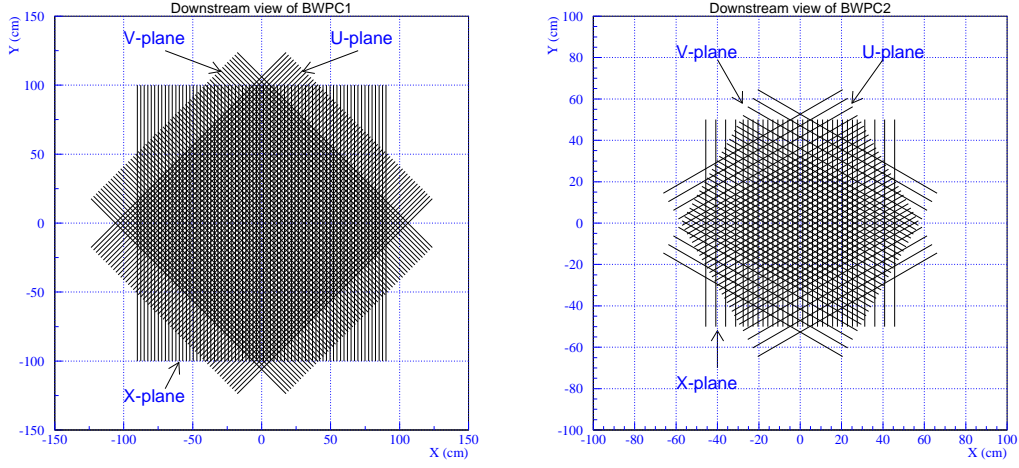


Figure 3.7: Cross-sectional view of the two beam wire chambers (BWPCs): BWPC1 (left) and BWPC2 (right).

60 and 60 readout channels for the X-, U- and V-planes, respectively, with a 2.54 mm wire spacing. The spatial resolution is 1.54 mm, and the active area is 178 mm (horizontal) by 50.8 mm (vertical). The cathode foils are 0.025 mm thick aluminized mylar coated with carbon. The anode-cathode distance is 3.175 mm, and the total thickness of the BWPC1 is approximately 56 mm. The BWPC1 is filled with a mixture of CF<sub>4</sub> (80%) and Isobutane (20%).

The second chamber (BWPC2) is located at 90 cm downstream of the BWPC1 and consists of three planes (U, V and X). Each plane has 24 readout channels with a 2.40 mm wire spacing in the central region (57.6 mm) and 8 channels with a 4.80 mm wire spacing in the peripheral region (19.2 mm on each end). The cathode foils are 0.008 mm single-side aluminized mylar coated with carbon. The anode-cathode distance is 1.5875 mm. The BWPC2 is filled with the same gas as BWPC1.

Downstream of the BWPCs, cylindrical degraders are located for slowing

down the kaons so that they come to rest in the target. The degraders have inactive and active parts. The upstream inactive degrader is made of 111.1 mm long beryllium oxide (BeO) and 4.76 mm Lucite. The thickness of the Inactive Degradar is appropriate for stopping kaons with a momentum of 710 MeV/c, in combination with the Active Degradar and (part of) the Target. BeO, with high density and low atomic number, minimizes multiple scattering.

The downstream active degrader (AD) consists of 40 layers of 2 mm thick scintillator disks (139 mm in diameter) alternating with 2-mm thick copper disks (136 mm in diameter). The AD is split into 12 azimuthal segments, and the scintillation light in each segment is sent to a single PMT through 14 wave length shifting (WLS) fibers running in grooves cut into the perimeter of the disks. The PMT outputs are fed to TDCs and CCDs. The signals from 4 PMTs are multiplexed and fed to a single analog-to-digital converter (ADC). Using this information, the AD has the ability to identify the beam particles and to detect activity coincident with kaon decays.

After passing through the degraders, just in front of the target, a beam hodoscope (B4 Hodoscope) detects the incoming particle and identifies it as a kaon or pion by measuring the energy deposit. An end view of the B4 Hodoscope is shown in Fig. 3.8.

The B4 Hodoscope consists of two planes (U- and V-plane, 119 mm in diameter) to provide position information. Each plane has 12 scintillator fingers. The cross section of the finger has a "Z-shape", as shown in Fig. 3.9, with a 6.35-mm thick middle part and 3.175-mm thick edge parts. This shape allows the B4 Hodoscope to have no inactive region and improves its spatial resolution.



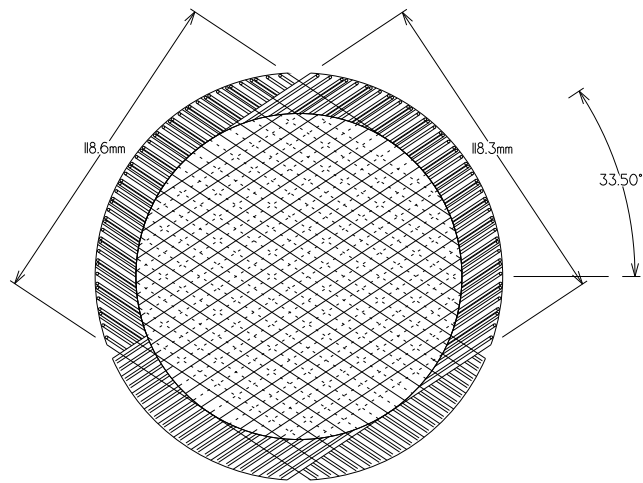


Figure 3.8: End view of the B4 Hodoscope.

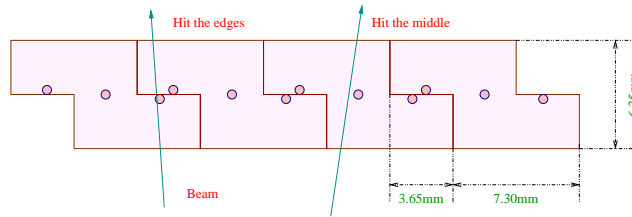


Figure 3.9: Schematic cross section of the B4 Hodoscope.

In each finger, 3 WLS fibers are embedded and fed to a single PMT that is read out by TDCs, ADCs and CCDs. A double-pulse fitting is performed to the signals recorded in the CCDs in order to detect pileups. The time development of the output signals is fitted with a single- or double-pulse assumption, which allows to reject events if the fitted pulse is more likely to be a double pulse and the time of the second pulse is coincident with the  $K^+$  decay time.

The B4 is surrounded by a ring of scintillator, the Ring Veto (RV), which covers the crack between the B4 and the I-Counter (described later). It is 3.27 mm thick, with an outer diameter of 145.5 mm, and as long as the B4 hodoscope. The RV is segmented vertically to 2 modules, each one read out separately and with its signals sent to a TDC, an ADC and a CCD.

### 3.3.2 Target (TG)

After passing through all the beam elements and being slowed down by the degraders,  $3.9 \times 10^6$  kaons per spill enter the scintillating fiber target located in the center of the spectrometer. Kaons lose more energy, come to rest, and decay in the target.

The TG consists of 413 5-mm square and 3.1-m long plastic scintillating fibers that are bundled to form a 12-cm diameter cylinder. A number of smaller fibers (called "edge fibers") fill the gaps near the outer edge of the TG. End and side views of the target are shown in Fig. 3.10.

Each of the 5.0-mm fibers is connected to a PMT, whereas the edge fibers are multiplexed into groups of 12 and each group is connected to a single PMT. The PMTs are read out by ADCs, TDCs and CCDs. Kaons, whose

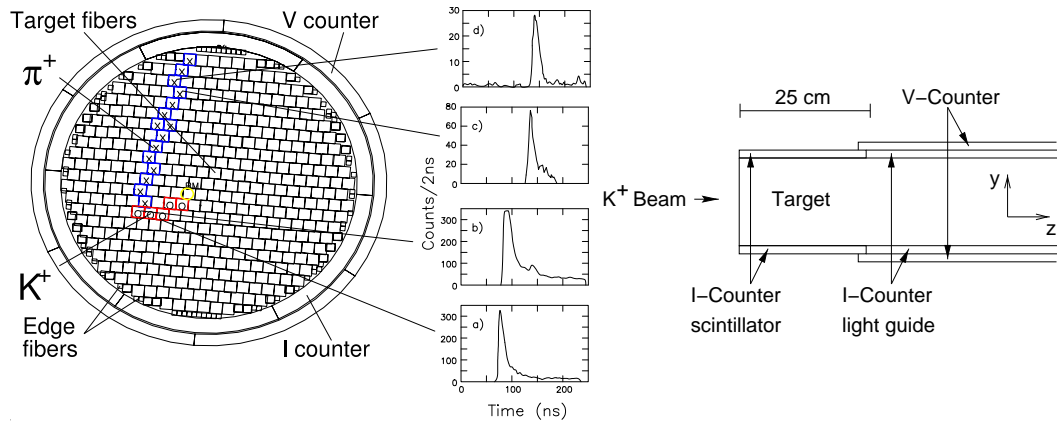


Figure 3.10: End (left) and side (right) views of the target. The CCD pulse-shape information is used to find kaon and pion clusters, as shown in the left figure. The lower two plots ((a) and (b)), are CCD pulses for a kaon, and the upper two plots ((c) and (d)), are those for a pion. Two layers of 6 plastic scintillators, the I-Counter (IC) and V-Counter (VC), surround the target.

velocities are small, typically lose a large amount of energy (few tens MeV) in each fiber, while pions from kaon decays lose about 1 MeV per fiber, since they travel as minimum ionizing particles (MIPs). Pattern recognition is performed to find fibers that belong to a kaon's path or a pion's path. The CCD pulse information is used to find clusters for kaons (kaon fibers) and pions (pion fibers). A double-pulse fitting is also performed to find the fiber where a  $K^+ \rightarrow \pi^+$  decay vertex is located, since the outgoing pion leaves a second pulse, and to estimate the energy loss and thus the range of the pion included in the kaon fiber.

The fiducial region of the target is defined by two layers of 6 plastic-scintillating counters that surround the target (see Fig. 3.10). The inner scintillators, called I-Counter (IC), tag charged decay products for a trigger before they enter the drift chamber. The IC is 6.4 mm thick at an inner radius of 6.0 cm, and extends 24 cm downstream from the upstream face of the target.

Each scintillator is instrumented with a PMT, and is read out by an ADC, a TDC and a 500 MHz transient digitizer (TD) based on flash ADC [28].

The outer scintillators, called the V-Counter (VC), overlap the downstream edge of the IC by 6 mm, and serve to detect particles that decay downstream of the fiducial region of the target. The VC is 5 mm thick and 1.96 m long, and is staggered with respect to the IC. Each scintillator is instrumented with a PMT, which is read out by an ADC and a TDC.

### 3.3.3 Drift Chamber (UTC)

The drift chamber, called "Ultra Thin Chamber" (UTC), is located just outside of the IC. The whole E949 spectrometer is in a 1 Tesla magnetic field. Positively charged particles are bent clockwise in the view from downstream. The primary functions of the UTC are measuring the momentum of charged particles and providing a matching between the tracks in the target and in the Range Stack.

The UTC has a length of 51 cm and inner and outer radii of 7.85 cm and 43.31 cm respectively. It is composed of 12 layers of drift cells, grouped into 3 superlayers. The inner superlayer has 4 layers of 48 cells, the middle superlayer has 4 layers of 96 cells, and the outer superlayer has 4 layers of 144 cells (shown in Fig. 3.11).

Each cell is composed of 9 wires strung axially. A single anode wire, made of gold-coated tungsten with a 20  $\mu\text{m}$  diameter, is surrounded by 8 cathode wires made of gold-coated aluminum with a 100  $\mu\text{m}$  diameter, which are arranged in a square. Adjacent cells share the cathode wires at the boundaries. The cells

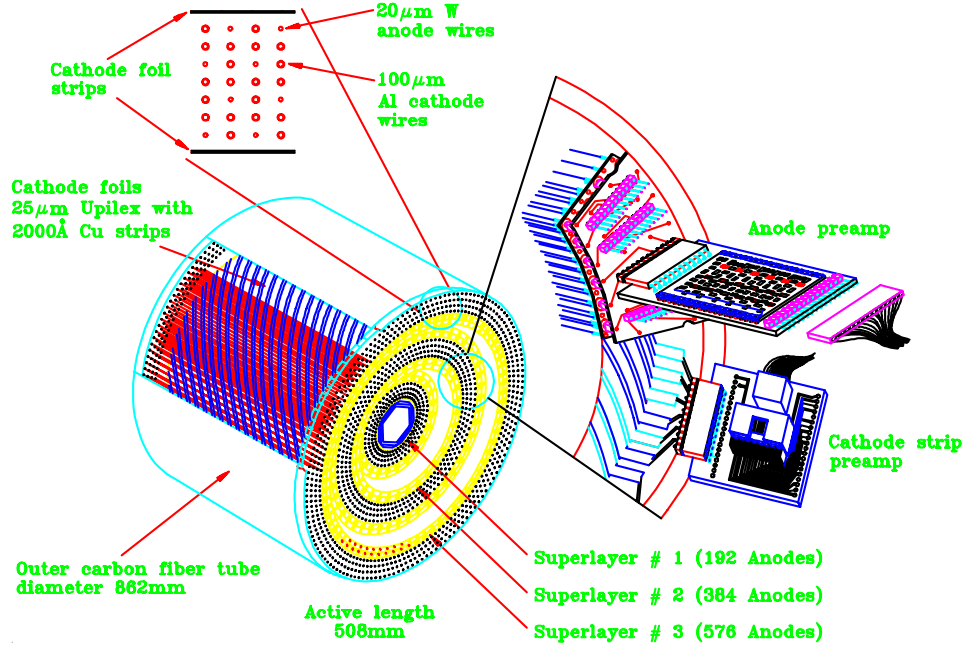


Figure 3.11: Schematic view of the Ultra Thin Chamber.

in each layer are staggered by one-half cell with respect to the neighboring layers, in order to resolve a left-right ambiguity. The superlayers are filled with a mixture of argon (49.6%), ethane (49.6%) and ethanol (0.8%) gases. The cathode wires are grounded, and the anode wires are maintained at 2 kV (gain =  $8 \times 10^4$ , drift velocity = 5 cm/ $\mu$ s). Each anode wire is instrumented with an ADC and a TDC. The drift time to the anode wires provides  $(x, y)$  positions for charged tracks.

The inner and outer radii of each superlayer have helical arrays of cathode strips, whose pitch angle is  $45^\circ$ . The strips, with a width of 7 mm, are made of 1200 Å thick copper coated with 300 Å thick nickel, and are mounted on a 25  $\mu$ m thick Kapton foil. The separation between the strips is 1 mm. The cathode foils have 48, 72, 108, 144, 180, and 216 strips from the inner to the outer layers, respectively. The Z position of a charged track is measured from

the energy-weighted mean of the cluster of hit strips. The resolution for a z-position measurement is about 1 mm. Each cathode strip is instrumented with an ADC and a TDC.

There are 2 inactive regions filled with nitrogen gas between the 3 super-layers. The differential pressure in the 5 gas volumes supports the cathode foils (excluding the innermost and outermost foils, which are held in place by support tubes). The total mass in the active region of the UTC, excluding the inner and outer support tubes and innermost and outermost foils, amounts to  $2 \times 10^{-3}$  radiation lengths.

The momentum resolution ( $\Delta P/P$ ) for the two body decays  $K_{\pi 2}$  and  $K_{\mu 2}$  is 1.1% and 1.3%, respectively. More information on the UTC is given in [29].

### 3.3.4 Range Stack (RS)

The primary functions of the Range Stack (RS) are energy and range measurements of charged particles and their identification. It is also used as a Photon Veto detector, with  $\tilde{0.8}$  radiation lengths. The RS is located just outside the UTC at an inner radius of 45.08 cm and an outer radius of 84.67 cm. It consists of 19 layers of plastic scintillators, azimuthally segmented into 24 sectors (see Fig. 3.12). Conventionally, the 24 sectors are grouped into 6 “hextants” of 4 sectors each (sectors 1-4, 5-8, 9-12, 13-16, 17-20, 21-24).

The scintillators of layers 2-18 have a thickness of 1.905 cm and a length of 182 cm. The scintillators of layer 19 have a thickness of 1 cm. This layer is mainly used to veto charged particles with long range by requiring that they do not reach the layer-19 scintillators. The scintillation light in the layer 2-19

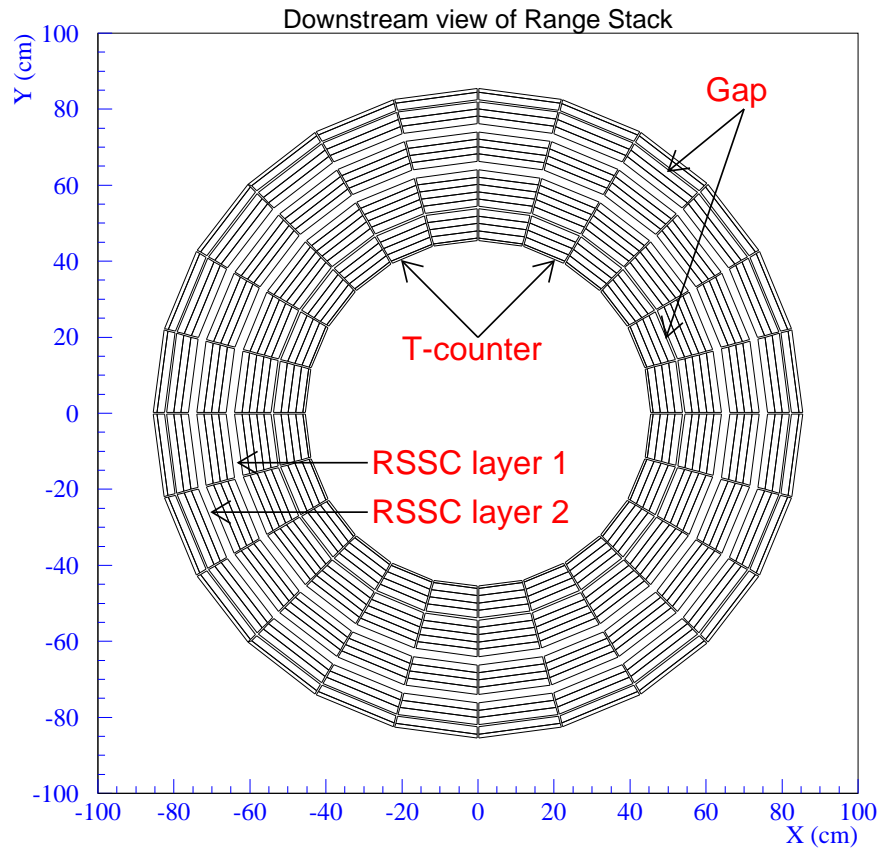


Figure 3.12: End view of the Range Stack. The two layers of the Range Stack Straw Chambers are located after layers 10 and 14.

counters is led by light guides to PMTs at both the upstream and downstream ends.

The innermost counters, called T-Counters, have a thickness of 6.35 mm and a length of 52 cm. 17 WLS fibers are embedded in each scintillator for read out, and are grouped and fed to a single PMT at each end. The T-Counter signals are used to produce a trigger signal and to define the fiducial region as  $2\pi$  sr solid angle, which is almost the same as the solid-angle acceptance of the UTC.

Each PMT of the RS scintillators is read out by an ADC and a TDC. Signals from 4 PMTs at the same end, same hexant and same layer are multiplexed and read out by a single TD. The signals are demultiplexed in the offline event reconstruction by using TDC information in order to determine which counter the signal came from. The ADCs record charges in a 100 ns window, and the TDCs record the time of hits in the range of 10  $\mu$ s. The TDs record pulse heights of PMT signals in 2 ns intervals (500 MHz sampling) for up to 2  $\mu$ s to provide information on the time development of the pulses. This 500 MHz sampling provides detailed information about the pulse shapes, which enables the separation of two pulses as close as 5 ns in time, by performing an offline pulse fitting. The gate width of the TDs is narrower than that of the TDCs in order to reduce the data size.

The time of a hit in the RS counters is obtained from the average of the upstream and downstream TDC times, and the z position of the hit is obtained from their time difference. In the case that TDC hit information is missing, the hit time information is complemented with the corresponding TD information if available.



The  $\pi^+$ 's from the  $\pi\nu\bar{\nu}$  decay in the PNN2 region, whose momentum is up to 199 MeV/c, come to rest in the RS. Pions with 199 MeV/c can propagate into plastic scintillator by roughly 28 cm. The total radial thickness of the RS and target is 45 cm, therefore most of the  $\pi\nu\bar{\nu}(2)$   $\pi^+$ 's (which are also bent in the 1 Tesla magnetic field) lose their entire kinetic energy and come to rest by the 10<sup>th</sup> layer of the Range Stack. On the other hand, the momentum of  $\mu^+$ 's from kaon decays at rest are at most 236 MeV/c. Muons with 236 MeV/c (such as  $\mu^+$ 's from  $K_{\mu 2}$  decays) can propagate into plastic scintillator by 54.3 cm. Hence,  $K_{\mu 2}$  decays are suppressed by requiring that charged tracks come to rest by the 12<sup>th</sup> layer of the RS.

However, the  $\mu^+$ 's from  $K_{\mu 2\gamma}$  and  $K_{\mu 3}$  decays could come to rest earlier in the RS. Besides, a  $\pi^+$  can decay in flight and the secondary  $\mu^+$  may come to rest in the RS. For this reason, further identification of  $\pi^+$  in the RS is performed by observing the  $\pi^+ \rightarrow \mu^+ \rightarrow e^+$  decay sequence in the TDs and TDCs of the counter where the  $\pi^+$  comes to rest (the “stopping counter”). Typical TD pulses in and around the stopping counter for a pion track are shown in Fig. 3.13.

The  $\mu^+$  from the  $\pi^+ \rightarrow \mu^+ \nu_\mu$  decay at rest has a kinetic energy of 4 MeV (equivalent range in plastic scintillator is 1 mm) and rarely goes out of the stopping counter. On the contrary, the  $e^+$  from the  $\mu^+ \rightarrow e^+ \nu_e \bar{\nu}_\mu$  decay at rest has a kinetic energy of up to 52 MeV, and the  $e^+$  track loses kinetic energy not only in the stopping counter, but also in the neighboring counters. The  $\pi^+ \rightarrow \mu^+$  decay at rest, whose lifetime is 26 ns, is detected by using TD information of the stopping counter by performing a double-pulse fitting, while the sequential  $\mu^+ \rightarrow e^+$  decay, whose lifetime is 2.2  $\mu$ s, is detected by using

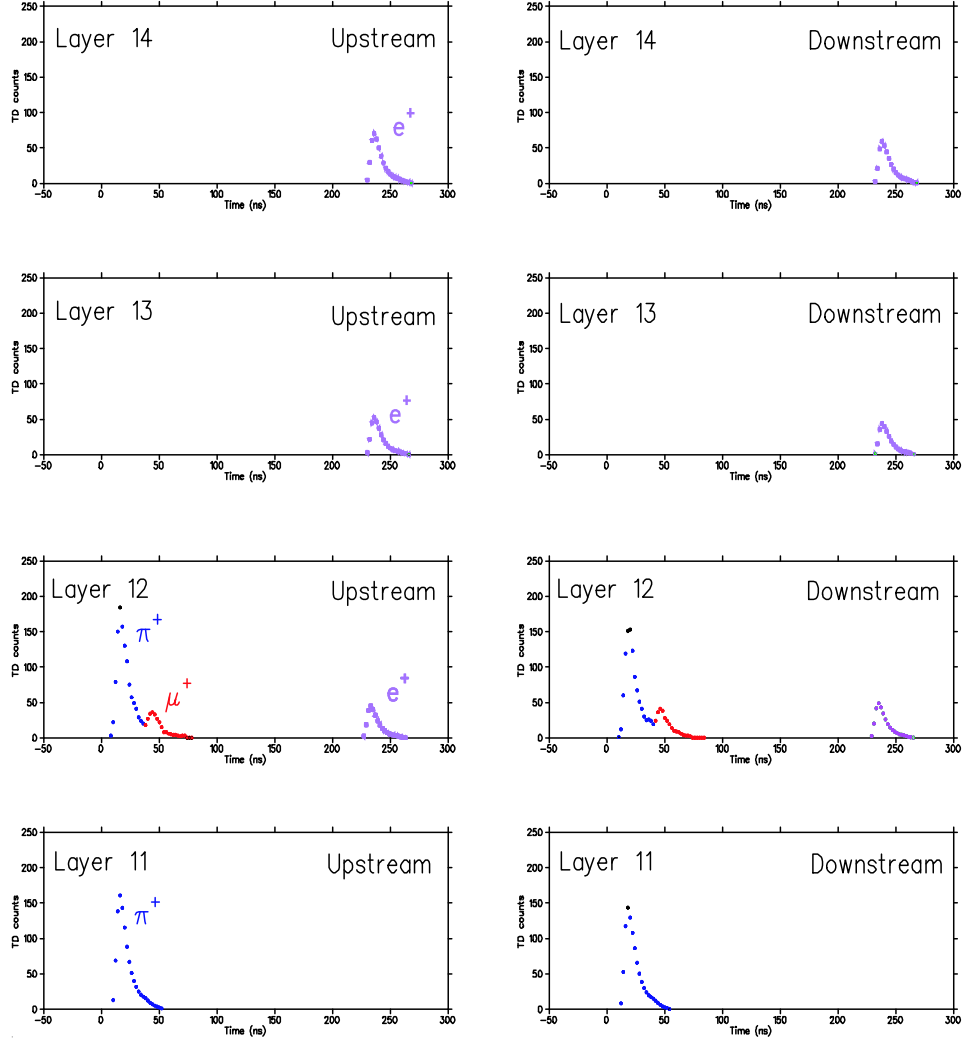


Figure 3.13: Pulses in and around the stopping counter recorded by the TDs of the upstream and downstream ends. The  $\pi^+ \rightarrow \mu^+ \rightarrow e^+$  decay sequence is recorded in the stopping counter (Layer 12 in this case). The  $\mu^+$  from the  $\pi^+ \rightarrow \mu^+$  decay is contained in the stopping counter. The positron from the  $\mu^+ \rightarrow e^+$  decay should also be found in the counters around the stopping counter (Layers 13 and 14 in this case).

TDC information of the stopping counter as well as the neighboring counters by requiring that the times of the hits from the  $e^+$  track are consistent with each other.

Range Stack Straw Chambers (RSSCs) are located after layers 10 and 14 of the RS. The inner RSSC consists of two layers of 24 straws per sector, and the outer RSSC consists of two layers of 28 straws per sector. The RSSCs are used to determine the trajectory (and therefore refine the range) of a charged particle in the RS. Information on the RSSCs is given in [30].

Energy, range and momentum measurements of charged tracks are crucial to distinguish the  $\pi^+$ 's in the signal region from backgrounds due to  $K_{\pi 2}$  decays, which have monochromatic momenta of 205 MeV/c. Energy, range and momentum resolutions of 2.8%, 2.9% and 1.1% respectively are achieved for fully contained  $K_{\pi 2}$  decays.

### 3.3.5 Photon Veto

The detection of any activity coincident with the charged track is crucial for suppressing the backgrounds for  $K^+ \rightarrow \pi^+ \nu \bar{\nu}$ . Photons from  $K_{\pi 2}$  and other radiative decays are detected by a hermetic set of photon detectors, which are shown in Fig. 3.14.

The photon detectors, surrounding the  $K^+$  decay vertex in a  $4\pi$  solid angle, are located in the barrel, upstream and downstream end caps, and near the beam line. Photon veto is performed by the Barrel Veto (BV), the Barrel Veto Liner (BVL), the upstream and downstream End Caps (ECs), the upstream and downstream Collar detectors (CO), the downstream Microcollar detector

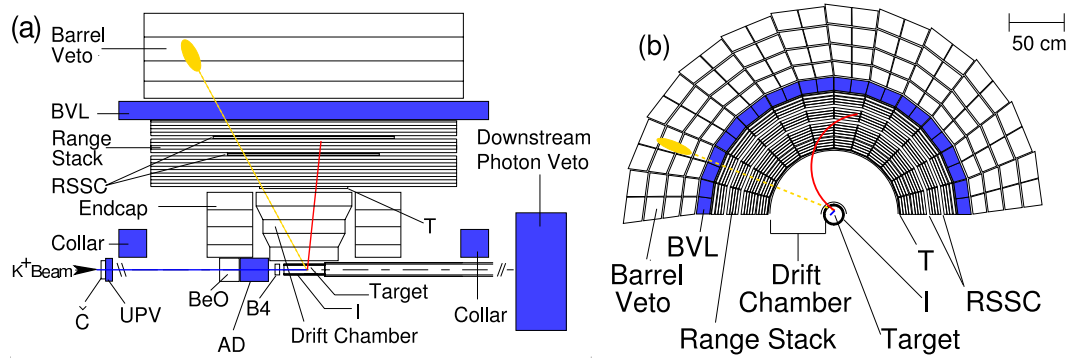


Figure 3.14: Schematic side (left) and end (right) views of the upper half of the E949 detector. Newly installed or upgraded photon detectors for E949 are in blue.

(CM), as well as the AD, target, IC, VC and RS.

The BV, 1.9-m long, is located in the outermost barrel region with an inner radius of 94.5 cm and an outer radius of 145.3 cm. It surrounds two thirds of the  $4\pi$  sr solid angle. The BV consists of 48 azimuthal sectors and four radial segments. The radial modules consist of 16, 18, 20 and 21 layers of 1-mm thick lead and 5-mm thick plastic scintillator from inner to outer module respectively. The azimuthal boundaries of each sector are tilted so that photons from the decay vertex could not travel along the inactive inter-sector gaps without losing their energy in the active regions.

The BV has 14.3 radiation lengths in total. Each end of each module is read out by a PMT and the signals are recorded by an ADC and a TDC. The time resolution of individual BV counters is measured to be 1.0 ns. The resolution is limited by the sampling time of the TDCs. The fraction of the photon energy left in scintillators is about 30%.

The BVL, which is newly installed for E949, is located just outside the Range Stack and inside the Barrel Veto. It has an inner radius of 85.2 cm and an outer radius of 93.5 cm, and consists of 48 azimuthal sectors and 12 radial layers of 1 mm thick lead and 5 mm thick plastic scintillator.

The BVL has 2.3 radiation lengths in total. Its length (2.2 m) is larger than that of the BV, so that the BVL adds active material to a region of the detector where the radiation length is relatively small. Each end of each module is read out by a PMT and the signals are recorded by an ADC and a TDC. Groups of 8 adjacent sectors in each end are read by TDs. The time resolution of the individual BVL counters is measured to be 0.5 ns. The resolution of the BVL modules is also limited by the TDC sampling time. The fraction of the photon energy seen by scintillator is about 30%.

The EC photon detector [31] is located in the 1 Tesla magnetic field and covers roughly one-third of the  $4\pi$  sr photon coverage. The EC is exposed in a high counting-rate environment near the beam line, where beam particles cause many hits that are not coincident with kaon decays. These hits may mask photons from  $K_{\pi 2}$  decays in the case that an accidental hit arises earlier than the photon hit, or cause vetoing on accidentals and loss of acceptance. Therefore offline double-pulse finding in the signals recorded by the CCDs, and vetoing on these second pulses separately, is crucial.

The upstream EC detector consists of 75 undoped Cesium Iodide (CsI) crystals, segmented in four rings (13, 14, 21 and 27 crystals from the inner to outer ring respectively), and the downstream EC detector consists of 68 crystals in four rings (11, 13, 19 and 25 from the inner to outer ring respectively). A total of 143 crystals with a pentagonal cross-section are used (Fig. 3.15).

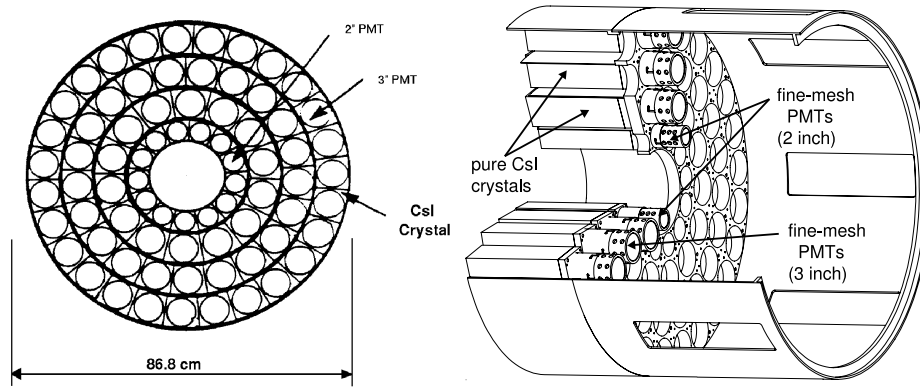


Figure 3.15: End view (left) and back view (right) of the upstream End Cap.

Each crystal has a length of 25 cm (13.5 radiation lengths) and the whole EC detector is designed to minimize photon escape through its radial cracks. Fine-mesh PMTs [32], which maintain high gains in strong magnetic fields, are attached directly to the crystals to achieve efficient light collection (Fig. 3.15). Only the fast component of the CsI light output with a decay time of a few tens of a nanosecond at a wavelength of 305 nm is enhanced by ultraviolet transmitting optical filters attached to the PMT window. The PMT signals are read out by ADCs, TDCs, and CCDs.

The upstream and downstream CO detectors are located outside the ECs and around the beamline, so that they cover the region with small angles around the beam line. They are similar in construction and cross-sectional size, but the upstream CO is about half the thickness of the downstream one. Their xy cross-section is a  $\sim 50$  cm by  $\sim 50$  cm dodecagon with a 203.2 mm (164.3 mm for the downstream CO) hole in the middle, and they are segmented in 12 azimuthal sectors. The downstream CO consists of 25 layers of 5 mm thick scintillator alternating with 2 mm thick lead, with a total thickness of about

173.5 mm and about 9 radiation lengths. The light from each sector is read out by bundles of WLS fibers glued in grooves in the scintillator, then fed to a PMT outside the magnetic field through a lucite lightguide. The upstream CO is read out directly with the lightguide, and has no fibers. The signals are recorded by TDCs and ADCs.

### 3.4 Trigger

The trigger selects signal-like events out of all kaon decays to be recorded, based on logic pulses, ADC and TD information from the detector elements. Digitized information of the selected events, which correspond to 70-80 Kbyte of data per event, is transferred from the electronics hut to the main computer for data taking.

The trigger is composed of a fast level-0 trigger and level-1.1 and -1.2 triggers. The level-0 trigger makes decisions entirely with logic pulses from detectors. It has a rejection of  $10^3$  and introduces 38 ns of dead time for every coincident hit in the first two layers of the Range Stack (T●2). The level-1.1 and -1.2 triggers involve partial processing of ADC and TD data, and operate on the lower rate events that pass the level-0 trigger. The level-1.1 trigger has a rejection of 12 after level-0, and introduces 10 to 20  $\mu$ s of dead time per level-0 trigger. The level-1.2 trigger has a rejection of 2 after level-1.1 and introduces a dead time of up to 100  $\mu$ s per level-1.1 trigger. The entire trigger for  $\pi\nu\bar{\nu}$  therefore has a rejection of 24000, and reduces the  $2.6 \times 10^6$  kaon decays (during the time the detector is live) to about 100 events per spill.

Two triggers are used for the  $\pi\nu\bar{\nu}$  analysis,  $\pi\nu\bar{\nu}(1)$  and  $\pi\nu\bar{\nu}(2)$  for the two

kinematic regions. For the  $\pi\nu\bar{\nu}(2)$  study, the  $OR$  of these two triggers will be used. They consist of the following requirements:

$$\begin{aligned}
\pi\nu\bar{\nu}(1) &\equiv \text{KB} \cdot \text{DC} \cdot \text{IC} \cdot \text{T} \bullet 2 \cdot (6_{ct} + 7_{ct}) \cdot \overline{19_{ct}} \cdot \overline{\text{BV} + \text{BVL} + \text{EC}} \cdot \\
&\quad (\text{L0\_rr1}(1) \cdot \text{US} + \text{L0\_rr1}(2) \cdot \text{DS}) \cdot \overline{\text{L0\_zfrf}} \cdot \text{HEX} \cdot \text{L1.n} \\
\pi\nu\bar{\nu}(2) &\equiv \text{KB} \cdot \text{DC} \cdot \text{IC} \cdot \text{T} \bullet 2 \cdot 3_{ct} \cdot 4_{ct} \cdot 5_{ct} \cdot 6_{ct} \cdot \overline{(13_{ct} + \dots + 18_{ct})} \cdot \overline{19} \cdot \\
&\quad \overline{\text{BV} + \text{BVL} + \text{EC}} \cdot \text{L0\_rr2}(1) \cdot \text{HEX} \cdot \text{L1.n} \cdot (\text{ps16} + \overline{C_\pi}) \quad (3.1)
\end{aligned}$$

where

- $K^+$  Stop Requirements:
  - KB : KB requires a coincident hit in the Kaon Čerenkov Counter, the B4 Hodoscope, and an analog sum of the energy of the hit fibers the target of at least 20 MeV. This requirement ensures that a kaon enters the target.
  - DC : Online delayed coincidence, in which the IC time is required to be at least 2 ns later than the time in the Kaon Čerenkov Counter. This delayed coincidence requirement ensures that a kaon decays at rest.
- Fiducial Requirements on Charged Tracks:
  - IC : At least one hit in the I-Counter is required to be coincident with the T•2 time. This condition requires that a charged track from a kaon decay enters the fiducial region of the detector.



- $\text{T}\bullet 2$  : A coincidence hit is required in the first two layers (T-Counter and layer 2) of the Range Stack in the same sector. This condition requires that a charged track from a kaon decay enters the Range Stack.
- $\overline{\text{L0\_zfrf}}$  : For  $\pi\nu\overline{\nu}(1)$ , extra fiducial requirements are imposed. A charged track is required to stop in the active region of the Range Stack scintillators, and not in the second RSSC. In such a case,  $\mu^+$ s from  $K_{\mu 2}$  decays can fake  $\pi^+$ s that come to rest in the Range Stack layer 14. Such a constraint is not needed for  $\pi\nu\overline{\nu}(2)$ , because  $\pi\nu\overline{\nu}(2)$  pions are not allowed to reach layer 13.
- Range Requirements on Charged Tracks:
  - $(6_{ct} + 7_{ct})$  or  $3_{ct} \cdot 4_{ct} \cdot 5_{ct} \cdot 6_{ct}$  : For  $\pi\nu\overline{\nu}(1)$ , a charged track must reach the Range Stack layer 6 or 7. For  $\pi\nu\overline{\nu}(2)$ , it must reach layer 6 and have hits in all previous layers. The  $\text{T}\bullet 2$  sector and two sectors clockwise from it are defined as the charged track ( $ct$ ) sectors. This condition removes short-range tracks from 3- and 4-body decays.
  - $\overline{(13_{ct} + \dots + 18_{ct})} \cdot \overline{19}$  : For  $\pi\nu\overline{\nu}(2)$ , a charged track is not allowed to reach Range Stack layers 13-19, whereas for  $\pi\nu\overline{\nu}(1)$  this requirement is loosened to only layer 19 veto. This condition removes  $\mu^+$  and other long tracks, and, for the case of  $\pi\nu\overline{\nu}(2)$ , it allows to collect more events in the kinematic region of interest.
  - $\text{L0\_rr2(i)}$  : Refined range requirement on a charged track.  $\mu^+$ 's from  $K_{\mu 2}$  decays are suppressed by the  $\overline{(19_{ct})}$  requirement. However, some of the  $\mu^+$ 's can still survive the requirement if their polar

angle with respect to to beam direction is small and they stop near the edge of the RS scintillators. Events are rejected if the range calculated in the online trigger is too long. For  $\pi\nu\overline{\nu}(1)$  and  $\pi\nu\overline{\nu}(2)$  different “masks” are used, given their different range. The online range in the target is obtained from the number of hit fibers, and the online range in the Range Stack is obtained from the stopping layer of the charged track and corrected for the polar angle. The polar angle is measured by the z positions at RS layers 11, 12 and 13, which are obtained from the end-to-end time difference of both-end hits. The online stopping counter is found by the ”stopping counter finder” (SCF), which defines the outermost and most clockwise  $ct$  counter as the stopping counter.

- Online Photon Veto:
  - $\overline{BV + BVL + EC}$  : Online photon veto in the BV, BVL and EC. Any photon hit which is coincident with T●2 and whose energy is above a threshold is not allowed. Each PMT signal from each end of the BV and BVL counters is discriminated by the threshold corresponding to 5 MeV, and the mean time of the discriminated signals from both ends is given by digital mean-timers [25]. Events are rejected if the output signals of the mean timers are coincident with T●2. Each PMT signal from each End Cap crystal is discriminated by the threshold corresponding to 20 MeV. Events are rejected if the output signals are coincident with T●2.
  - HEX : Only one RS hextant is allowed to have hits coincident with

T•2, or two hexants if they are adjacent. This rejects events with multiple tracks and events with photon activity in the RS.

- Level-1.1 and 1.2:
  - L1.1 : Level-1.1 trigger requires a signature of  $\pi^+ \rightarrow \mu^+$  decay in the online stopping counter. The height (PH) and the area (PA) of the pulse(s) recorded by the TDs in the stopping counter are compared. The decision is made by a control board with Application Specific Integrated Circuits (ASICs) in each TD board. The ratio PH/PA would be smaller for double pulses than for a single pulse. Events are rejected if the PH/PA ratio is large.
  - L1.2 : Level-1.2 trigger consists of three parts: (1) Events are rejected if coincident hits are detected in a RS counter near the stopping counter. It rejects events with muons that pass Level-1.1 due to accidental hits from the outside providing the double-pulse  $\pi^+ \rightarrow \mu^+$  decay signature in the stopping counter. (2) Events are rejected if one of two adjacent hexant hits is not due to a charged track (“hexant afterburner”). This requirement removes those events that pass the HEX requirement because of accidental hits. (3) Events are rejected if the SCF assignments are not meaningful (e.g., stopping layer is more than 19).
- Pion Čerenkov veto
  - (ps16+ $\overline{C_\pi}$ ) : An online pion Čerenkov veto was imposed in the middle of the run, when the beam separator broke down and the

rate of beam pions was found to be too high. This requirement was prescaled by 16 (i.e. it was not applied in one every 16 events), in order to be able to measure its rejection and assess its effect. The data taken before the addition amount to about 39.4% of the total.

In addition to the  $\pi\nu\bar{\nu}$  trigger, various "monitor" triggers also collected events for use in data quality assessments, calibration of detector subsystems, and acceptance and background calculations.

- $K_{\pi 2}(1) = KB \cdot T \bullet 2 \cdot (6_{ct} + 7_{ct}) \cdot \overline{(19_{ct})}$
- $K_{\pi 2}(2) = KB \cdot DC \cdot T \bullet 2 \cdot IC \cdot (6_{ct} + 7_{ct}) \cdot \overline{(19_{ct})} \cdot HEX \cdot L1.n$
- $K_{\mu 2}(1) = KB \cdot T \bullet 2 \cdot (6_{ct} + 7_{ct}) \cdot (17_{ct} + 18_{ct} + 19_{ct})$
- $\pi_{scatter} = \pi B \cdot \overline{DC} \cdot T \bullet 2 \cdot IC \cdot (6_{ct} + 7_{ct}) \cdot \overline{BV + BVL + EC} \cdot HEX,$

where  $\pi B$  requires that a pion enters the target. Because each monitor trigger is highly prescaled, the number of all the monitor triggers in each spill were at most 10.

### 3.5 Monte Carlo Simulation (UMC)

The detector and the physics processes in it are modeled by a Monte Carlo (MC) simulation program. The MC includes all of the detector elements, except for the beam instrumentation upstream of the target, therefore the simulation of kaon decays in the E949 detector starts from a "beam file" with the (x,y,z) positions of kaon decays in the target obtained from an analysis of

$K^+ \rightarrow \mu^+ \nu$  decays. The MC generates all data, except for the TD and CCD pulse-shape information.

Multiple Coulomb scattering of charged particles with various nuclei in the detector are calculated according to the theory of Moliere [33], with corrections for the spin of the scattered particle and the form factor of the nucleus [34]. Hadronic interactions of positively charged pions in the plastic scintillators are calculated using a combination of data and phenomenological models [35]. Photon and electron interactions are calculated using the EGS4 electromagnetic-shower simulation package [36].

The accuracy and the performance of the MC has been verified by comparing the different kinematic variables from data and MC for  $K^+ \rightarrow \pi^+ \pi^0$  and  $K^+ \rightarrow \mu^+ \nu$  decays.

## 3.6 Summary of 2002 Data Taking

The E949 experiment had the first physics run for 12 weeks from March to June in 2002. The data collected in the run period corresponded to  $KB_{live} = 1.77 \times 10^{12}$  kaon decays in the target. This number is found by scalers that count the number of KB triggers for every spill, and then is corrected for the amount of data discarded because the detector had some technical flaw during that time (“bad runs”). Fig. 3.16 shows the number of accumulated kaon decays as a function of the data-taking days for the various running years of E787 and E949.

The E949 run was performed under a high beam intensity environment. The proton intensity of the AGS increased to twice as high as in E787. The to-

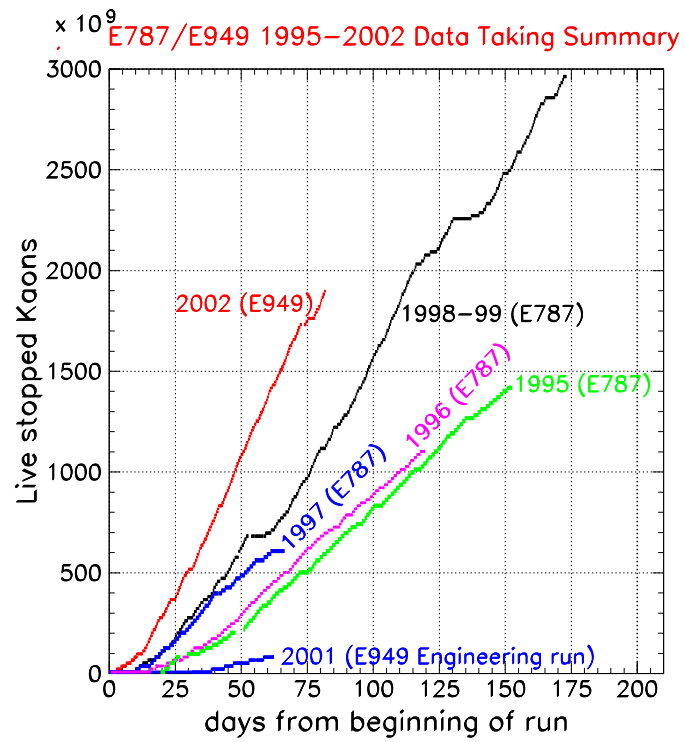


Figure 3.16: Number of kaon decays in the target as a function of the data-taking days for E787 and E949.

tal exposure of kaons available for E949 was 30% that of E787, which recorded  $5.94 \times 10^{12}$  kaon decays in the target.

# Chapter 4

## Analysis overview

Reliable detection of a process as rare as  $K^+ \rightarrow \pi^+ \nu \bar{\nu}$  requires knowledge and suppression of the background processes of the order of  $10^{-12}$ , depending on the achieved acceptance. For this purpose, a set of stringent selection criteria (“cuts”, see Appendix A) is used in a blind analysis, in order to estimate the expected background levels from data. Monte Carlo simulation is also used for the backgrounds that cannot be reliably identified in the data samples. In this chapter, the analysis technique and the methods used to verify its reliability will be described.

### 4.1 Event Reconstruction

The event reconstruction consists of reconstruction of a charged track in the target, UTC and Range Stack, of the kaon path and the decay vertex in the target, of beam particle hits in the beam instrumentation, and of photon hits in the photon detectors. The event reconstruction in the x-y view is shown in



Fig. 4.1.

Charged-track reconstruction is performed twice for the target, UTC and RS. The first step is to identify the Range Stack counters that have hits due to the track (“track counters”). First, a sector that has coincident TDC hits in the first two layers of the RS counters around the online  $T_{\bullet 2}$  timing is determined to be the offline  $T_{\bullet 2}$  sector. If the sector is not found, the online  $T_{\bullet 2}$  sector is used. The track counters are defined as the counters that have TDC hits coincident with the  $T_{\bullet 2}$  timing. The average time of the track counters is defined as the track time,  $trs$ . The outermost and most clockwise track counter is defined as the offline “stopping counter”.

The UTC track is reconstructed by two separate fits: one in the x-y plane (perpendicular to the beam axis) and one in the r-z plane (formed by the radial and beam axes). In the x-y plane, a circle is fitted to the hit positions derived from the wire locations and drift distances. In the r-z plane, a straight line is fitted to the cathode strip hits. The polar angle of the charged track is evaluated from this r-z fitting.

In the first step of the target reconstruction, the times, energies and positions of the target fibers having CCD hits are examined, and they are categorized into “kaon”, “pion”, “opposite-side pion” and “gamma” fibers. The “kaon” fibers are determined as the ones that have energies larger than 4 MeV, times coincident with that of the B4 Hodoscope, and positions located outside a band (“swath”) around the extrapolated UTC track. The average time of the kaon fibers is defined as the target kaon time,  $tk$ , and their energy sum represents the target kaon energy. The kaon decay vertex is determined by the kaon fiber that is closest to the extrapolated UTC track and farthest from the

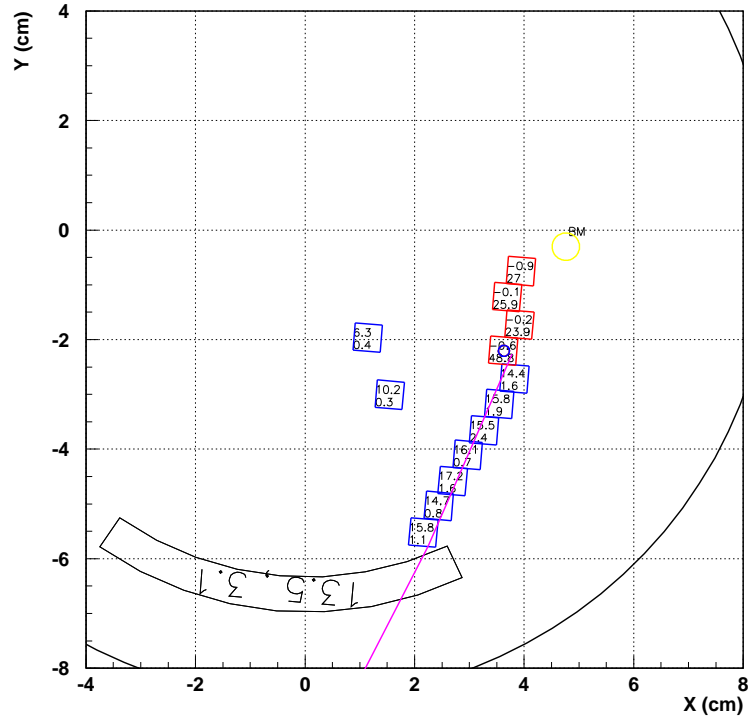
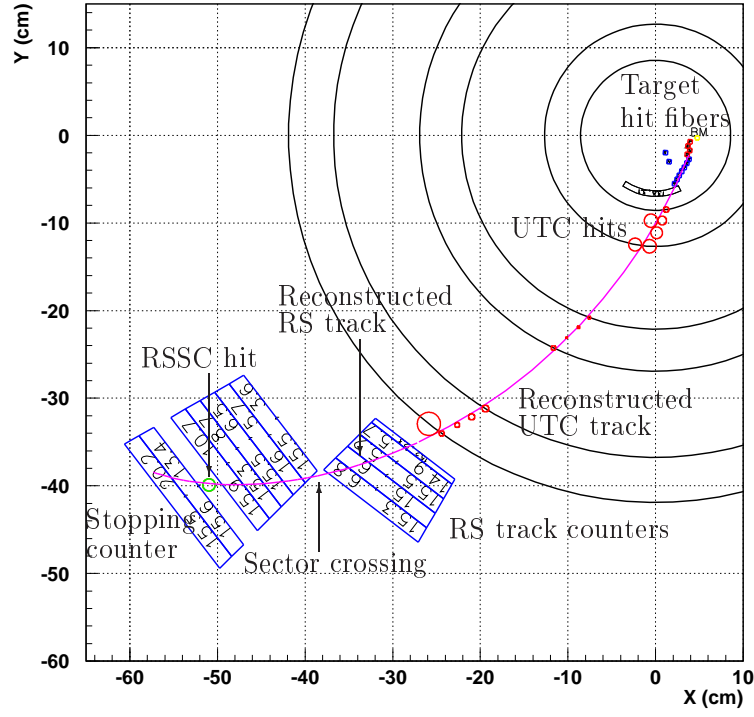


Figure 4.1: Reconstruction of an event in the x-y view: the reconstruction in the target, UTC and Range Stack (top), and the reconstruction in the target (bottom).

x-y position of the B4 Hodoscope hit. The z position of the kaon decay vertex is obtained by extrapolating the UTC track to the decay vertex fiber. The "pion" and "opposite-side pion" fibers are selected by taking the fibers which have energies typically less than 1 MeV, times coincident with the track time, and positions inside the swath. The fibers on the side of the UTC track relative to the decay vertex are assigned to "pion" fibers, and the ones on the other side are assigned to "opposite-side pion" fibers. The opposite-side pion fibers could potentially be indicating additional charged particles. The average time of hits in the pion fibers is defined as the target pion time,  $t_{pi}$ . The fibers that have times consistent with the track time and are not categorized as the kaon, pion or opposite-side pion fibers, are assigned to "gamma" fibers. Hits in the gamma fibers potentially originate from photons or secondary beam particles.

In the RS stopping counter, the  $\pi^+ \rightarrow \mu^+$  decay signature is searched for via a pulse-fitting method. When a  $\pi^+$  comes to rest in the RS, the stopping counter has the signature of double pulses due to the  $\pi^+$  and the secondary  $\mu^+$ . A  $\chi^2$  fit is performed on the TD output twice, with a single-pulse assumption and a double-pulse assumption, and sometimes three times, with a triple-pulse assumption, by varying the leading edges, heights and pedestals of template pulses that have been prepared for the individual counters and calibrated with  $\pi_{scatter}$  monitor trigger data. A triple-pulse fitting is performed when more than two pulses are found, or the fitted second pulse does not look to be due to a  $\mu^+$  but an accidental, based on the double-pulse fit output. In this case, one of the three pulses is assigned to an accidental. The algorithm returns the fit qualities for both the single- and double-pulse assumptions (and triple-pulse assumption if the fit is performed) and the time and energy information

of the pulses obtained by the fit. The TD pulse shapes in the examples of the double-pulse and triple-pulse fits are shown in Fig. 4.2 and 4.3. More details can be found in [38].

After the pulse fitting is made, a second iteration of the track reconstruction is performed. The momentum in the UTC is calculated from the radius of the circle in the x-y fit and the polar angle in the r-z fit. The total momentum of the charged track  $ptot$  is obtained by correcting the momentum in the UTC by the target range, the I-Counter range and the amount of dead material in the inner wall of the UTC and the drift gas. After the UTC track determination is finished, a second iteration of the target reconstruction is made. In this iteration, a double-pulse fit is performed on the CCD pulses of the kaon decay vertex fiber, in order to identify the  $K^+ \rightarrow \pi^+$  decay pattern. The energy loss of the pion in the kaon decay vertex fiber, obtained from the second pulse found by the fit, is subtracted from the target kaon energy and is added to the target pion energy. Two examples of such a fit are shown in Fig. 4.4 and Fig. 4.4. In the second example, the energy of the second pulse is higher than expected from just a decay pion heading directly towards the detector acceptance. This case is discussed in the next section.

The energy deposit of the charged track in the Range Stack is calculated next. The energy deposit in each track counter is primarily obtained from the ADC energy, which is the area of a pulse within an ADC gate of 100 ns. If an accidental hit deposits energy in one of the track counters within the ADC gate, the track energy could be overestimated, which would result in loss of signal acceptance. To avoid this, the energy obtained from the TD pulse height information is used instead of the ADC energy, if the ADC energy is

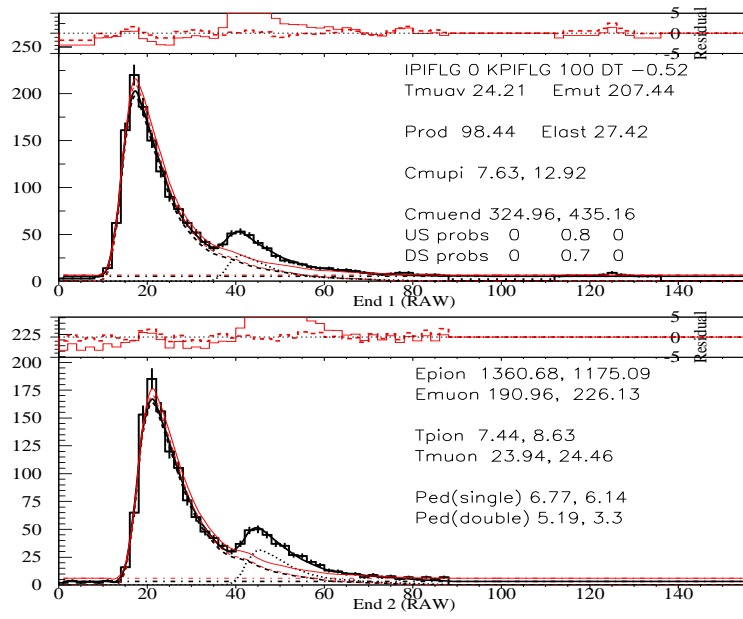


Figure 4.2: Double-pulse fit to the TD pulse shape in the stopping counter for the upstream (top) and downstream (bottom) end.

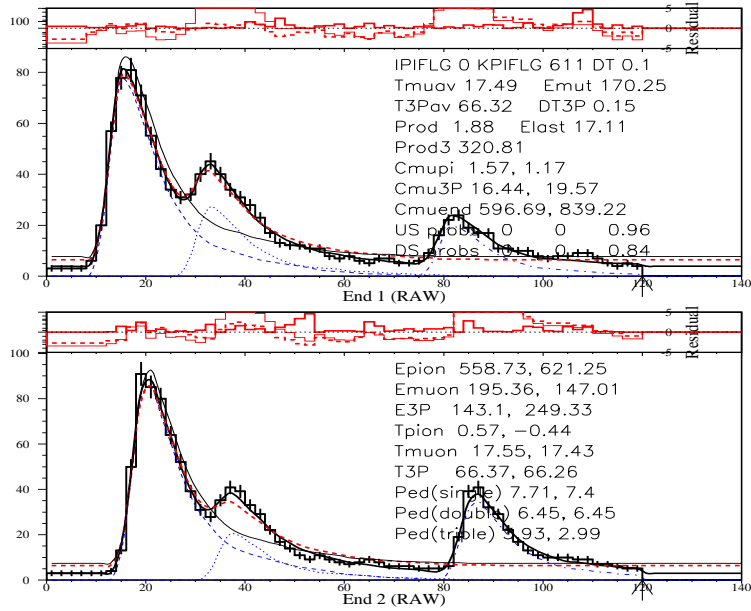


Figure 4.3: Triple-pulse fit to the TD pulse shape in the stopping counter for the upstream (top) and downstream (bottom) end.

2006/04/14 13.19

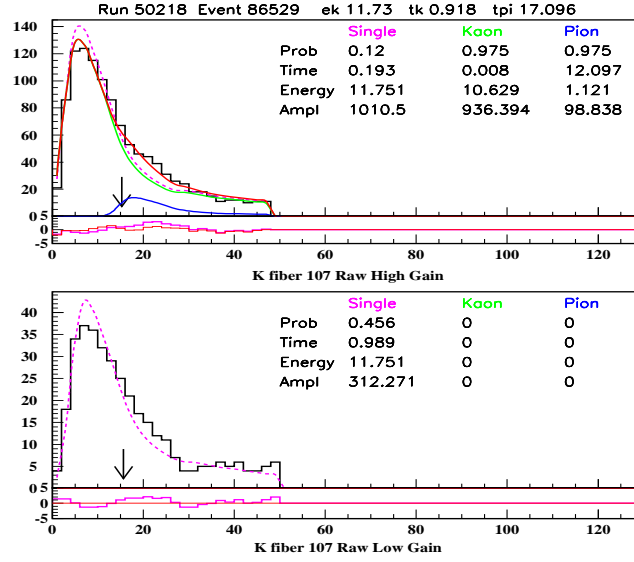


Figure 4.4: Double-pulse fit to the CCD pulse shape in the Kaon decay vertex fiber for the high (top) and low (bottom) gain readout. The energy of the second pulse is a typical one for the energy deposit of a decay pion heading directly towards the detector acceptance.

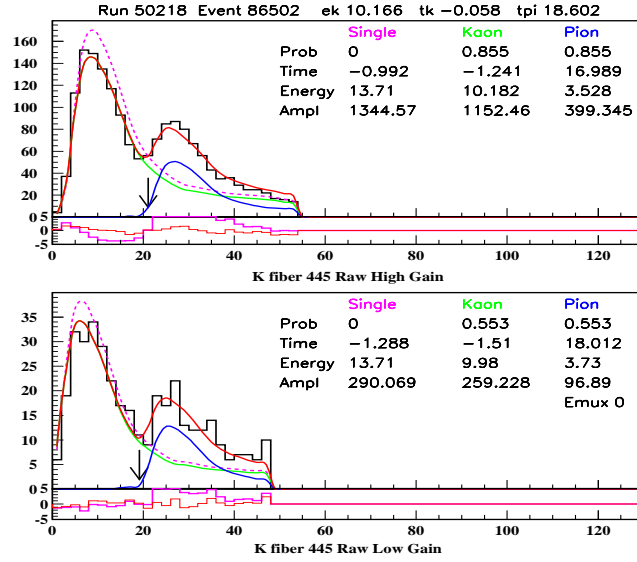


Figure 4.5: Double-pulse fit to the CCD pulse shape in the Kaon decay vertex fiber for the high (top) and low (bottom) gain readout. The energy of the second pulse is significantly higher than the typical energy deposit of a decay pion heading directly towards the detector acceptance, and may signify a scatter (see section 4.2).

much greater than the the one expected from the TD pulse height, because the pulse height of the track hit is less disturbed by the existence of an accidental pulse. The total energy deposit of the track in the RS is obtained by summing up the energies in the track counters, and subtracting the muon energy in the stopping counter measured by the TD pulse fitting. This visible energy in each track counter is corrected to the true energy deposit by Birk's formula [37],

$$\frac{dL}{dx} = \frac{dE/dx}{1 + k_B \cdot dE/dx}, \quad (4.1)$$

where  $L$  is the luminescence in a plastic scintillator and  $k_B = 0.01$  is called Birk's constant.

The range of the charged track in the RS is derived from a fitted track, calculated separately in the x-y and r-z planes. A fit is performed only in the x-y plane, by propagating a track in the RS that loses kinetic energy with the Bethe-Bloch formula with the pion assumption, and is being bent in a 1 Tesla magnetic field. The incident momentum and angle (in the x-y plane) at the entrance of the RS are the fit parameters, and the track is required to match the measured positions of the sector crossings and RSSC hits and the measured energy in the stopping counter. In the r-z plane, the path of the track is obtained by extrapolating the UTC track to the stopping position of the track. The  $\chi^2$ s for the r-z track are calculated from the residuals between the extrapolated UTC track and the z measurements based on the RSSCs and the end-to-end time differences in the individual counters. The range in the RS is calculated from the path length of the fitted track, and is then corrected to the total range  $rtot$  by adding the target range, the range in the I-Counter, and



the ranges in the dead materials using the extrapolated UTC track. Finally the total energy  $etot$  is calculated by adding the RS, target and IC energy, and compensating for energy loss in the UTC material.

In the Kaon and Pion Čerenkov Counters, coincident TDC or CCD hits are clustered from 14 PMTs in each. The average time and the multiplicity of those hits are calculated for each cluster. In the two sets of Beam Wire Chambers, beam particle hits are reconstructed when two or three planes have coincident TDC hits. The TDC values of the wire hits are averaged to obtain the time of the incoming particle. In the B4 Hodoscope, two perpendicular counters in different layers are clustered when they have coincident TDC or CCD hits. The time and x-y position of the cluster are obtained from the energy-weighted average of the TDC or CCD hits. The measured energy deposits are used to separate kaons and pions, which leave different energies in the B4 Hodoscope. The times of hits in any of the above beam detectors are used to remove Double Beam events (see section 4.2) by checking extra activities at trs.

In the photon detectors, the time and energy of each module in the detector subsystems are calculated. The hits that are coincident with the track time are searched for to veto the backgrounds that include photons.

## 4.2 Background overview

The range in plastic scintillator ( $rtot$ ) versus momentum ( $ptot$ ) distribution of the outgoing charged particle (pion or muon) is shown in Fig. 4.6 for the events which passed the  $\pi\nu\bar{\nu}(1)$  or (2) trigger. The two concentrated peaks are due to the dominant two-body decays  $K^+ \rightarrow \pi^+\pi^0$  ( $K_{\pi 2}$  peak) and  $K^+ \rightarrow \mu^+\nu$

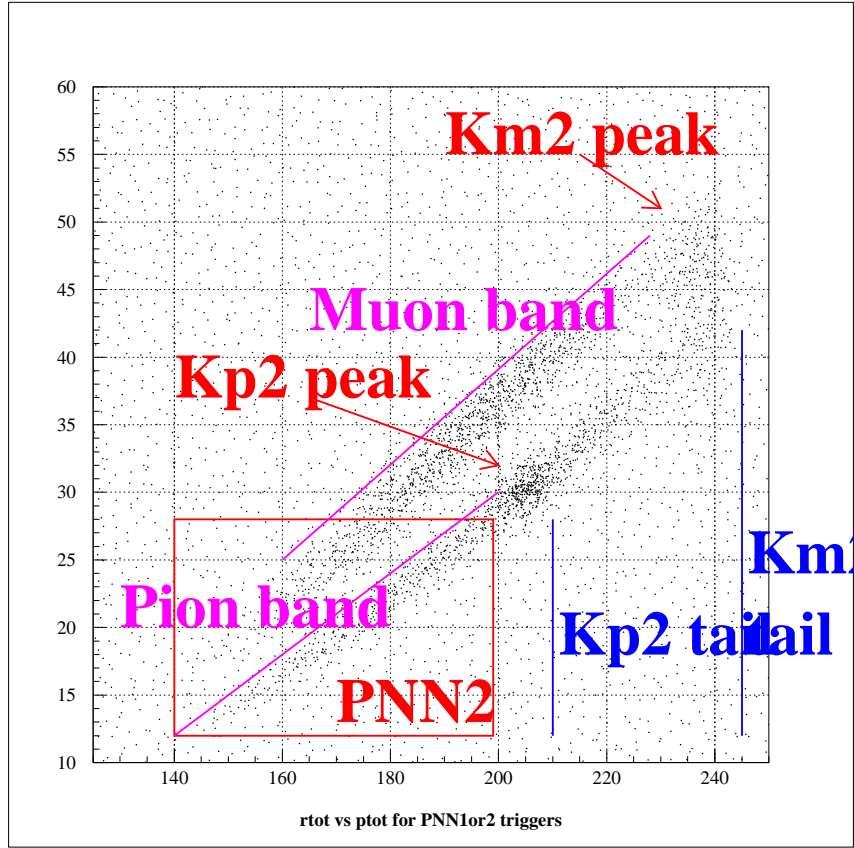


Figure 4.6: The range in plastic scintillator ( $rtot$ ) versus momentum ( $ptot$ ) distribution of the outgoing charged particle (pion or muon) for the events which passed the  $\pi\nu\bar{\nu}(1)$  or  $(2)$  trigger.

( $K_{\mu 2}$  peak). The range tails contain peak events with inelastic pion or muon scattering in the RS. Therefore the momentum measurement is correct, but the range is mismeasured and these events do not belong to the peak. The diagonal “bands” are either multi-body decays with pions or muons ( $K_{\pi 2\gamma}$ ,  $K_{\mu 3}$ ,  $K_{\mu 2\gamma}$ ,  $K_{e4}$ ), decays in flight, or, in the case of pions,  $K_{\pi 2}$ ’s where the pion scattered inelastically in the target. In this case, both the range and the momentum are measured incorrectly. Beam pions that scatter into the detector acceptance also belong to this band.

As can be seen in this plot, the  $K_{\mu 2}$  peak and tail do not contribute at all to the PNN2 background, and the three-body muon decays in the band give a small contribution. For these modes to be confused with signal, both the muon has to be misidentified as a pion, and the extra photons have to escape the veto.

The multi-body pion decays and scattered beam particles are the processes whose kinematics coincide with those of  $K^+ \rightarrow \pi^+ \nu \bar{\nu}$  in the PNN2 region.  $K_{\pi 2 \gamma}$  has 3 photons to veto on, and  $K_{e4}$  has the signature of extra activity in the target, either in the Kaon fibers (detected as second pulses) or outside of them.

Scattered beam backgrounds are divided in 2 categories: *single-beam background* (see Fig. 4.7) is due to a beam pion entering the target and scattering into the detector or a beam Kaon decaying in flight causing its products to be in the PNN2 kinematic region due to a Lorentz boost. Although the case of a Kaon decay-in-flight is suppressed by all the other K decay cuts as well, a beam pion scattering into the detector has no extra particles to veto on, just like the signal. However, both processes occur instantaneously after the entrance of the beam particle into the target, unlike decays at rest, where the Kaon has to stop first and decay a while later, therefore they do not satisfy the delayed coincidence requirement. The *double-beam background* (see Fig. 4.8) is caused by two beam particles entering the detector at times sufficiently different to satisfy the delayed coincidence. The products of the first Kaon can be missed under certain circumstances, and a second pion can scatter into the detector as in the single-beam-pion case (“K-pi” background) or a second Kaon can enter the target and decay in flight, as in the single-beam-kaon case

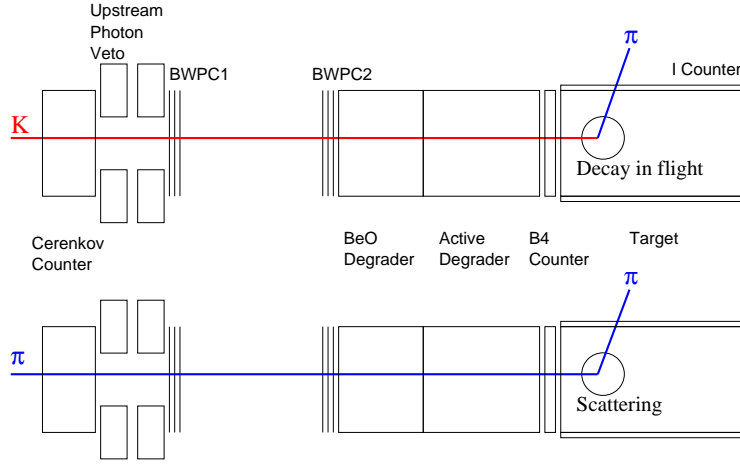


Figure 4.7: Schematic diagrams of the Single Beam background: a Single Kaon Beam background (top) and a Single Pion Beam background (bottom).

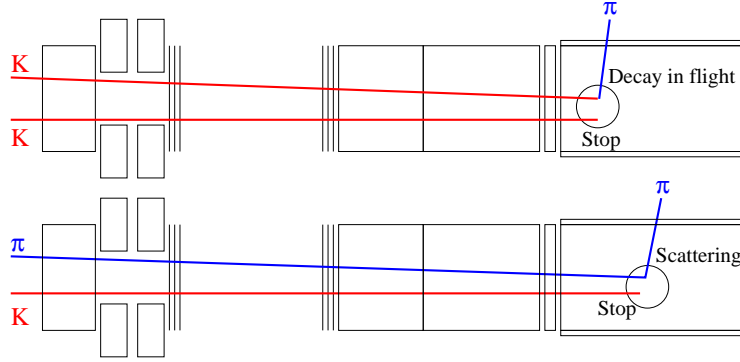


Figure 4.8: Schematic diagrams of the Double Beam background: a  $K - K$  Double Beam background (top) and a  $K - \pi$  Double Beam background (bottom).

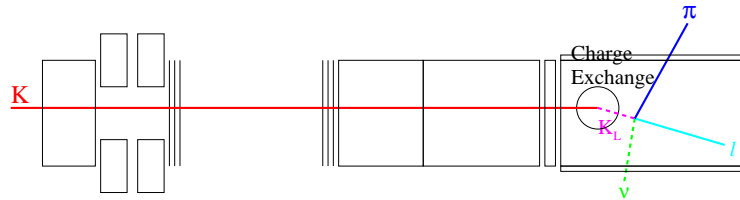


Figure 4.9: Schematic diagram of the charge exchange interaction background.

(“K-K” background). Double-beam backgrounds are suppressed by requiring no activity in the beam detectors in time with the Kaon decay.

Beam kaons can also interact in matter as they are being brought to rest and produce a neutral kaon via the charge exchange process (see Fig. 4.9).  $K^0$ 's are not slowed down in the target, so potential background arising from prompt  $K_s^0$ 's decay is removed by the delayed coincidence requirement. However,  $K_L^0$ 's are long-lived and can decay semi-leptonically. If the  $K_L^0$  travels slowly in the target, therefore its decay point is not well separated with the entering  $K^+$  cluster, then the decay  $\pi^+$  can emulate the signal, if the lepton also happens to not be detected.

The main background in the PNN2 region, however, is the  $K_{\pi 2}$  decay where the  $\pi^+$  scatters in the target, and the main concern in this analysis will be to minimize it. This is a particularly dangerous background due to the large BR of  $K_{\pi 2}$  and the way the geometry of the scatter correlates the kinematics of the  $\pi^+$  and the direction of the photons produced by the  $\pi^0$ . Fig. 4.10 gives an idea of this mechanism: the outgoing  $\pi^+$  starts at the direction of the incoming K, and its track is hidden under the Kaon fibers. Due to the two-body kinematics, at least one of the two photons has a higher probability to go towards the beam direction, where the photon detection power of the detector is smaller than that at the barrel region. Then the  $\pi^+$  scatters inelastically in a kaon fiber and enters the detector with deteriorated kinematic quantities as compared to the  $K_{\pi 2}$  peak. Such events are wrongly included in the PNN2 box, and their photon veto rejection is not the same as the  $K_{\pi 2}$  decays on the peak.

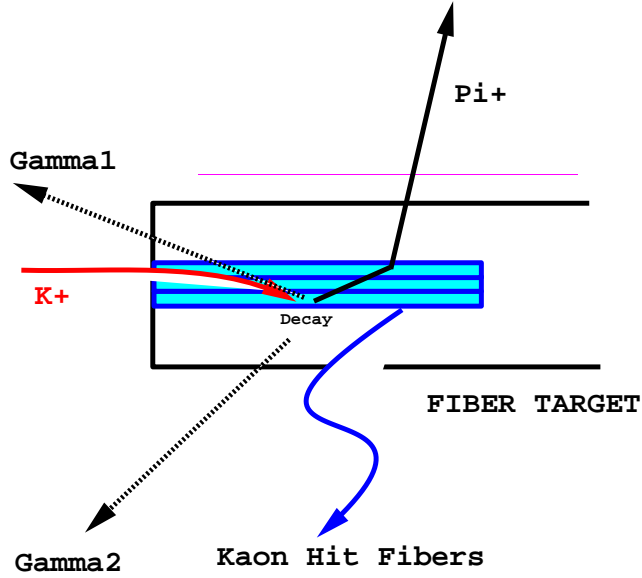


Figure 4.10: A schematic of a  $K_{\pi 2}$  scattering event in the target in which the pion travels along the fibers, and thereby the neutral pion escapes through the weak photon detection region of the detector.

## 4.3 Analysis technique

### 4.3.1 Background estimation from data

The large suppression of backgrounds needed for a reliable measurement makes estimation of the background in the signal region difficult, because any measurement involving low statistics is subject to large statistical fluctuations. Furthermore, the development of cuts using smaller and smaller numbers of events can result in bias, because it is always possible to design cuts to remove a single event or a small number of events, but which may not represent the characteristics of a larger data sample.

To avoid this bias in designing cuts, a “blind” analysis is performed. The background sources are identified a priori and the signal region is pre-defined

(a multi-dimensional parameter space, populated by the events that pass all the cuts, often referred to as the “box”) where the signal to background ratio is expected to be the highest. Cuts to suppress background are developed using events which lie outside the box and events in the box are not counted or examined until the cuts and the background estimates are final.

To enhance the statistical power of the analysis, background measurements are made via “bifurcated” analysis. Each background is addressed by at least two uncorrelated cuts or group of cuts, which can be independently “inverted” to create high statistics background samples from data. That is, background data samples can be created by selecting events which fail a specific cut.

A pictorial representation of a bifurcated analysis is shown in Fig. 4.11. If cut1 and cut2 are designed to target a specific type of background and are assumed to be uncorrelated, then the number of background events in signal region A relative to that in region B in the parameter space of cut1 and cut2 must be equal to the background events in region C relative to region D. Applying cut2 to the inverted cut1 sample, one can get the number of events in region B, which will be referred to as *normalization*. Then measuring the *rejection* of cut1 on a sample which fail cut2 via  $R = (C + D)/C$ , the background level in signal region A can be calculated as:

$$N_{bg} = BC/D = B/(R - 1) \quad (4.2)$$

Thus, in a bifurcated analysis, the measurement of background in the signal region is restricted to the measurement of the number of events outside the signal region.

Whenever possible, the background sample is extracted from the real data as opposed to modeling the background with Monte Carlo simulations. This is because the reliability of the simulation of various physical processes involved is limited due to uncertainties in nuclear and photo-nuclear total and differential cross-sections. These can lead to large uncertainties when extrapolating to sensitivities of the order of  $10^{-10}$ . Nevertheless, in some cases this method is the only one available because certain cuts suppress many different backgrounds with similar signatures. Therefore, by inverting one of them, it is not possible to clearly select a certain background and measure the rejection of other cuts on it, and the background will be over- or under-estimated. Moreover, since the level of these backgrounds is very small, the samples needed to measure the normalization or rejection run out of statistics after applying some preliminary purification cuts. This is the case for the  $K_{e4}$ ,  $K_{\pi2\gamma}$  and CEX backgrounds, which cannot be easily separated from the much more abundant  $K_{\pi2}$  scatter and double-beam events.

To detect and avoid any bias in the cuts, background measurements are performed twice on independent data samples. The data set is partitioned into one-third and two-third samples uniformly throughout the run, and cuts are designed and the background level is measured using the one-third sample. When the background estimate from the one-third sample is found to be within the acceptable limit, the cuts are frozen and the background level is re-measured using the two-third sample. If the cuts are unbiased, the one-third and the two-third samples should give the same result within statistical uncertainty when scaled appropriately to represent the entire data set. Nonetheless, the background is estimated using the unbiased two-third sample, is then cor-



rected for the whole data sample and is accepted as the final background measurement for the analysis.

### 4.3.2 Validity checks: outside-the-box study

The validity of the bifurcation method relies on the assumptions that (a) the bifurcated cuts are uncorrelated and (b) that all the background types are known and the cuts to suppress them are pre-identified. The assumption that the bifurcated cuts are uncorrelated can be tested by loosening the cuts, recalculating the background levels at these looser cut positions, and comparing it to the observed number of events in these “outside the box” regions. Fig. 4.12 shows a schematic explanation of this method. A new signal region  $A'$  larger than  $A$  is defined, and the expected background in it is calculated with the same method described above. Then the background in the unmasked part of this region will be

$$bg' = bg(A') - bg(A) = B'C'/D' - BC/D \quad (4.3)$$

Since the region is close but still outside the box, it can be examined and the events in it counted. If the number of events observed is different than that predicted, a correlation between cuts or a new source of background may be present, which invalidates the bifurcated background estimate for the box.

### 4.3.3 Acceptance measurement

The acceptance of most of the online and offline cuts is measured with monitor data samples of the dominant  $K_{\mu 2}$  and  $K_{\pi 2}$  decays and beam pions. Each

such sample resembles the signal in different aspects. Therefore, the photon veto, beam, target and reconstruction cuts (the ones that do not depend on the charged particle being a pion) acceptance, as well as the trigger acceptance loss due to accidental activity in the detector, is calculated with  $K_{\mu 2}$  decays. This sample is not expected to have photon activity and the charged track rarely scatters in the detector, so it is generally better reconstructed compared to other monitor samples.  $K_{\mu 2}$  decays are also kinematically well-separated from the beam pion band, making them suitable for the beam cuts acceptance measurement.

The acceptance of the reconstruction and target cuts that are specifically targeted to pions is measured with  $K_{\pi 2}$  decays. This is a well-reconstructed pion sample (the target reconstruction of beam pions is unreliable, due to the closeness of the “Kaon” and “pion” clusters in time), like the signal, and its kinematics can be required to be the ones of the  $K_{\pi 2}$  peak, in order to suppress inelastic scatters.

The beam pion monitors are used for the acceptance of some pion-specific reconstruction cuts, the kinematic cuts and the  $\pi^+ \rightarrow \mu^+ \rightarrow e^+$  decay chain muon veto cuts. Due to the lack of photon activity in this sample, the reconstruction efficiency is more signal-like than for  $K_{\pi 2}$  decays. Beam pions also spread kinematically in the whole  $\pi\nu\bar{\nu}(2)$  region, therefore they are suitable to measure the kinematic cuts acceptance.

The trigger, phase space and solid angle acceptance is measured with signal  $K^+ \rightarrow \pi^+ \nu \bar{\nu}$  decays generated with Monte Carlo, because no monitor sample has the same kinematics with the signal. The acceptance loss due to pion nuclear interactions and decay in flight is also measured with simulated signal

events.

The RS trigger counters' ( $T \bullet 2$ ) efficiency due to gaps between the counters and photostatistics has to be separately measured, using a special monitor sample ( $KB$ ) that does not require  $T \bullet 2$  in the trigger, and signal Monte Carlo.  $K_{\pi 2}$  events are reconstructed from this sample without the  $T \bullet 2$ , and then the trigger bit efficiency is measured. The result is scaled for the higher energy deposit of  $\pi\nu\bar{\nu}(2)$  pions compared to  $K_{\pi 2}$  in the T counter, using signal and  $K_{\pi 2}$  Monte Carlo.

Finally the fraction of Kaons stopping in the target ("Kaon stopping fraction"  $f_s$ ) has been calculated in [40], using  $K_{\mu 2}$  monitor data and Monte Carlo. The number of  $K_{\mu 2}$  decays at rest is divided by the total number of kaons that entered the detector times the  $K_{\mu 2}$  Branching Ratio. The acceptance of the cuts needed to select stopped Kaons is calculated with data or Monte Carlo, whichever is appropriate for every cut. The value for  $f_s = 0.7740 \pm 0.0011$  found in the  $\pi\nu\bar{\nu}(1)$  analysis will be used in this analysis, too.

After all those measurements, the Single Event Sensitivity ("S.E.S."), a measure of the potential of E949 to find a  $K^+ \rightarrow \pi^+\nu\bar{\nu}$  event in the  $\pi\nu\bar{\nu}(2)$  region, is given by

$$S.E.S. = A_{tot} \times \epsilon_{T \bullet 2} \times f_s \times KB_{live} \quad (4.4)$$

where  $A_{tot}$  is the total acceptance of the online and offline cuts,  $\epsilon_{T \bullet 2}$  is the  $T \bullet 2$  efficiency and  $KB_{live} = 1.77 \times 10^{12}$  the total number of Kaon decays in the detector during the data taking.

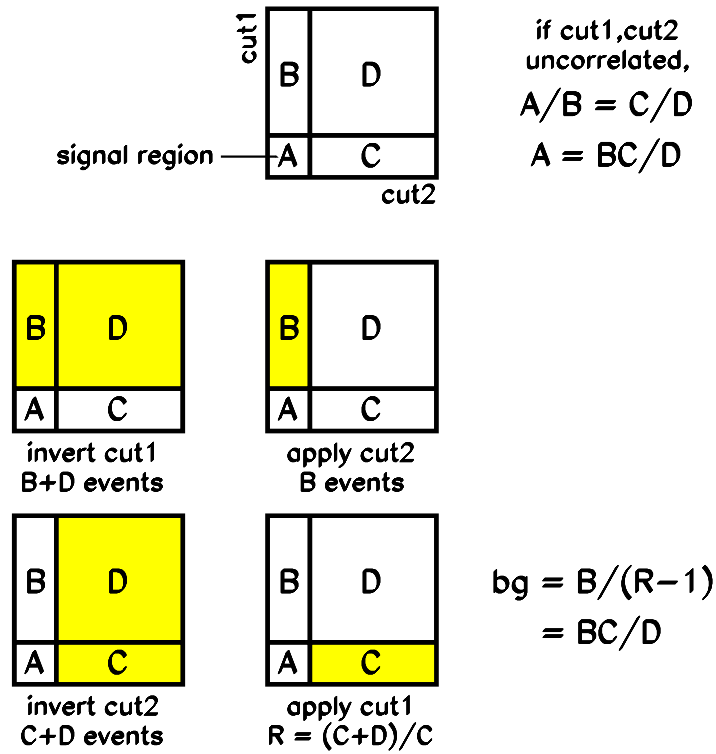


Figure 4.11: A background estimate resulting from a bifurcated analysis. The letters signify both the samples and the number of events in them.

Top: If a certain background is suppressed by cut1 and cut2, then the data sample can be represented in the parameter space of these two cuts as 4 sub-samples A, B, C and D. If these cuts are uncorrelated, then the number of background events in region A relative to that in B is equal to that in C relative to D.

Middle: Count events that fail cut1 and pass cut2 to get the normalization B. Bottom: Select events that fail cut2, and measure the rejection of cut1 via  $R = (C + D)/C$ . Region A is never examined in this procedure. The background estimated to be present in region A is given by  $BC/D = B/(R - 1)$ .

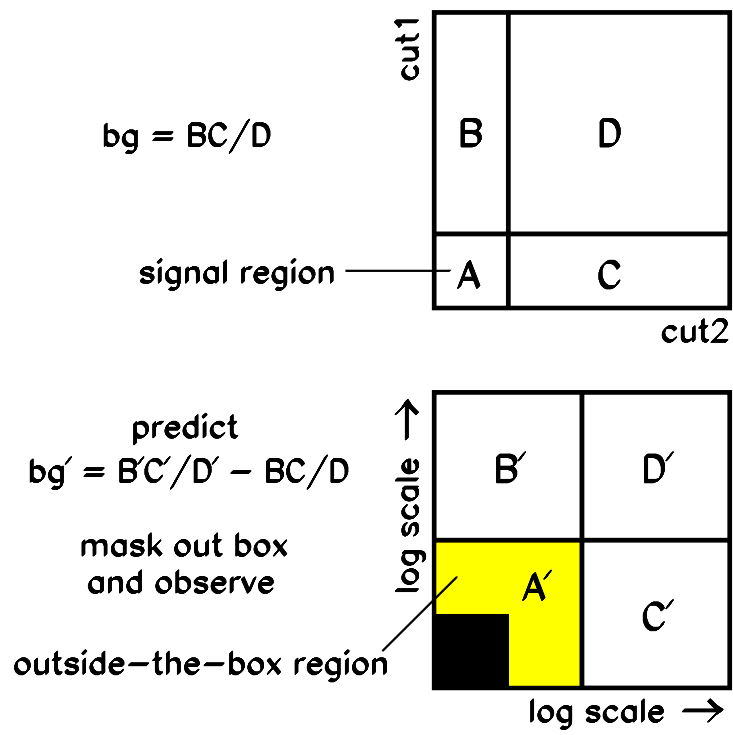


Figure 4.12: Schematic representation of the outside-the-box study.

# Chapter 5

## Background estimation

The expected background level for all processes that contribute in the  $\pi\nu\bar{\nu}(2)$  signal region are calculated in this chapter, using the methods described in section 4.3. The results are multiplied by 3, in order to scale to the total sample (they are calculated using 1/3 of the data), and whenever there remain zero events in the bottom of the normalization or rejection branch, one event is used for the calculations.

### 5.1 $K^+ \rightarrow \pi^+\pi^0$ Target scatters

The  $K_{\pi 2}$  decay, where the  $\pi^+$  scatters in the Target, is the dominant background for the  $\pi\nu\bar{\nu}(2)$  analysis. As it has been shown with Monte Carlo simulations [41], the photon distribution from the  $\pi^0$  decay is more uniform in polar angle for events where the  $\pi^+$  has scattered in the target, than for unscattered ones. Therefore, the Photon Veto (PV) rejection for TG scatter events is expected to be different than that for  $K_{\pi 2}$  events in the peak. The

$\pi^+$  kinematics cannot be used anymore in the bifurcation study, since the PV rejection has to be measured inside the  $\pi\nu\overline{\nu}(2)$  kinematic box.

The other set of cuts used to suppress this background are the target quality cuts (TGCUT06). These eliminate events with evidence of a scattered pion in the target, either the scatter occurred outside the Kaon fibers (scatters visible in xy, or “xy-scatters”) or inside them (events where the  $\pi^+$  started in the beam direction and then scattered into the detector acceptance, or “z-scatters”). The two categories are not mutually exclusive. By inverting some of these cuts and applying others, samples with varying mixtures of xy- and z-scatters can be created for the rejection branch. These samples will be contaminated to an extent with  $K_{e4}$  and  $K_{\pi2\gamma}$  decays and Charge Exchange background, but these backgrounds are small compared to  $K_{\pi2}$  target scatters, as shown in the following sections. Thirteen such “classes” were used, described in Table 5.1, and the PV rejection was measured on them in the  $\pi\nu\overline{\nu}(2)$  kinematic box. The rejection in the  $K_{\pi2}$  peak is also given for comparison. The PV rejections measured for different classes are consistent with each other within statistical uncertainties.

For the final PV rejection, class 12 was used, because it had adequate statistics and it is expected to be the richest in z-scatters, since the cuts that majorly attack them are inverted: CCDPUL and EPIONK cut events with large pulses in the kaon fibers at trs, and B4EKZ rejects events in which the z position of the decay vertex found by the UTC does not agree with the kaon energy deposit (and thus path length) in the target. Both these signatures are characteristic of a decay pion that started in the beam direction in the kaon fiber, and then scattered into the detector. The second pulse energy

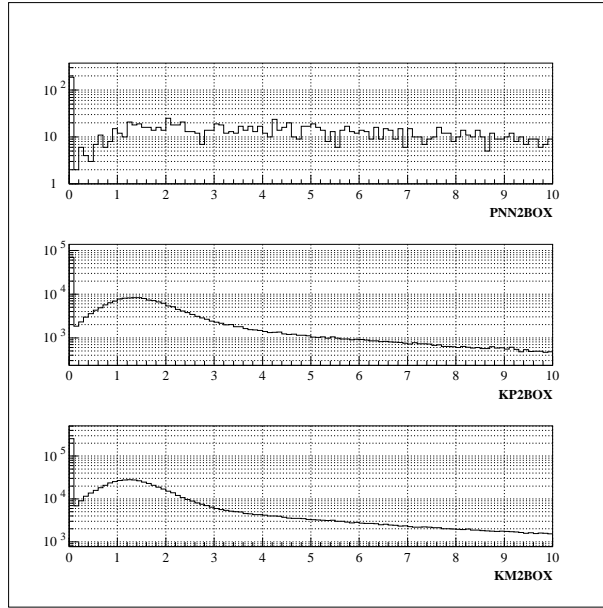


Figure 5.1: Energy distribution of the second pulse in the Kaon fiber for class 12 of the  $K_{\pi 2}$  TG scatter rejection branch (top), for  $K_{\pi 2}$  peak events (middle) and for  $K_{\mu 2}$  events (bottom).

distribution for class 12,  $K_{\pi 2}$  peak events, and  $K_{\mu 2}$  events is shown in Fig. 5.1. The difference in PV rejection between different classes with adequate statistics will be used as an estimate for the systematic uncertainty.

In the normalization branch (see Table 5.2), all the cuts in TGCUT06 were applied, and the PV was inverted. Some contamination from  $K_{\pi 2}$  RS scatters and  $K_{\pi 2\gamma}$  is expected, but these backgrounds are small compared to  $K_{\pi 2}$  TG scatters. The  $p_{\text{tot}}$  distribution of the events remaining in the normalization branch after the inversion of PVCUTPNN2, after the application of all the TGCUT06 except CCDPUL, and after the application of CCDPUL is shown in Fig. 5.2. In the same figure, the  $p_{\text{tot}}$  distribution of the events in class 12 of the rejection branch is also shown before and after PVCUTPNN2.



| CLASS | TGCUTS   | PV rejection          |
|-------|--|-----------------------|
| 1     | All cuts, KP2BOX   | 30536/27=1131.0±217.6 |
| 2     | $\overline{CCDPUL}, \overline{EPIONK}$   | 29758/18=1653.2±389.5 |
| 3     | $\overline{CCDPUL}, \overline{EPIONK}$ , all others  | -                     |
| 4     | $\overline{CCDPUL}, \overline{EPIONK}, \overline{TGZFOOL}, \overline{EIC}, \overline{OPSVETO}, \overline{OTHERS}$                                  | -                     |
| 5     | $\overline{CCDPUL}, \overline{EPIONK}, \overline{CHI567}, \overline{VERRNG}$   | 35463/20=1773.2±396.4 |
| 6     | $\overline{CCDPUL}, \overline{EPIONK}, \overline{CHI567}, \overline{VERRNG}$ , all others  | -                     |
| 7     | $\overline{CHI567}, \overline{VERRNG}$   | 40114/17=2359.7±572.2 |
| 8     | $\overline{CHI567}, \overline{VERRNG}$ , all others  | -                     |
| 9     | $\overline{CCDPUL}, \overline{EPIONK}, \overline{CHI567}, \overline{VERRNG}, \overline{KIC}, \overline{PIGAP}, \overline{TARGF}, \overline{TPICS}$ | 29289/17=1722.9±417.7 |
| 10    | $\overline{B4EKZ}$   | 14076/8=1759.5±621.9  |
| 11    | $\overline{B4EKZ}$ , all others  | -                     |
| 12    | $\overline{CCDPUL}, \overline{EPIONK}, \overline{B4EKZ}$   | 31568/18=1753.8±413.3 |
| 13    | $\overline{CCDPUL}, \overline{EPIONK}, \overline{B4EKZ}$ , all others  | -                     |

Table 5.1: Classes of events (2-13) used to measure the PV rejection in the  $\pi\nu\overline{\nu}(2)$  kinematic box, number of events before and after the PV is applied, and the rejection found. The classes that are skipped do not have enough statistics for a meaningful measurement. The PV rejection in the  $K_{\pi 2}$  kinematic peak, after all cuts in TGCUT06 were applied, is also given in CLASS 1. The same setup cuts as in the normalization branch (Table 5.2) are applied.

| CUT                        | Events   |
|----------------------------|----------|
|                            | 30983002 |
| BAD_RUN,KERROR             | 30397640 |
| SKIM5,RECON                | 10480765 |
| PSCUT06                    | 3226493  |
| DELCO3                     | 3207512  |
| KCUT                       | 476055   |
| <i>PVCUTPNN2</i> , PNN2BOX | 49246    |
| B4EKZ(IC)                  | 35178    |
| TGZFOOL                    | 34672    |
| EPITG                      | 19694    |
| EPIMAXK                    | 19694    |
| TARGF                      | 16996    |
| DTGTTP                     | 16991    |
| RTDIF                      | 16838    |
| DRP                        | 16610    |
| TGKTIM                     | 16327    |
| EIC                        | 15867    |
| TIC                        | 15867    |
| TGEDGE                     | 15514    |
| TGDEDX                     | 12319    |
| TGENR                      | 11780    |
| PIGAP                      | 11567    |
| TGB4                       | 10471    |
| KIC                        | 10467    |
| PHIVTX                     | 8326     |
| OPSVETO                    | 7380     |
| TGLIKE                     | 6979     |
| TIMKF                      | 5643     |
| NPITG                      | 5643     |
| ALLKFIT                    | 5243     |
| TPICS                      | 5237     |
| EPIONK                     | 5018     |
| CHI567                     | 3317     |
| VERRNG                     | 2836     |
| CHI5MAX                    | 2787     |
| ANGLI                      | 2779     |
| CCDBADFIT                  | 2239     |
| CCDPUL                     | 280      |

Table 5.2: The normalization branch for the  $K_{\pi 2}$  target scatter background.

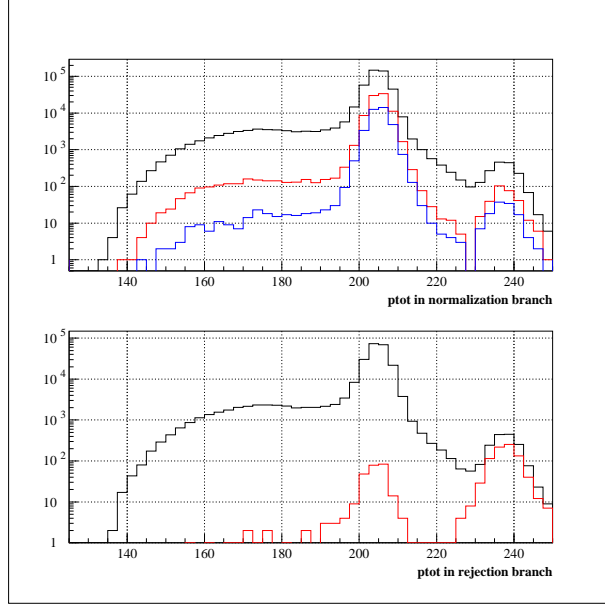


Figure 5.2: Top:  $ptot$  distribution of the events remaining in the normalization branch of the  $K_{\pi 2}$  TG scatter study after the inversion of PVCUTPNN2 (black), after the application of all the TGCUT06 except CCDPUL (red), and after the application of CCDPUL (blue). Bottom:  $ptot$  distribution of the events in class 12 of the rejection branch of the  $K_{\pi 2}$  TG scatter study before (black) and after (red) PVCUTPNN2.

Using the numbers from tables 5.2 and 5.1, the  $K_{\pi_2}$  target scatter background is

$$N_{K_{\pi_2}-TGscat} = 3 \times \frac{N}{R_{PVclass12}-1} = 3 \times \frac{280}{(1753.8 \pm 413.3)-1} = 0.479 \pm 0.116(stat.)^{+0.029}_{-0.123}(sys.) \quad (5.1)$$

## 5.2 $K^+ \rightarrow \pi^+ \pi^0$ Range Stack scatters

Pions from the  $K_{\pi_2}$  decay can also undergo inelastic scattering in the Range Stack and fall into the  $\pi\nu\overline{\nu}(2)$  kinematic box by losing energy in the scattering process. However, for these events to be a background for this analysis, the pion momentum also has to be mis-measured and the photons from the  $\pi^0$  decay have to be missed. Therefore, this background is expected to be smaller compared to the  $K_{\pi_2}$  target scattered background.

It should be noted that these background events are already included in the normalization branch in Table 5.2<sup>1</sup>, but they are not included in the Photon Veto rejection study in Table 5.1 because the target cuts were reversed to measure this Photon Veto rejection. The  $K_{\pi_2}$  events which scattered in the RS should be assigned the same Photon Veto rejection as the  $K_{\pi_2}$  peak events, since the pion did not scatter in the target.

The most effective cuts against this background are the Range Stack track quality cuts RSDIDX and PRRF (collectively referred to as RSCT), the BOX

---

<sup>1</sup>Correcting the normalization of  $K_{\pi_2}$  TG scatters for  $K_{\pi_2}$  RS scatters does not make a significant difference in the background, given the statistical uncertainty.

| CUT       | Rejection        |             | Normalization                            |         |
|-----------|------------------|-------------|--|---------|
|           | PBOX from KP2BOX | PNN2 RE BOX | $\overline{RSDEDX}$ or $\overline{PRRF}$ |         |
|           | KP2BOX           | PNN2        | KP2BOX                                   | PNN2BOX |
| SETUP     | 52840            | 678         | 15496                                    | 2896    |
| LAYER14   | 52754            | 678         | 15456                                    | 2896    |
| FIDUCIAL  | 48275            | 609         | 13843                                    | 2798    |
| UTCQUAL   | 42845            | 516         | 11894                                    | 2191    |
| RNGMOM    | 42160            | 516         | 11624                                    | 111     |
| RSDEDX    | 36737            | 104         | NA                                       | NA      |
| PRRF      | 30536            | 73          | NA                                       | NA      |
| PVCUTPNN2 | 27               | 0           | 9  | 1       |

Table 5.3: Background study for  $K_{\pi 2}$ RS scatters. PBOX is the momentum cut and RE BOX the range and energy cut. “NA” means that the cut is not applied, because the RSCT cuts have been reversed in the normalization branch.

cut on  $ptot$  and the Photon Veto cut. Table 5.3 summarizes this background study. The SETUP cuts are the same as the  $K_{\pi 2}$  target scatter normalization branch. The second and the third columns of the table contain events in the  $K_{\pi 2}$  momentum peak. Events with the momentum of the  $K_{\pi 2}$  peak events, but lowered in range and energy are assumed to have scattered in the Range Stack.

The efficiency  $\epsilon_{RSCT}$  and the rejection  $R_{RSCT}$  of these cuts can be measured as

$$\begin{aligned}
\epsilon_{RSCT} &= 30536/42160 = 0.724 \pm 0.002 \\
R_{RSCT} &= 516/73 = 7.068 \pm 0.766
\end{aligned} \tag{5.2}$$

The fourth and fifth column of Table 5.3 are for normalization. The RSCT cut is reversed and all other cuts are applied. The various contributions to the

total 111 events left in the PNN2BOX before the application of the PV have to be considered in order to calculate the background of interest. The largest component of this sample comes from scattering in the target that contaminated the RSCT reversed sample because of the inefficiency of the RSCT cuts. On the other hand, the total 280 events in the  $K_{\pi 2}$  target scatter normalization branch (Table 5.2) have a target scattered ( $N_{tg}$ ) and a RS scattered ( $N_{rs}$ ) component. Therefore

$$\begin{aligned} N_{tg} + N_{rs} &= 280 \\ (1 - \epsilon_{RSCT}) \times N_{tg} + (R_{RSCT} - 1) \times N_{rs} &= 111 \end{aligned} \quad (5.3)$$

Solving this system of equations, the real  $K_{\pi 2}$  RS scatter normalization is obtained,  $N_{rs} = 5.822 \pm 0.776$ . The final background from the RS scattered events can be measured by applying the  $K_{\pi 2}$  peak Photon Veto rejection to  $N_{rs}$  from the second column of Table 5.3,  $R_{PV-K_{\pi 2}peak} = 30536/27 = 1131.0 \pm 217.6$ :

$$N_{K_{\pi 2}-RSscat} = 3 \times \frac{N_{rs}}{R_{PV-K_{\pi 2}peak} - 1} = 3 \times \frac{5.822 \pm 0.776}{(1131.0 \pm 217.6) - 1} = 0.015 \pm 0.004 \quad (5.4)$$

## 5.3 Beam background

### 5.3.1 Single beam

The two cuts that suppress this background are DELCO3 and B4DEDX. In the rejection branch, after some basic setup cuts, B4DEDX is inverted, requiring

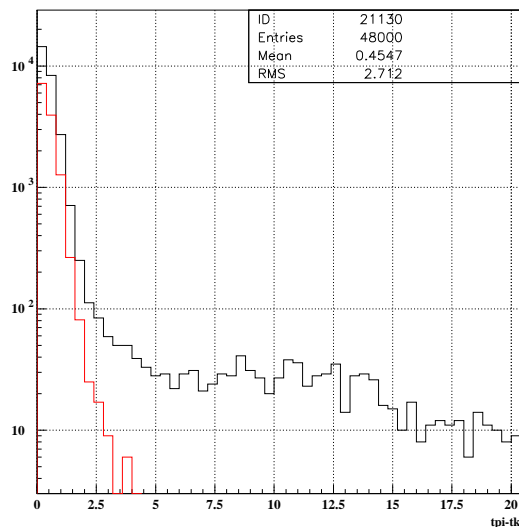
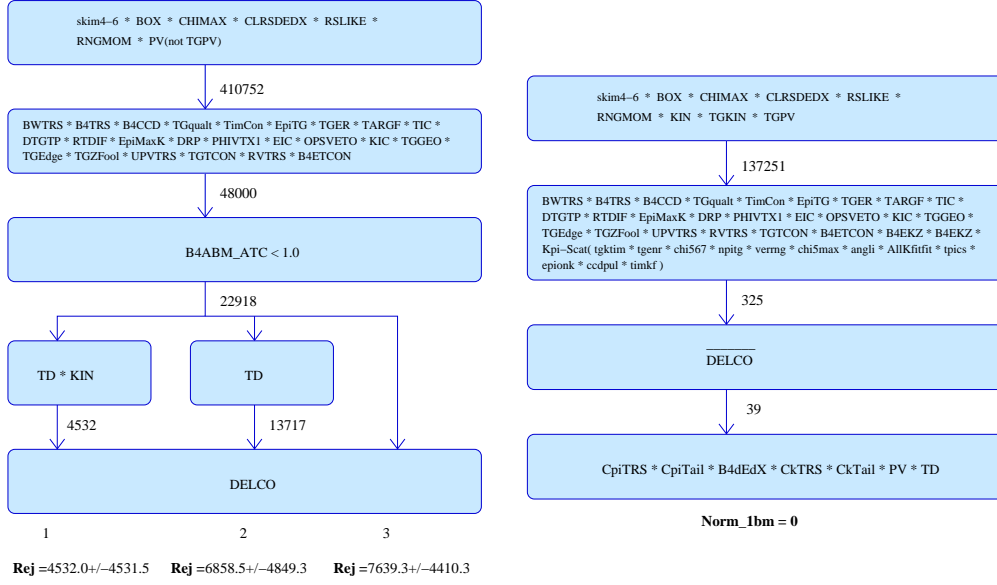


Figure 5.3: Tpi-tk distribution of events in the single beam background rejection branch before (black) and after (red) the inversion of B4DEDX.

B4 energy consistent with a pion ( $b4abm_{atc} < 1.0 MeV$ ), and the DELCO3 cut rejection is measured on this sample. The tpi-tk distribution before and after the inversion of B4DEDX is shown in Fig. 5.3. The branch is divided into 3 sub-branches before DELCO3 is applied, of varying purity. It is assumed that the DELCO3 rejection is the same for beam pions and kaons. In the normalization branch, DELCO3 is inverted and all other relevant cuts are applied. The schematic of the two branches, together with the number of events that survive after every (set of) cut(s), is shown in Fig. 5.4. Using these numbers, the single-beam background in the 3/3 sample is



(a) Rejection

(b) Normalization

Figure 5.4: Single beam bifurcations: (a) rejection branch, with the values of the DELCO3 rejection obtained for the 3 sub-branches, and (b) normalization branch. Numbers under the boxes are the number of events remaining after the cuts were applied. TD is the TDCUT02 cut, and KIN the KCUT cut.



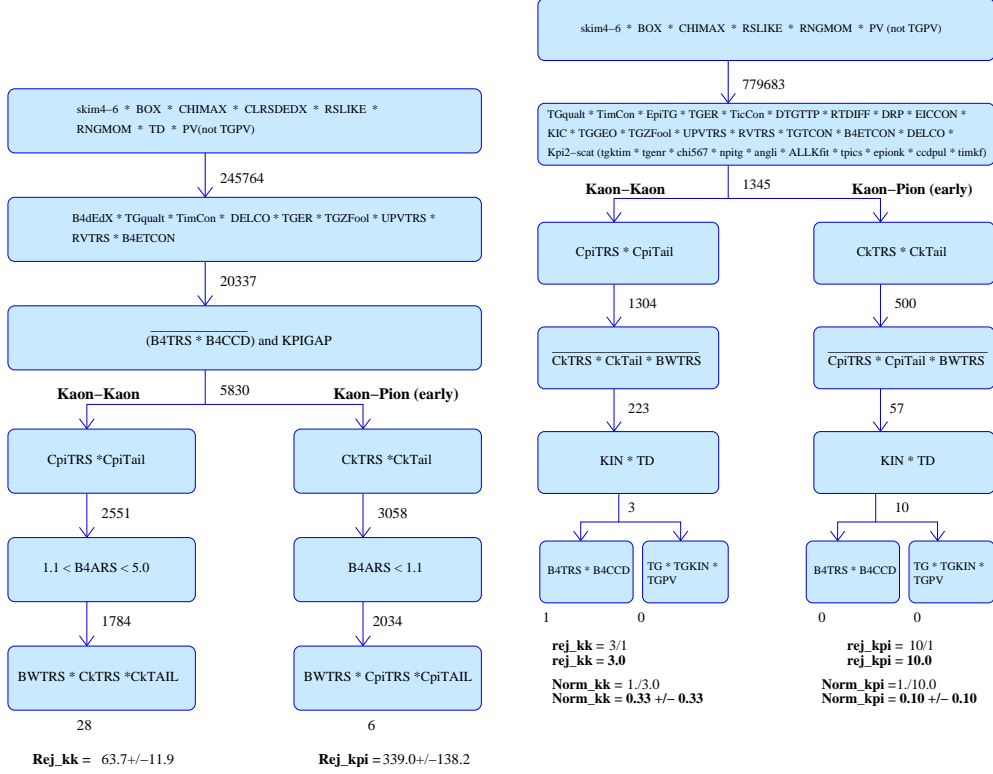
$$\begin{aligned}
N_{1bm} &= 3 \times \frac{A_{PV_{pnn2}}}{A_{PV_{beam}}} \times \frac{Norm_{1bm}}{R_{DELCO}-1} \\
N_{1bm} &= 3 \times \frac{0.58}{0.85} \times \frac{1.0 \pm 1.0}{(4532.0 \pm 4531.5) - 1} = (0.45 \pm 0.64) \cdot 10^{-3} \quad (5.5)
\end{aligned}$$

where  $\frac{A_{PV_{pnn2}}}{A_{PV_{beam}}} = \frac{0.58}{0.85}$  is the ratio of the acceptance of the nominal PNN2 photon veto cut and the looser PV cut used to produce the beam study numbers (see B). For a conservative estimate of the background, the smallest value of  $R_{DELCO}$  from the 3 rejection sub-branches is used.

### 5.3.2 Double beam

In order to calculate this background, it is assumed that the Čerenkov counter and the Beam Wire Chambers are uncorrelated with the B4 and the Target, since the Degraders, where the beam particles undergo multiple scattering, are located between them. Therefore, for the rejection branch, 2-beam events are tagged by requiring a hit in the B4 at RS time, and the rejection of the BWCs and the K- or  $\pi$ -Čerenkov (Ck and Cpi respectively) is measured on this sample. In the normalization branch, either the BWCs, or Ck or Cpi are required to have a hit at RS time and all other cuts are applied. A schematic of the 2-beam bifurcation study is shown in Fig. 5.5.

In addition to the B4-tag, KPIGAP is also applied in the rejection branch, which requires the Kaon and pion cluster in the Target to be disconnected in xy. This is done to remove K-decay contamination from the 2-beam sample: either a photon from  $K_{\pi 2}$  or a charged particle from a multibody decay, both relevant in the PNN2 kinematic region, can give a signal in the B4 at RS time,



(a) Rejection

(b) Normalization

Figure 5.5: Double beam Bifurcations: (a) rejection branch, and (b) normalization branch, for both K-K and K- $\pi$ . Numbers under the boxes are the number of events remaining after the cuts were applied. The K- $\pi$  numbers are for the early runs (before the change in trigger) and the K-K numbers are from all runs.

faking a second beam particle in the B4. Such events are not expected to have any BWC or Čerenkov rejection, and should be removed, in order to measure the BWC and Čerenkov rejection correctly. On the other hand, the rejection of the beam counters does not depend significantly on the proximity of the 2 beam particles, therefore such a subset of events with spatially disconnected beam particles, can be used to measure the rejection.

Both the rejection and normalization branches bifurcate into K-K and K- $\pi$  sub-branches, requiring a Cpi or Ck veto respectively, before either inverting Ck or Cpi (in the normalization branch), or measuring the Ck or Cp rejection (in the rejection branch). The normalization branch bifurcates further at the bottom, in order to handle the small statistics, therefore the K-K (K- $\pi$ ) normalization numbers are given by

$$Norm_{KK(K\pi)} = \frac{n_{KK(K\pi)}}{r_{KK(K\pi)}} \quad (5.6)$$

where  $n_{KK(K\pi)}$  is the number of events remaining in the B4TRS\*B4CCD sub-branch, and  $r_{KK(K\pi)}$  the rejection of TG\*TGKIN\*TGPV.

### **K-K background**

Using the method described above, and the results from Fig. 5.5, the K-K 2-beam background is

$$N_{KK} = 3 \times \frac{A_{PV_{pnn2}}}{A_{PV_{beam}}} \times \frac{Norm_{KK}}{R_{KK} - 1} \quad (5.7)$$

and, using Eq. (5.6),

$$N_{KK} = 3 \times \frac{0.58}{0.85} \times \frac{\frac{1.0 \pm 1.0}{3.0 \pm 2.4}}{(63.7 \pm 11.9) - 1} = 0.0107 \pm 0.0141 \quad (5.8)$$

### K- $\pi$ background

A complication arises when the K- $\pi$  double beam background is to be calculated, due to the addition of the Cpi veto to the online trigger in the middle of the run (see section 3.4). The offline Cpi rejection is very low for the late part of the run, and the normalization branch runs out of statistics, producing an unnaturally high background estimate with large uncertainty. Therefore it is impossible to just add the K- $\pi$  background for the early and late part of the run. Instead, the background calculated for the set of runs before the trigger change was scaled by the ratio of  $KB_{live}$  of the two parts of the run  $f_{KB_{live}} = \frac{0.606}{0.394} = 1.54$ . This approach is justified by the fact that the K- $\pi$  background measured for the early and late part of the run for  $\pi\nu\overline{\nu}(1)$  triggers agree with each other. The K-K background calculated for the early and late runs for  $\pi\nu\overline{\nu}(2)$  is also consistent [42]. Everything indicates that there was no increase in beam background after the trigger change occurred, therefore scaling by  $f_{KB_{live}}$  is valid. The K- $\pi$  background is thus

$$\begin{aligned} N_{K\pi} &= 3 \times \frac{A_{PV_{pn2}}}{A_{PV_{beam}}} \times (1 + f_{KB_{live}}) \times \frac{Norm_{K\pi}}{R_{K\pi}-1} \\ N_{K\pi} &= 3 \times \frac{0.58}{0.85} \times (1 + 1.54) \times \frac{\frac{1.0 \pm 1.0}{10.0 \pm 9.5}}{(339.0 \pm 138.2) - 1} = (1.54 \pm 2.24) \cdot 10^{-3} \quad (5.9) \end{aligned}$$

### 5.3.3 Total beam background

Summarizing the previous results, the total beam background expected in the signal region for the 3/3 sample is

$$N_{beam} = N_{1bm} + N_{KK} + N_{K\pi} = (12.7 \pm 14.3) \cdot 10^{-3} \quad (5.10)$$

This expected background is an improvement of about a factor of 10 compared to the E787 result [39], and is consistent with the  $\pi\nu\bar{\nu}(1)$  background, given the difference in phase space of the two kinematic regions.

## 5.4 Muon backgrounds

The muon background is expected to come mainly from  $K^+ \rightarrow \mu^+\nu\gamma$  and  $K^+ \rightarrow \pi^0\mu^+\nu$  decays in the  $\pi\nu\bar{\nu}(2)$  kinematic region. However, this background is expected to be small, because for these processes to be confused with signal, both the muon has to be misidentified as a pion and the photon(s) have to be missed. The cuts used to suppress the muon background are the  $\pi^+ \rightarrow \mu^+ \rightarrow e^+$  decay sequence cuts (TDCUT02) and the pion-muon kinematic separation cut RNGMOM.

After some setup cuts that remove  $K_{\pi 2}$  decays and beam backgrounds, in the normalization branch (Table 5.4) TDCUT02 is inverted. When the remaining cuts are applied (KCUTS and PVPNN2), no events remain in the normalization branch, therefore N=1 will be used for the background estimation. In the rejection branch (Table 5.5), RNGMOM is inverted and the rejection of the TDCUT02 is measured on this sample. Using these values,

| CUT            | events  |
|----------------|---------|
| PNN2BOX        | 4649482 |
| PSCUT06        | 550771  |
| TGCUT06        | 15622   |
| <u>TDCUT02</u> | 2941    |
| KCUTS          | 0       |
| PVCUTPNN2      | 0       |

Table 5.4: Normalization branch for the muon backgrounds.

| CUT                                       | events  |
|---|---------|
| PSCUT06                                   | 5971094 |
| TGCUT06                                   | 652242  |
| <u>RNGMOM</u>                             | 485160  |
| other KCUTS                               | 24294   |
| PVCUTPNN2                                 | 3368    |
| EV5                                       | 1707    |
| ELVETO                                    | 988     |
| TDFOOL                                    | 986     |
| TDVARNN                                   | 8       |
| Total $R_{TD} = 3368/8 = 421.0 \pm 148.7$ |         |

Table 5.5: Rejection branch for the muon backgrounds.

the muon background is

$$N_\mu = 3 \times \frac{N}{R_{TD} - 1} = 3 \times \frac{1 \pm 1}{(421.0 \pm 148.7) - 1} = 0.0071 \pm 0.0076 \quad (5.11)$$

## 5.5 $K^+ \rightarrow \pi^+ \pi^- e^+ \nu$ background

The  $K_{e4}$  decay with a BR of  $(4.08 \pm 0.09) \times 10^{-5}$  and with the  $\pi^+$  maximum momentum at 203 MeV/c could be a serious background in the PNN2 region

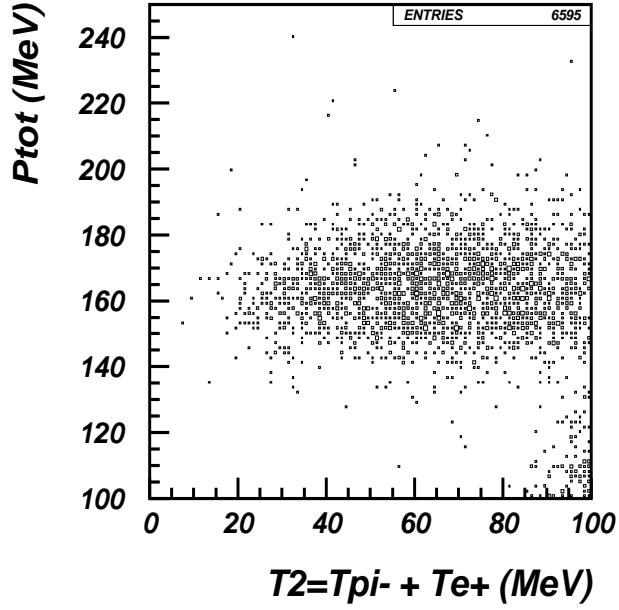


Figure 5.6: Total kinetic energy ( $T_2$ ) of the  $\pi^-$  and the  $e^+$  versus the momentum of the  $\pi^+$  ( $P_{tot}$ ) for  $K^+ \rightarrow \pi^+\pi^-e^+\nu$  Monte Carlo events that pass the  $\pi\nu\bar{\nu}(2)$  trigger.

because this decay contains no photon in the final state to veto on and the  $\pi^-$  and the  $e^+$  could be undetectable. Fig. 5.6 shows the total kinetic energy ( $T_2$ ) of the  $\pi^-$  and the  $e^+$  versus the momentum of the  $\pi^+$  ( $p_{tot}$ ) for Monte Carlo events that passed the  $\pi\nu\bar{\nu}(2)$  trigger. When  $T_2$  is very low, the  $\pi^-$  and the  $e^+$  can not fly out of the target and they might escape detection if they deposit all their energy in some insensitive material or if their path overlaps with kaon fibers. For these low  $T_2$  events the distribution of  $P_{tot}$  concentrates around 160 MeV, which is in the range of the  $\pi\nu\bar{\nu}(2)$  signal box.

### 5.5.1 Background estimate using data

The two cuts that are most effective against this background are TGPV\*OPSVETO and CCDPUL. TGPV\*OPSVETO removes events with energy deposits outside the kaon and pion fibers (classified as “photon” and “opposite side pion” fibers respectively), and CCDPUL removes events with extra energy deposit in the Kaon fibers.

Two  $K_{e4}$  background branches are selected in data skim5 by  $\overline{TGPV}$ ,  $\overline{OPSVETO}$  or  $\overline{CCDPUL}$ . The number of events remaining after every cut in these branches are listed in Table 5.6. Some cuts have been loosened in this study, in order to avoid revealing part of the signal box, therefore a background estimate using the results of this table will be an overestimation, provided that the background distribution does not change drastically when these cuts are tightened. For instance, the Photon Veto cuts are at a loose setting (85% acceptance and  $146.1 \pm 9.9$  rejection for class 12 of Table 5.1, see plots in Appendix B), the time window and energy threshold of TGPV and OPSVETO have been loosened from their nominal values to 1.3 ns and 5 MeV and 3 ns and 2 MeV respectively, and the CCDPUL energy threshold is set to 2 MeV.

The events that remain at the end of each branch were scanned by eye to understand their nature, and a significant contamination of  $K_{\pi 2}$  scatters,  $K^+ \rightarrow \pi^+ \mu^+ \mu^-$  and other decays was found, among the  $K_{e4}$  ones. Therefore, the data themselves cannot be used to calculate this background, because a clean sample of  $K_{e4}$  cannot be isolated. The  $\overline{TGPV \cdot OPSVETO}$  branch from data will be used for normalization, and the TGPV\*OPSVETO rejection will be calculated with Monte Carlo, in order to get a conservative background



| Cut      | $\overline{TGPV \cdot OPSVETO}$ | $\overline{CCDPUL}$ |
|----------|---------------------------------|---------------------|
| TRIGGER  | 30995248                        | 30995248            |
| PNN2BOX  | 1201592                         | 1201592             |
| PSCUT06  | 423959                          | 423959              |
| TDCUT02  | 179203                          | 179203              |
| KCUTS    | 112435                          | 112432              |
| PRESEL   | 8593                            | 8594                |
| RCUT     | 7346                            | 5923                |
| PVICVC   | 3303                            | 2901                |
| TGCUT06  | 95                              | 122                 |
| FINALCUT | 15                              | 42                  |

Table 5.6: The  $K_{e4}$  normalization branches of data, using  $\overline{TGPV \cdot OPSVETO}$  and  $\overline{CCDPUL}$ . PRESEL contains DELCO6, B4TIM, TGZFOOL and all Photon Veto cuts except that for IC and VC. RCUT means  $\overline{TGPV \cdot OPSVETO}$  in the  $\overline{TGPV \cdot OPSVETO}$  branch and  $\overline{CCDPUL}$  in the  $\overline{CCDPUL}$  branch. FINALCUT means  $\overline{CCDPUL}$  in the  $\overline{TGPV \cdot OPSVETO}$  branch and  $\overline{TGPV \cdot OPSVETO}$  in the  $\overline{CCDPUL}$  branch.

prediction.

The effect of the tighter final PV cut can be accounted for, however, since the sample is contaminated with  $K_{\pi 2}$  TG scatters. Using the PV rejection of class 12 for the loose and nominal PV parameters, the normalization is

$$Norm_{ke4} = \frac{R_{PV_{ke4}}}{R_{PV_{pnn2}}} \times N = \frac{146.1}{1753.8} \times 15 = 1.25 \pm 0.31 \quad (5.12)$$

### 5.5.2 Background study with UMC

In order to understand the rejection of  $\overline{TGPV \cdot OPSVETO}$  and  $\overline{CCDPUL}$ , Monte Carlo is used to simulate the energy deposit of charged tracks in the target. The main source of uncertainty in simulation comes from the absorption of  $\pi^-$  in the target. The  $\pi^-$  absorption is modeled with an experimental

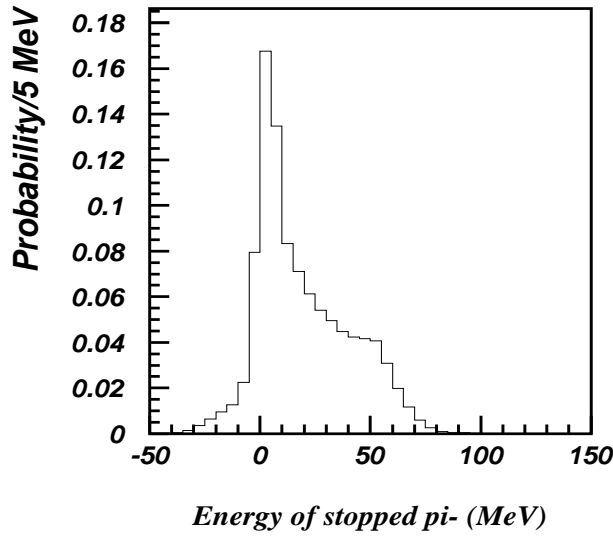


Figure 5.7: Observable absorption energy of  $\pi^-$  stopped in the target.

measurement of stopped  $\pi^-$  in the Range Stack [43]. Fig. 5.7 shows the absorption energy distribution of stopped  $\pi^-$  from that experiment (measured energy deposit - kinetic energy). In simulation, the absorption energy is sampled according to this distribution. If the energy is sampled to be negative, then the last fiber on the  $\pi^-$  trajectory is assigned 0 energy. This model, however, assumes that all the observable energy is deposited locally and promptly, in a single fiber, where the  $\pi^-$  stopped. Possible energy deposit in neighboring fibers from the relatively energetic photons that are produced in  $\pi^-$ -Carbon absorption as well as deposits from neutrons outside the target are not simulated.

About  $2 \times 10^8$  events were simulated using this model, with an additional cut at  $T2 < 50 \text{ MeV}$ , in order to enhance the phase space region most responsible for the background. To study the correlation between TGPV·OPSVETO and CCDPUL, two variables were used: the energy deposit in target fibers out-

| Cut     | Events (Acceptance) |
|---------|---------------------|
| Kstops  | 199998880           |
| TRIGGER | 10691979            |
| PNN2BOX | 9928203             |
| KCUTS   | 7697728             |
| PRESEL  | 3894473             |
| PVICVC  | 2316910             |
| TGCUT06 | 63425               |

Table 5.7: The number of events remaining after all possible PASS2 cuts in  $K^+ \rightarrow \pi^+\pi^-e^+\nu$  Monte Carlo. PRESEL cut means DELCO6, TGZFOOL, and all Photon Veto cuts except that for IC and VC.

side of kaon and pion fibers  $T_{xtg}$ , corresponding to the energy deposits available to TGPV·OPSVETO, and the total energy deposit of pions and electrons in kaon fibers  $E_{hide}$ , corresponding to the energy deposit that would be found by the CCDPUL.

Table 5.7 shows the number of events left after the application of all possible cuts to MC data, and Fig. 5.8 the relation between  $E_{hide}$  and  $T_{xtg}$  for the surviving events. In Table 5.8 the rejection of TGPV·OPSVETO is calculated as a function of the cut on  $E_{hide}$ , which simulates the effect of the *CCDPUL* cut. Since the matching of the energy between MC and Data is uncertain, the cut on  $E_{hide}$  is varied between 1.5 and 10 MeV, and the cut on  $T_{xtg}$  between 0.6 and 1.8 MeV. The rejection of TGPV·OPSVETO does not change much with the value of the threshold, but it shows a correlation with the cut in  $E_{hide}$ . The mean value for the rejection  $R_{TGPV\cdot OPSVETO} = 73$  is used in the evaluation of the background, and the variation with the  $E_{hide}$  cut position from  $R_{TGPV\cdot OPSVETO}^{min} = 13.6$  to  $R_{TGPV\cdot OPSVETO}^{max} = 132.4$  is included in the asymmetric systematic error.

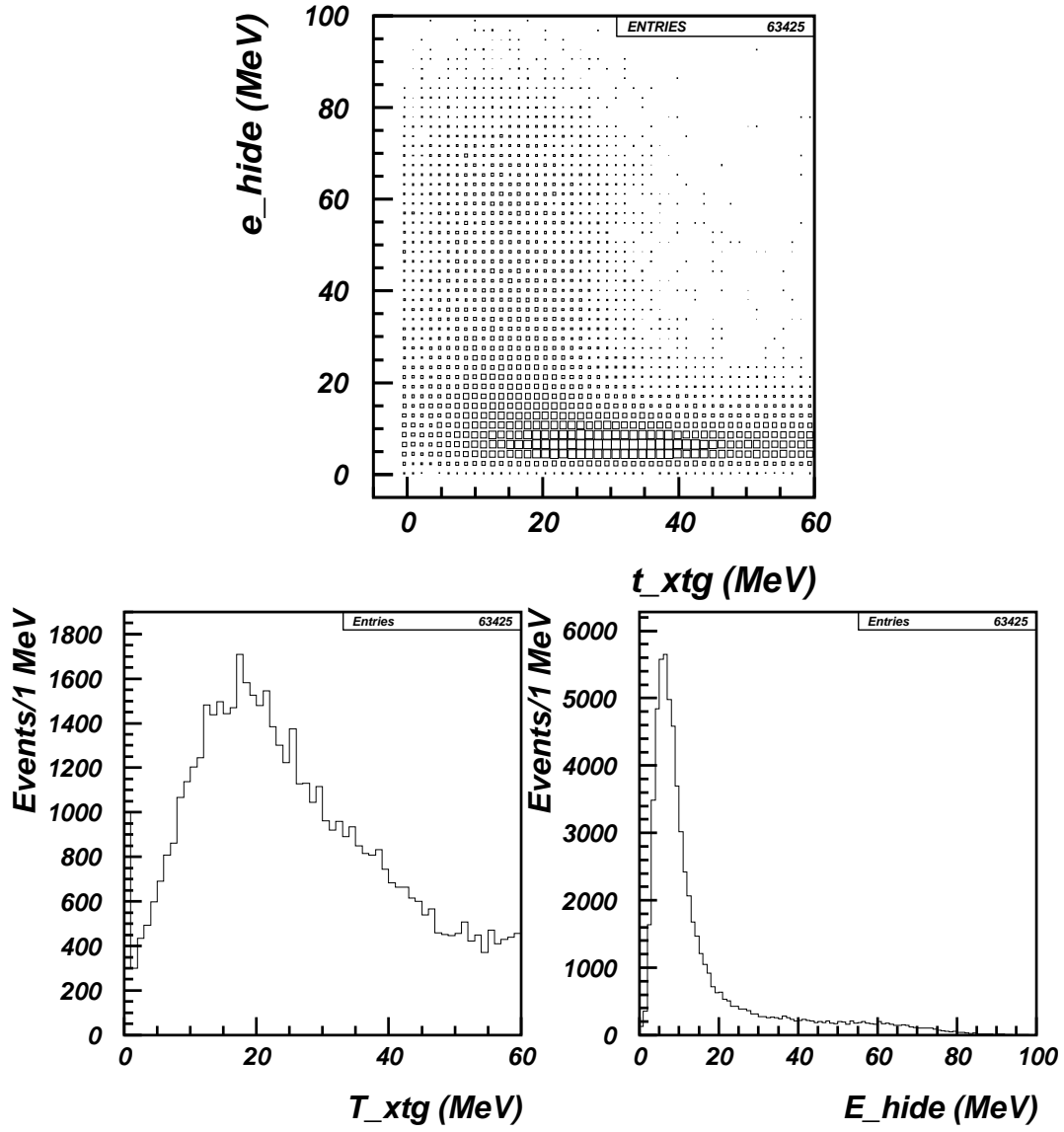


Figure 5.8:  $E_{hide}$  versus  $T_{xtg}$  (top) and projections on  $T_{xtg}$  (bottom left) and  $E_{hide}$  (bottom right) for the  $K^+ \rightarrow \pi^+ \pi^- e^+ \nu$  Monte Carlo events that survive all analysis cuts applicable in UMC.

|                   | $T_{xtg} < 0.6$ | $T_{xtg} < 1.2$ | $T_{xtg} < 1.8$ |
|-------------------|-----------------|-----------------|-----------------|
| $E_{hide} < 1.5$  | 245/12=20.4     | 245/18=13.6     | 245/18=13.6     |
| $E_{hide} < 2.5$  | 1104/27=40.9    | 1104/34=32.5    | 1104/36=30.7    |
| $E_{hide} < 4.0$  | 5609/61=92.0    | 5609/70=80.1    | 5609/78=71.9    |
| $E_{hide} < 10.0$ | 34943/264=132.4 | 34943/313=111.6 | 34943/354=98.7  |

Table 5.8: Rejection of cuts on  $T_{xtg}$  with different cuts on  $E_{hide}$  on  $K^+ \rightarrow \pi^+ \pi^- e^+ \nu$  Monte Carlo events.

Using the results of Table 5.8 and equation 5.12, the  $K_{e4}$  background is found to be

$$N_{ke4} = 3 \times \frac{Norm_{ke4}}{R_{TGPV.OPSVETO} - 1} = 0.052 \pm 0.013(stat.)^{+0.246}_{-0.023}(syst.) \quad (5.13)$$

## 5.6 $K^+ \rightarrow \pi^+ \pi^0 \gamma$

The background due to radiative  $K_{\pi 2}$  is expected to be small, due to the small branching ratio of this decay compared to  $K_{\pi 2}$  and the existence of the third photon available to veto on. From the two processes through which this decay proceeds, direct emission with  $BR(DE) = (4.4 \pm 0.7) \times 10^{-6}$  and inner Bremsstrahlung with  $BR(IB, 55 MeV < T_{\pi^+} < 90 MeV) = (2.75 \pm 0.15) \times 10^{-4}$  [8], the latter is only of interest, due to its higher Branching Ratio.

Since it is difficult to separate this background sample from the  $K_{\pi 2}$ -scatter background sample, both Monte Carlo and data were used to measure it. The method consisted of determining the expected number of  $K_{\pi 2 \gamma}$  events in the  $\pi \nu \overline{P}(2)$  kinematic region as a function of the number of  $K_{\pi 2}$  peak events observed outside the search region. In order to normalize the number of  $K_{\pi 2 \gamma}$

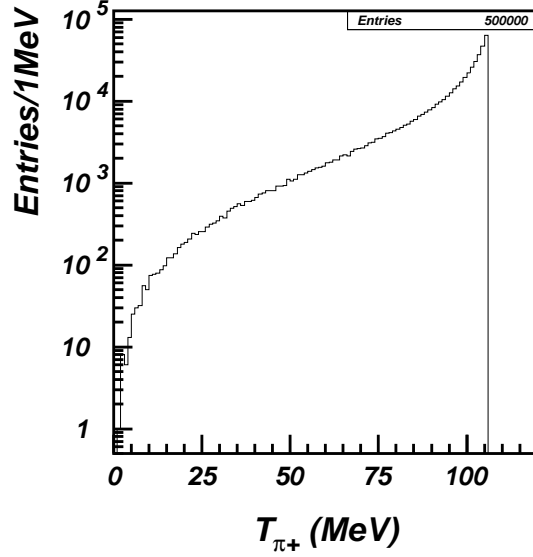


Figure 5.9: Pion energy spectrum from  $K_{\pi 2 \gamma}$  generated by MC, using only the inner Bremsstrahlung process.

events to the number of  $K_{\pi 2}$  peak events, it is necessary to know the branching ratio and the rejection of both the online and offline cuts for each decay. This information was calculated using MC.

About  $2 \times 10^5$   $K_{\pi 2}$  and  $5 \times 10^5$   $K_{\pi 2 \gamma}$  events were generated with MC. Fig. 5.9 shows the  $\pi^+$  kinetic energy spectrum of the  $K_{\pi 2 \gamma}$  events produced. The BR in the whole phase space of the decay ( $0 \text{ MeV} < T_{\pi^+} < 106 \text{ MeV}$ ) can be calculated from this distribution as:

$$BR(K_{\pi 2 \gamma}) = \frac{\int_0^{106} dN}{\int_{55}^{90} dN} \times (2.75 \pm 0.15) \times 10^{-4} = (1.11 \pm 0.06) \times 10^{-3} \quad (5.14)$$

Then the online  $\pi\nu\overline{\nu}(2)$  trigger and the offline cuts were applied to the simulated samples (Table 5.9). From the number of events remaining and the

| Requirement                                    | $K_{\pi 2}$ | $K_{\pi 2\gamma}$ |
|--|-------------|-------------------|
| $K^+$ decays ( $N_{K_{\pi 2(\gamma)}}^{UMC}$ ) | 199992      | 499968            |
| $\pi\nu\overline{\nu}(2)$ trigger              | 20455       | 49355             |
| offline cuts ( $N_{K_{\pi 2(\gamma)}}$ )       | 4950        | 6907              |

Table 5.9: Trigger simulation and offline cuts effect on  $K_{\pi 2}$  and  $K_{\pi 2\gamma}$  simulated samples.

branching ratio of each decay, the ratio of  $K_{\pi 2}$  events in the kinematic peak over the  $K_{\pi 2\gamma}$  events in the  $\pi\nu\overline{\nu}(2)$  region can be determined as :

$$\begin{aligned}
\kappa &= \frac{N_{K_{\pi 2}}}{N_{K_{\pi 2\gamma}}} \times \frac{BR(K_{\pi 2})}{BR(K_{\pi 2\gamma})} \times \frac{N_{K_{\pi 2\gamma}}^{UMC}}{N_{K_{\pi 2}}^{UMC}} \\
&= \frac{4950}{6907} \times \frac{0.2113 \pm 0.0014}{(1.11 \pm 0.06) \times 10^{-3}} \times \frac{499968}{199992} \\
&= 341 \pm 17
\end{aligned} \tag{5.15}$$

The rejection due to the photons from the  $\pi^0$  for both  $K_{\pi 2}$  and  $K_{\pi 2\gamma}$  decay can be expected to be roughly equal. However, due the presence of the extra photon, the total Photon Veto rejection for the  $K_{\pi 2\gamma}$  decay is expected to be higher than for  $K_{\pi 2}$ . The single photon detection inefficiency of the detector has been measured as a function of the energy and angle of the additional photon in [44]. Using these measurements and the energy and angular distribution of the additional photon for the 6907 events which passed all the analysis cuts (Fig. 5.10), the rejection due to the additional photon was measured to be

$$R_{\gamma} = \frac{1}{\epsilon_{\gamma}} = 5.40 \tag{5.16}$$

where  $\epsilon_{\gamma}$  is the total single photon detection inefficiency from the convolu-

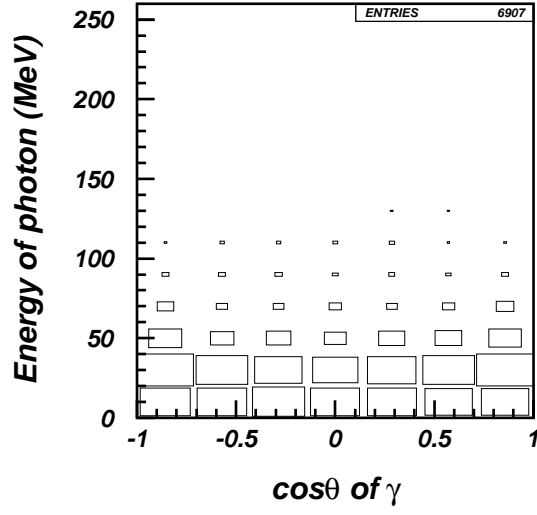


Figure 5.10: Energy vs polar angle of the non- $\pi^0$  photon from the  $K_{\pi 2\gamma}$  MC events that passed all the cuts.

tion of the distribution in Fig. 5.10 and the map in [44].

Using the ratio of  $K_{\pi 2}$  events in the kinematic peak over the  $K_{\pi 2\gamma}$  events in the PNN2BOX from the MC study, and the additional Photon Veto rejection due to the presence of the extra photon in the  $K_{\pi 2\gamma}$  decay, the radiative  $K_{\pi 2}$  background can be measured as

$$N_{K_{\pi 2\gamma}} = 3 \times \frac{N_{K_{\pi 2}}^{data}}{\kappa R_{\gamma}} = 3 \times \frac{27 \pm 5.2}{(341 \pm 17) \cdot 5.4} = 0.044 \pm 0.009 \quad (5.17)$$

where  $N_{K_{\pi 2}}^{data}$  is the number of events in the  $K_{\pi 2}$  kinematic peak which survived all the analysis cuts, used to generate class 1 of Table 5.1.



| CUT     | events |
|---------|--------|
| SETUP   | 1402   |
| KPIGAP  | 41     |
| TGCUT06 | 3      |

Table 5.10: Normalization branch for CEX from data. The cuts mentioned in the text are skipped from the SETUP and the TGCUT06.

## 5.7 Charge Exchange (CEX) background

The Charge Exchange background is expected to come from  $K_L^o \rightarrow \pi^+ e^- \nu_e$  and  $K_L^o \rightarrow \pi^+ \mu^- \nu_\mu$  decays. The DELCO3 cut suppresses the contribution from  $K_S^o$  decays, but a slow  $K_L^o$  can travel away from the CEX position and decay to a lepton that could be missed and a signal-like pion. Such a topology is suppressed by the cut TARGF, which requires that the Kaon and pion clusters are connected.

The normalization branch for this background comes from data, with KPIGAP (a tighter version of  $\overline{TARGF}$ , see appendix A) and all other cuts applied, except for DELCO3, B4EKZ, TGPV, OPSVETO, CCDPUL, CHI567, VERRNG, CHI5MAX and ALLKFIT. These excluded cuts also have rejection against CEX, as they would cut events with prompt  $K^o$  decay, ambiguous decay vertex assignment, or visible  $e^-$  energy in the Target, but they are skipped in order to retain statistics. The final normalization number will be corrected for their rejection ( $R_{excl}$ ). The normalization branch is shown in Table 5.10. SETUP includes PNN2BOX, KCUT, PSCUT06, TDCUT02 and PVCUTPNN2.

Since a pure CEX sample cannot be isolated from data inverting any other cuts apart from TARGF, the effect of this cut on the background and the

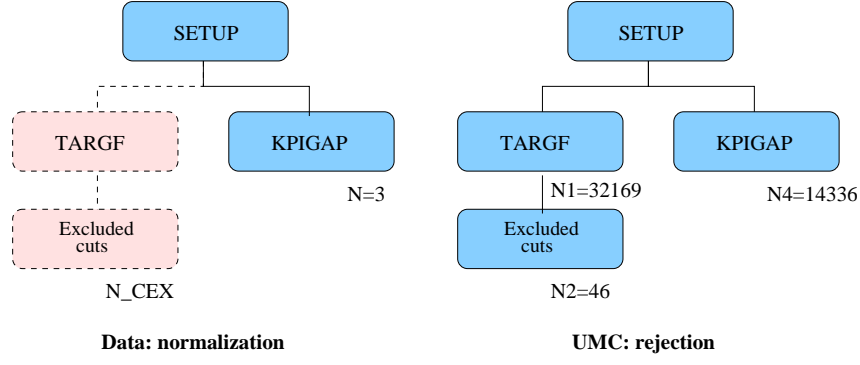


Figure 5.11: The method used to calculate the expected CEX background. The shaded boxes are not accessible in data, since they are the signal region, but they are in MC.

rejection of the cuts excluded in the normalization branch on CEX events was measured with Monte Carlo. About  $3.42 \times 10^8$   $K_L^0 \rightarrow \pi^+ \mu^- \nu_\mu$  events were generated, using the production point and  $K_L^0$  momentum distributions derived from  $K_S^0 \rightarrow \pi^+ \pi^-$  data [38]. The  $K_L^0 \rightarrow \pi^+ e^- \nu_e$  events are already included in the normalization branch, and the cuts used to suppress  $K_L^0 \rightarrow \pi^+ \mu^- \nu_\mu$  are expected to have the same rejection on  $K_L^0 \rightarrow \pi^+ e^- \nu_e$ , therefore it is adequate to use only the muon mode. As shown in Fig. 5.11, the expected CEX background in the signal region is

$$\frac{N_{CEX}}{N} = \frac{N_2}{N_4} \quad (5.18)$$

where  $N$  is the normalization from data and  $N_2$  and  $N_4$  are from MC. But

$$R_{excl} = \frac{N_1}{N_2} \quad (5.19)$$

therefore

| Background             | Events in the 3/3 sample  |
|------------------------|---|
| $K_{\pi 2}$ TG scatter | $0.479 \pm 0.116 (\text{stat.})^{+0.029}_{-0.123} (\text{syst.})$ |
| $K_{\pi 2}$ RS scatter | $0.015 \pm 0.004$   |
| Beam                   | $0.013 \pm 0.014$   |
| Muon                   | $0.0071 \pm 0.0076$   |
| $K_{e4}$               | $0.052 \pm 0.013 (\text{stat.})^{+0.246}_{-0.023} (\text{syst.})$ |
| $K_{\pi 2\gamma}$      | $0.044 \pm 0.009$   |
| CEX                    | $0.018 \pm 0.010 (\text{stat.})^{+0.005}_{-0.003} (\text{syst.})$ |
| <i>TOTAL</i>           | $0.630 \pm 0.119 (\text{stat.})^{+0.248}_{-0.125} (\text{syst.})$ |

Table 5.11: Total background estimation.

$$N_{CEX} = 3 \times N \times \frac{N_1}{N_4} \times \frac{1}{R_{excl}} \quad (5.20)$$

for the whole sample. Therefore,

$$N_{CEX} = 3 \times (3 \pm 1.7) \times \frac{32169}{14336} \times \frac{1}{32169/46} \times 0.62 = 0.018 \pm 0.010 (\text{stat.})^{+0.005}_{-0.003} \quad (5.21)$$

where 0.62 is the acceptance of CHI567, VERRNG, CHI5MAX and ALKFIT, which was taken from data (see chapter 6). The systematic error comes from the variation of the rejection of the excluded cuts with the chosen  $T_{xtg}$  and  $E_{hide}$  threshold. When they vary from  $T_{xtg} < 1., E_{hide} < 1.25$  to  $T_{xtg} < 3., E_{hide} < 2.75$ , the rejection changes from 32169/38 to 32169/58.

## 5.8 Background summary

The total background expected in the signal region based on the 1/3 sample analysis is summarized in Table 5.11

The expected background in the E787 analysis was  $1.216 \pm 0.239$  [39] for comparable  $KB_{live}$ , therefore the current result is about a factor of 2 improvement. Especially the dominant  $K_{\pi 2}$  target scatter background has been drastically reduced, thanks to the upgraded photon veto. The beam background is better understood and consistent with the  $\pi\nu\overline{\nu}(1)$  beam background. Finally the new method developed to estimate the CEX background is more reliable than the one used in E787, which depended only on Monte Carlo.

## 5.9 Outside-the-box study

In order to verify that the bifurcation cuts are uncorrelated, the outside-the-box (OTB) study was performed on the major ( $K_{\pi 2}$  TG scatter) background. The Photon Veto was loosened to its loosest parameters (at 85% acceptance) and the CCDPUL and EPIONK cuts to a threshold of 2 MeV pion energy, and the background study was repeated. The normalization, rejection and number of  $K_{\pi 2}$  TG scatter background events expected in the large signal region for class 2, which has the CCDPUL and EPIONK inverted, are listed in Table 5.12. The expected  $K_{\pi 2\gamma}$  background in this region has to be added to this value, because the  $K_{\pi 2\gamma}$  background level changes as well when the PV is loosened. Substituting the number of  $K_{\pi 2}$  peak events that survive the loose PV  $N_{K_{\pi 2}}^{data} = 182$  in equation 5.17, the expected  $K_{\pi 2\gamma}$  background in the large box is  $0.099 \pm 0.007$ , not scaled to the 3/3 sample. Given that the  $K_{\pi 2\gamma}$  background is increased by only a factor of 2 in the large box, the CEX background, which is less sensitive to the PV tightness since it has no photons in the final state, is expected to contribute even less.

|                  |                   |
|------------------|-------------------|
| Normalization    | 424               |
| Events before PV | 26360             |
| Events after PV  | 183               |
| PV rejection     | $144.0 \pm 10.6$  |
| Background       | $2.965 \pm 0.220$ |

Table 5.12: The quantities used in the calculation of the expected  $K_{\pi 2}$  TG scatter background in the large signal region, for the outside-the-box study. The background value has not been scaled to the 3/3 sample.

Therefore, the expected background in the OTB region is

$$\begin{aligned}
N_{OTB} &= N_{kp2-TGscat}^{large} + N_{kp2g}^{large} - N_{kp2-TGscat}^{small}/3 + N_{kp2g}^{small}/3 = \\
&2.965 + 0.099 - 0.508/3 - 0.044/3 = 2.880 \pm 0.224 \quad (5.22)
\end{aligned}$$

When this region was examined, 3 events were found, which is consistent with the expectation.

# Chapter 6

## Acceptance measurement

### 6.1 $K_{\mu 2}$ based acceptance

The acceptance of the reconstruction and target quality cuts that do not depend on the charged particle being a pion, the beam cuts and the Photon Veto, as well as the trigger acceptance loss due to accidental activity in the detector are measured with  $K_{\mu 2}$  monitors.  $K_{\mu 2}$  decays with momentum in the peak have a clean, well-reconstructed charged track, no photon expected and are kinematically separated from the beam pion and decay-in-flight band(s), therefore they are ideal for measuring the acceptance loss of the cuts that suppress backgrounds with the opposite characteristics, like scattered  $K_{\pi 2}$  and beam backgrounds.

The setup cuts used to clarify the samples for the different measurements are listed in Table 6.1. TRIGGER is the  $K_{\mu 2}(1)$  trigger bit, ICBIT is the I-Counter trigger bit and KM2PBOX selects  $K_{\mu 2}$  momentum ( $226\text{ MeV}/c < p_{tot} < 246\text{ MeV}/c$ ). For the reconstruction cuts acceptance measurement, no

| $K_{\mu 2}$ SETUP | component cuts   |
|-------------------|--|
| $SETUP_{RD}$      | TRIGGER, ICBIT, $t_{IC} - t_{Ck} > 5ns$ ,<br>B4DEDX, UTC, TARGET, UTC_QUAL   |
| $SETUP_{recon}$   | TRIGGER, ICBIT, $t_{IC} - t_{Ck} > 5ns$ ,<br>B4DEDX, CPITRS, CPITAIL, CKTRS, CKTAIL,<br>BWTRS, $A_{RD}$ cuts, $ t_{IC} - t_{RS}  < 5ns$ ,<br>PVCUTPNN2(noBV+BVL) |
| $SETUP_{beam}$    | TRIGGER, ICBIT, $A_{RD}$ cuts, $A_{recon}$ cuts,<br>KM2PBOX, COS3D   |
| $SETUP_{tgqual}$  | $SETUP_{beam}$ , $A_{beam}$ cuts   |
| $SETUP_{PV}$      | $SETUP_{tgqual}$ , $A_{tgqual}$ cuts, stopping layer < 19  |

Table 6.1: Setup cuts used for the  $K_{\mu 2}$  based acceptance measurements. “ $A_{xxx}$  cuts” are the cuts whose acceptance is measured in “xxx” category.

PV is applied in the BV and BVL, because muons can penetrate into those subsystems. By forcing them not to, only events where the muon stopped in the RS would be allowed, which tend to have less steep tracks than the signal, and thus are not reconstructed as efficiently. Therefore the reconstruction efficiency measurement would be biased. For the PV acceptance measurement, on the other hand, the muons are required to stop before RS layer 19, so that they do not penetrate into the BV and BVL. This way, both the online layer 19 veto requirement acceptance loss, and the PV acceptance loss due to accidental activity in those subsystems is correctly included in the PV acceptance.

The acceptances found are shown in Table 6.2 and Table 6.3. DCBIT is the delayed coincidence trigger bit, LHEX is the online RS hextant cut, HEX\_AFTER is the hextant afterburner bit of the L1.2 trigger, PVCUT\_ONL is the BV\*EC\*BVL online veto and LAY\_20\_21 is an implicit cut on unphysical stopping layer output of the online Stopping Counter Finder, included in L1.2.

| CUT                           | events  | acceptance        |
|-------------------------------|---------|-------------------|
| <i>SETUP<sub>RD</sub></i>     | 2683926 |                   |
| RD_TRK                        | 2683926 | 1.000000          |
| TRKTIM                        | 2683768 | 0.999941          |
| <i>A<sub>RD</sub></i>         |         | 0.999941±0.000005 |
| <i>SETUP<sub>recon</sub></i>  | 1540621 |                   |
| RDUTM                         | 1540613 | 0.999995          |
| TARGET                        | 1540613 | 1.000000          |
| <i>A<sub>recon</sub></i>      |         | 0.999995±0.000002 |
| <i>SETUP<sub>tgqual</sub></i> | 1936851 |                   |
| TGCUT                         | 1932067 | 0.997530          |
| B4EKZ                         | 1757036 | 0.909407          |
| TGZFOOL                       | 1735713 | 0.987864          |
| TARGF                         | 1681456 | 0.968741          |
| DTGTTP                        | 1681376 | 0.999952          |
| RTDIF                         | 1664265 | 0.989823          |
| TGKTIM                        | 1648213 | 0.990355          |
| EIC                           | 1603801 | 0.973054          |
| TIC                           | 1603796 | 0.999997          |
| PIGAP                         | 1590248 | 0.991553          |
| TGB4                          | 1515757 | 0.953158          |
| PHIVTX                        | 1472010 | 0.971139          |
| CCDBADFIT                     | 1119041 | 0.760213          |
| CCDPUL                        | 468152  | 0.418351          |
| TIMKF                         | 419835  | 0.896792          |
| NPITG                         | 404708  | 0.963969          |
| VERRNG                        | 377404  | 0.932534          |
| ANGLI                         | 377175  | 0.999393          |
| ALLKFIT                       | 369894  | 0.980696          |
| TPICS                         | 369374  | 0.998594          |
| KIC                           | 369277  | 0.999737          |
| EPIONK                        | 369098  | 0.999515          |
| <i>A<sub>tgqual</sub></i>     |         | 0.190567±0.000282 |

Table 6.2: The  $K_{\mu 2}$  based reconstruction acceptance.



| CUT                         | events  | acceptance        |
|-----------------------------|---------|-------------------|
| <i>SETUP<sub>beam</sub></i> | 3502646 |                   |
| TIMCON                      | 3468568 | 0.990271          |
| TGTCON                      | 3431477 | 0.989307          |
| B4ETCON                     | 3397608 | 0.990130          |
| DCBIT                       | 2971819 | 0.874680          |
| DELCO2                      | 2934548 | 0.987459          |
| DELCO3                      | 2665428 | 0.908293          |
| DELC                        | 2533566 | 0.950529          |
| PSCUT                       | 2402330 | 0.948201          |
| B4DEDX                      | 2389221 | 0.994543          |
| BWTRS                       | 2192141 | 0.917513          |
| B4TRS                       | 2133786 | 0.973380          |
| B4CCD                       | 2104234 | 0.986150          |
| CPITRS                      | 2101029 | 0.998477          |
| CPITAIL                     | 2100066 | 0.999542          |
| CKTRS                       | 2088481 | 0.994484          |
| CKTAIL                      | 2056114 | 0.984502          |
| RVUPV                       | 2020648 | 0.982751          |
| TGGEO                       | 1938032 | 0.959114          |
| TGQUALT                     | 1936851 | 0.999391          |
| <i>A<sub>beam</sub></i>     |         | 0.552968±0.000266 |
| <i>SETUP<sub>PV</sub></i>   | 45255   |                   |
| LHEX                        | 42227   | 0.933090          |
| HEX_AFTER                   | 40647   | 0.962583          |
| PVCUT_ONL                   | 38579   | 0.949123          |
| LAY_20_21                   | 38267   | 0.991913          |
| STLAY                       | 37844   | 0.988946          |
| RSHEX                       | 36499   | 0.964459          |
| PVCUT                       | 35097   | 0.961588          |
| TGPVCUT                     | 34794   | 0.991367          |
| PVCUTPNN2                   | 24154   | 0.694200          |
| <i>A<sub>PV</sub></i>       |         | 0.533731±0.002345 |

Table 6.3: The  $K_{\mu 2}$  based beam and PV acceptance.

The total  $K_{\mu 2}$  based acceptance is

$$A_{K_{\mu 2}} = 0.056240 \pm 0.000262 \quad (6.1)$$

## 6.2 $\pi_{scat}$ based acceptance

The acceptance of the non-fiducial kinematic cuts, the reconstruction cuts that depend on the charged particle being a pion and the TD cuts are measured with scattered beam pion monitors. These events have a well-reconstructed pion track in the UTC and RS, whose stopping counter spans the whole range of the RS, so they can be used to measure the acceptance of the cuts that suppress badly reconstructed and/or scattered events in those subsystems. However, the Target reconstruction is unreliable, due to the small time difference between the “Kaon” and “pion” clusters, therefore this sample is not suitable for the acceptance measurement of the target quality cuts that depend on pion energy deposit.

The setup cuts used to clarify the samples for the different measurements are listed in Table 6.4. The energy deposit in the B4 hodoscope is required to be consistent with a pion ( $b4abm2 < 1.3 MeV$ ) and the target and I-Counter pion time with the RS pion time for all samples. The PV is applied only in the RS, since this is the only PV subsystem whose reconstruction efficiency is measured.

The total  $\pi_{scat}$  based acceptance is

$$A_{\pi_{scat}} = 0.269213 \pm 0.000830(stat.) \pm 0.009086(sys.) \quad (6.2)$$

| $K_{\mu 2}$ SETUP  | component cuts  |
|--------------------|---|
| $SETUP_{bad\_stc}$ | RD_TRK, TRKTIM, STLAY, UTC, RDUTM, TARGET, PDC, ICBIT, $b4abm2 < 1.3 MeV$ , $ t_{\pi} - t_{RS}  < 5ns$ , $ t_{IC} - t_{RS}  < 5ns$ , TARGF, DTGTTP, RTDIF, TGQUALT, TGZFOOL, CKTRS, CKTAIL, PVCUTPNN2(only RS), COS3D, LAYV4, PNN2BOX |
| $SETUP_{kin}$      | $SETUP_{bad\_stc}$ , BAD_STC, TDCUT02   |
| $SETUP_{TD1}$      | $SETUP_{bad\_stc}$ , BAD_STC, RNGMOM, ZFRF, ZUTOUT, LAYER14, UTC_QUAL, EIC  |
| $SETUP_{TD2}$      | $SETUP_{TD1}$ , RSDIDX, PRRF  |

Table 6.4: Setup cuts used for the  $\pi_{scat}$  based acceptance measurements.

### 6.2.1 Kinematic and reconstruction acceptance

In order to account for the poor Target reconstruction of the  $\pi_{scat}$  events, which is a function of the kinematics, the PNN2BOX cut was varied and the kinematic acceptance was measured for 3 different settings: the nominal PNN2BOX, which gives the central value, a small PNN2BOX and a large PNN2BOX, used for the systematic uncertainty. The difference in reconstruction quality for  $\pi_{scat}$  events and  $K_{\pi 2}$  events was evaluated from the resolution of the reconstructed  $\pi$  mass  $m_{\pi} = (ptot^2 - etot^2)/2etot$  of the two samples. The distributions are shown in Fig. 6.1, and have a resolution of 13.8 and 8.4 respectively. The fractional uncertainty in  $\pi_{scat}$  Target track reconstruction is therefore  $\sqrt{13.8^2 - 8.4^2}/140.0 \simeq 7.8\%$ . Since ptot and etot contribute roughly equally to the resolution, their uncertainties are  $7.8\%/\sqrt{2} = 5.5\%$ , and rtot scales approximately linearly with etot, so its uncertainty is also 5.5%. The edges of the nominal  $\pi\nu\bar{\nu}(2)$  kinematic box, then, were varied by 5.5% in order to produce the following small and large boxes

Smallbox :

$$147.7 MeV/c < ptot < 188.1 MeV/c$$

$$12.7 cm < rtot < 26.5 cm$$

$$63.3 MeV < etot < 95.0 MeV$$

Largebox :

$$132.3 MeV/c < ptot < 209.9 MeV/c$$

$$11.3 cm < rtot < 29.5 cm$$

$$56.7 MeV < etot < 106.0 MeV$$

The acceptances found are shown in Table 6.5. The LAYER14 cut has no acceptance loss due to accidentals, because almost no pions with their kinematics in the  $\pi\nu\overline{\nu}(2)$  box reach RS layer 14. The  $\pi_{scat}$  based kinematic acceptance is then

$$A_{kin} = 0.748804 \pm 0.001696(stat.) \pm 0.014055(sys.) \quad (6.3)$$

### 6.2.2 TD acceptance

The  $\pi^+ \rightarrow \mu^+ \rightarrow e^+$  decay chain cuts can also be measured with  $\pi_{scat}$  events. Due to the  $\pi_{scat}$  trigger being looser than the  $\pi\nu\overline{\nu}(1)$  or  $(2)$  one, the sample is expected to be contaminated with pion decay-in-flight and absorption in the

| CUT                   | events | acceptance              |
|-----------------------|--------|-------------------------|
| $SETUP_{kin}^{small}$ | 46437  |                         |
| UTC_QUAL              | 40314  | 0.868144                |
| RNGMOM                | 39717  | 0.985191                |
| RSDEX                 | 37241  | 0.937659                |
| PRRF                  | 35490  | 0.952982                |
| LAYER14               | 35490  | 1.000000                |
| $A_{kin}^{small}$     |        | $0.764261 \pm 0.001970$ |
| $SETUP_{bad\_stc}$    | 153952 |                         |
| BAD_STC               | 153712 | 0.998441                |
| $A_{bad\_stc}$        |        | $0.998441 \pm 0.000101$ |
| $SETUP_{kin}^{nom}$   | 65109  |                         |
| UTC_QUAL              | 56727  | 0.871262                |
| RNGMOM                | 55902  | 0.985457                |
| RSDEX                 | 52021  | 0.930575                |
| PRRF                  | 48830  | 0.938659                |
| LAYER14               | 48830  | 1.000000                |
| $A_{kin}^{nom}$       |        | $0.749973 \pm 0.001697$ |
| $SETUP_{kin}^{large}$ | 81035  |                         |
| UTC_QUAL              | 70716  | 0.872660                |
| RNGMOM                | 69650  | 0.984926                |
| RSDEX                 | 64336  | 0.923704                |
| PRRF                  | 59654  | 0.927226                |
| LAYER14               | 59654  | 1.000000                |
| $A_{kin}^{large}$     |        | $0.736151 \pm 0.001548$ |

Table 6.5: The  $\pi_{scat}$  based kinematic and reconstruction acceptance.

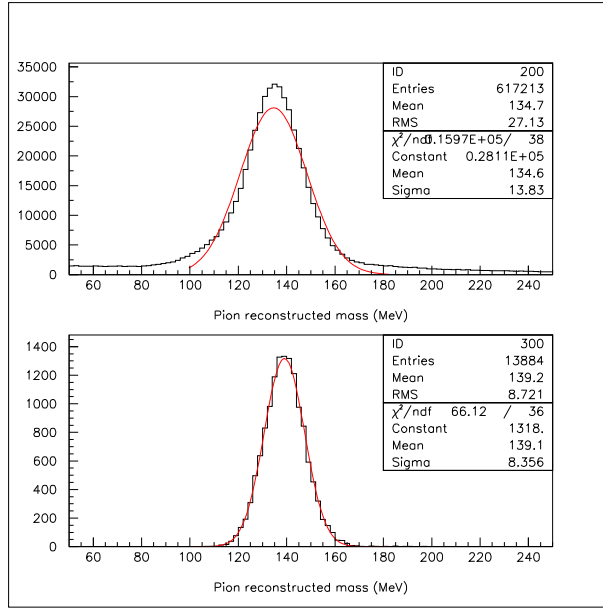


Figure 6.1: The reconstructed pion mass distributions from  $\pi_{scat}$  (top) and  $K_{\pi 2}$  events (bottom).

stopping counter, both of which fake a muon signal, therefore they lower the TD cuts acceptance measured with  $\pi_{scat}$  events. Such effects can be suppressed with the RS reconstruction cuts RSDIDX and PRRF, but these cuts also suppress accidentals, therefore they would cause a higher TD acceptance to be measured. To assess the systematic error due to nuclear interactions and decays in flight (“NIDIF”), two samples were prepared for the TD acceptance measurement, with (“TD2”) and without (“TD1”) the RS reconstruction cuts. The average of the two will be used for the central value and their difference for the systematic uncertainty.

The acceptances found are shown in Table 6.6. L1.1 and L1.2 are the components of the level 1 trigger. The  $\pi_{scat}$  based TD acceptance is then

| CUT                                | events | acceptance        |
|------------------------------------|--------|-------------------|
| <i>SETUP</i> <sub><i>TD1</i></sub> | 115777 |                   |
| FITPI                              | 95578  | 0.825535          |
| RSHEX2                             | 93807  | 0.981471          |
| L1.1                               | 76008  | 0.810259          |
| L1.2                               | 63879  | 0.840425          |
| TDCUT                              | 60057  | 0.940168          |
| EV5                                | 49875  | 0.830461          |
| ELVETO                             | 47775  | 0.957895          |
| TDFOOL                             | 47630  | 0.996965          |
| TDVARNN                            | 40459  | 0.849444          |
| <i>A</i> <sub><i>TD1</i></sub>     |        | 0.349456±0.001401 |
| <i>SETUP</i> <sub><i>TD2</i></sub> | 96309  |                   |
| FITPI                              | 81193  | 0.843047          |
| RSHEX2                             | 79778  | 0.982572          |
| L1.1                               | 65336  | 0.818973          |
| L1.2                               | 55857  | 0.854919          |
| TDCUT                              | 52622  | 0.942084          |
| EV5                                | 43775  | 0.831876          |
| ELVETO                             | 41944  | 0.958172          |
| TDFOOL                             | 41823  | 0.997115          |
| TDVARNN                            | 35595  | 0.851087          |
| <i>A</i> <sub><i>TD2</i></sub>     |        | 0.369592±0.001555 |

Table 6.6: The  $\pi_{scat}$  based TD acceptance.

$$A_{TD} = 0.359524 \pm 0.000752(stat.) \pm 0.010068(sys.) \quad (6.4)$$

### 6.3 $K_{\pi 2}$ based acceptance

The acceptance of the target quality cuts that depend on pion energy deposit and reconstruction quality are measured with  $K_{\pi 2}$  monitor events, in which the decay product is a pion (unlike in  $K_{\mu 2}$  monitors), and its track in the target

| $K_{\mu 2}$ SETUP | component cuts   |
|-------------------|--|
| $SETUP_{UTC}$     | RD_TRK, TRKTIM, STLAY, BAD_STC, TARGET   |
| $SETUP_{ops}$     | TRIGGER, $SETUP_{UTC}$ , UTC, RDUTM, PDC,<br>PSCUT06, KCUTS, TGCUT06 without the ones measured,<br>TDCUT02, KP2BOX |
| $SETUP_{tgkin}$   | $SETUP_{ops}$ , OPSVETO, TGPVCUT   |

Table 6.7: Setup cuts used for the  $K_{\pi 2}$  based acceptance measurements.

is well-reconstructed (unlike  $\pi_{scat}$  monitors). The setup cuts used for this measurement are listed in Table 6.7 and the acceptances found in Table 6.8. The total  $K_{\pi 2}$  based acceptance is

$$A_{K_{\pi 2}} = 0.511091 \pm 0.004118 \quad (6.5)$$

## 6.4 UMC based acceptance

The acceptance of the online trigger and the phase space and solid angle cuts and the acceptance loss due to pion decay-in-flight and pion nuclear interactions (“NIDIF”) are calculated with  $K^+ \rightarrow \pi^+ \nu \bar{\nu}$  Monte Carlo simulated events. About  $10^5$  signal events were generated with NIDIF on and another  $10^5$  with NIDIF off. The trigger  $A_{tr}$  and the phase space  $A_{ps}$  acceptance are measured with the NIDIF-off sample, and then are corrected for NIDIF by comparing with the NIDIF-on sample ( $A_{NIDIF}$ ). The results are shown in Table 6.9, where UFATE, USTMED and USTOP\_HEX are cuts based on UMC truth variables. UFATE requires that the pion stopped without decaying or interacting, this is why it has no acceptance loss for the NIDIF-off case. USTMED requires that the pion stopped in the RS scintillator, and



| CUT            | events  | acceptance              |
|----------------|---------|-------------------------|
| $SETUP_{UTC}$  | 1496580 |                         |
| UTC            | 1412010 | 0.943491                |
| $A_{UTC}$      |         | $0.943491 \pm 0.000189$ |
| $SETUP_{ops}$  | 13139   |                         |
| OPSVETO        | 12817   | 0.975493                |
| $A_{ops}$      |         | $0.975493 \pm 0.001349$ |
| $SETUP_{tgin}$ | 12719   |                         |
| TGDEDX         | 11727   | 0.922006                |
| TGLIKE         | 11333   | 0.966732                |
| EPITG          | 10492   | 0.925792                |
| EPIMAXK        | 10492   | 1.000000                |
| TGEDGE         | 10441   | 0.995139                |
| DRP            | 10414   | 0.997414                |
| CHI567         | 7202    | 0.691569                |
| CHI5MAX        | 7063    | 0.980700                |
| $A_{tgin}$     |         | $0.555311 \pm 0.004406$ |

Table 6.8: The  $K_{\pi 2}$  based acceptance.

USTOP\_HEX that the offline reconstructed stopping counter agrees with the real one. Note that LAYER14 has some phase space acceptance loss, due to the small but non-zero number of  $\pi\nu\bar{\nu}(2)$  events that reach layer 14 of the RS. The SETUP cut is  $ptot < 300 MeV/c$ .

Using the numbers in Table 6.9,

$$\begin{aligned}
A_{tr} &= 0.3291 \pm 0.0015(stat.) \pm 0.0165(sys.) \\
A_{ps} &= 0.4054 \pm 0.0027(stat.) \\
A_{NIDIF} &= \frac{A_{tr}(NIDIFon)}{A_{tr}(NIDIFoff)} \times \frac{A_{ps}(NIDIFon)}{A_{ps}(NIDIFoff)} = \\
&0.7297 \pm 0.0092(stat.) \pm 0.0516(sys.) \tag{6.6}
\end{aligned}$$

The systematic error of 5% comes from the small discrepancies between the

| Cut   | NIDIF ON            | NIDIF OFF           |
|---|---------------------|---------------------|
|   | 99999               | 100000              |
| $T \bullet 2$                                   | 39227               | 41036               |
| $3_{ct} \cdot 4_{ct} \cdot 5_{ct} \cdot 6_{ct}$ | 27575               | 33742               |
| $\pi\nu\bar{\nu}(1)\text{or}(2)$                | 26288               | 32914               |
| $A_{tr}$  | $0.2629 \pm 0.0014$ | $0.3291 \pm 0.0015$ |
| SETUP   | 25793               | 32887               |
| UFATE   | 22688               | 32887               |
| USTMED  | 22517               | 32620               |
| USTOP_HEX                                       | 21743               | 32500               |
| COS3D   | 20870               | 31294               |
| LAYER14   | 20838               | 31282               |
| ZFRF  | 20175               | 30083               |
| ZUTOUT  | 20148               | 30063               |
| PNN2BOX   | 9552                | 13334               |
| $A_{ps}$  | $0.3703 \pm 0.0030$ | $0.4054 \pm 0.0027$ |

Table 6.9: Summary of the acceptances obtained from the Monte Carlo events. The errors are statistical.

kinematic quantities of MC and real events. Since the phase space acceptance exclusively depends on the momentum, range and energy, these kinematic quantities of the Monte Carlo events are adjusted by comparing with those of the real data. The comparison for  $K_{\pi 2}$  events is shown in Table 6.10. The values agree in general, and any differences are accounted for in the systematic error.

Therefore,

$$A_{UMC} = A_{tr} \times A_{ps} \times A_{NIDIF} = 0.0974 \pm 0.0021(stat.) \pm 0.0097(sys.) \quad (6.7)$$

| Quantity                    | Monte Carlo | Real Data                                  |
|-----------------------------|-------------|--|
| Momentum (MeV/c)            | 205.1       | 204.94±0.02±0.02                           |
| Range (cm)                  | 30.4        | 30.254±0.004±0.010                         |
| Energy (MeV)                | 108.5       | 108.77±0.01±0.01                           |
| Momentum Resolution (MeV/c) | 2.34        | 2.29±0.01 <sup>+0.0</sup> <sub>-0.04</sub> |
| Range Resolution (cm)       | 1.02        | 0.901±0.005±0.002                          |
| Energy Resolution (MeV)     | 3.02        | 3.03±0.02±0.02                             |

Table 6.10: Comparison of the  $K_{\pi 2}$  kinematic quantities between Monte Carlo and real data.

## 6.5 $T \cdot 2$ efficiency

The  $T \bullet 2$  efficiency calculated in this section accounts for the acceptance loss due to the geometrical and counter inefficiencies of the T-Counters, which cannot be measured with MC. The geometrical inefficiency is due to the track passing through an azimuthal gap between two adjacent T-Counters. The counter inefficiency occurs if the scintillation light induced by the charged track is not detected by the PMTs. Therefore, the efficiency is

$$\begin{aligned}
\epsilon_{T \bullet 2} &= 1 - \epsilon(\textit{geometrical}) - \epsilon(\textit{counter}) \\
&= 1 - \epsilon(\textit{geometrical}) - e^{-kE},
\end{aligned} \tag{6.8}$$

where  $\epsilon(\textit{geometrical}) = 0.02855$  and  $\epsilon(\textit{counter})$  represent the geometrical and counter inefficiencies respectively,  $k$  is the number of photoelectrons per MeV, and  $E$  is the mean energy deposit in the T-Counters. The value for  $\epsilon(\textit{geometrical})$  was calculated in [38], where  $k$  was also found to be 1.741 p.e./MeV for all sectors apart from two sectors that had hardware problems, for which  $k$  was 1.616 p.e./MeV. These values, that were calculated with  $K_{\pi 2}$

events, will be used for the evaluation of  $A_{T\bullet 2}$  in the  $\pi\nu\overline{\nu}(2)$  region, because  $K_{\pi 2}$  pions are more similar to the  $\pi\nu\overline{\nu}(2)$  signal than  $K_{\mu 2}$  muons.

Using the mean energy deposit in the T-counters as a function of momentum  $E_{dep}(p_\pi)$ , and the momentum distribution  $f(p_\pi)$  for Monte Carlo simulated  $\pi\nu\overline{\nu}$  events in the  $\pi\nu\overline{\nu}(2)$  kinematic box, the inefficiency due to photostatistics is

$$\epsilon(counter) = \frac{\int dp_\pi f(p_\pi) e^{-k E_{dep}(p_\pi)}}{\int dp_\pi f(p_\pi)} = 0.02095 \quad (6.9)$$

which is a weighted average of the values in the good and bad sectors. Then the  $T\bullet 2$  efficiency for  $\pi\nu\overline{\nu}(2)$  is calculated with Eq. (6.8):

$$\epsilon_{T\bullet 2} = 0.9505 \pm 0.0012(stat.) \pm 0.0143(sys.) \quad (6.10)$$

where the 1.5% systematic uncertainty accounts for constraining the charged track in the middle of the T counters in z for the study done in [38]. In order to ensure that the track passed through the T-Counters, the charged track extrapolated by the UTC was required to have z position within  $\pm 20$  cm from the middle of the T-Counters (Z Fiducial Cut). This fiducial requirement increases the  $T\bullet 2$  efficiency because events with the track pointing at the z edge of the T-Counters are removed.

|                         |   |
|-------------------------|---|
| $A_{K_{\mu 2}}$         | $0.056240 \pm 0.000262$   |
| $A_{\pi_{scat}}$        | $0.269213 \pm 0.000830(\text{stat.}) \pm 0.009086(\text{sys.})$ |
| $A_{K_{\pi 2}}$         | $0.511091 \pm 0.004118$   |
| $A_{UMC}$               | $0.0974 \pm 0.0021(\text{stat.}) \pm 0.0097(\text{sys.})$       |
| $A_{tot}$               | $(7.537 \pm 0.179) \times 10^{-4}$                              |
| $\epsilon_{T\bullet 2}$ | $0.9505 \pm 0.0012(\text{stat.}) \pm 0.0143(\text{sys.})$       |
| $f_s$                   | $0.7740 \pm 0.0011$   |
| $KB_{live}$             | $1.77 \times 10^{12}$   |
| $(S.E.S.)^{-1}$         | $1.019 \times 10^{-9}$  |

Table 6.11: The  $\pi\nu\bar{\nu}(2)$  acceptance factors and Single Event Sensitivity.

## 6.6 Acceptance summary and Single Event Sensitivity (S.E.S.)

The total acceptance for the  $\pi\nu\bar{\nu}(2)$  study and the rest of the factors used to calculate the Single Event Sensitivity from equation 4.4:

$$S.E.S. = A_{tot} \times \epsilon_{T\bullet 2} \times f_s \times KB_{live}$$

are summarized in Table 6.11.  $A_{tot}$  is the total acceptance of the online and offline cuts,  $\epsilon_{T\bullet 2}$  is the  $T\bullet 2$  efficiency,  $f_s$  is the fraction of Kaons stopping in the target and  $KB_{live}$  the total number of Kaon decays in the detector during the data taking.

In the absence of background, the S.E.S. is the lowest branching ratio that could be measured by this analysis, which is at the same level with the one in E787's  $\pi\nu\bar{\nu}(2)$  analysis ( $(S.E.S._{E787})^{-1} = 0.687 \times 10^{-9}$ , combined for the 1996 and 1997 data sets).

# Chapter 7

## Conclusion

The study of the 1/3 sample has been completed. The Photon Veto and Target reconstruction quality cuts have been tightened and optimized, in order to suppress the major  $K_{\pi 2}$  Target scatter background, which has been reduced by a factor of 2. As a result, the total expected background level has been shown to be  $0.630 \pm 0.119$  events, about a factor of 2 less than the E787 expectation of  $1.216 \pm 0.239$  events [39]. Therefore, the upgrade of the Photon Veto system of the E787 detector has lived up to expectation.

The other backgrounds are also at an acceptable level and better understood than before, especially the beam background, which now agrees with the  $\pi\nu\bar{\nu}(1)$  beam background taking into account the larger  $\pi\nu\bar{\nu}(2)$  phase space, and the Charge Exchange background, which is measured with a new method that uses also data, in addition to Monte Carlo.

The final acceptance of  $(7.537 \pm 0.179) \times 10^{-4}$  has also been proven to be reasonable, despite the large acceptance loss of some Target quality cuts and the tightened TD cuts, due to the expansion of the kinematic box and the op-

timization of the Photon Veto, among other reasons. Although the beam had double the intensity compared to the E787 running conditions, the acceptance loss due to accidentals did not have a catastrophic effect on the acceptance, which is at the same level of the E787 one  $((13.230 \pm 0.135) \times 10^{-4})$ .

The signal to background ratio for the  $\pi\nu\overline{\nu}(2)$  analysis has been improved to about 1/5, whereas in E787 was about 1/10. A sample with this purity could make a 10% effect on the  $\pi\nu\overline{\nu}$  Branching Ratio, when combined with the  $\pi\nu\overline{\nu}(1)$  result.

# Chapter 8

## Appendix

### A Analysis cuts

#### A.1 PASS1 level

These basic cuts are applied as a pre-selection to all the analysis samples, therefore they are not mentioned in the background studies.

- Trigger Bit (TRBIT)

The event passes the online trigger bit of  $\pi\nu\overline{\nu}$ .

- Data Taking Quality (BAD\_RUN)

Events in runs during which problems on the beam, detector, or electronics occurred are removed.

- Charged Track Reconstruction (RD\_TRK)

The track is reconstructed in the Range Stack.



- Track Time Reconstruction (TRKTIM)

The average time of the track hits in the Range Stack is obtained.

- Consistency between Online and Offline Stopping Counters (STLAY)

The stopping counter that is found by the online Stopping Counter Finder (SCF) should be the same as that found by the offline track finding routine.

- Stopping Counter Performance (BAD\_STC)

Some TD channels had problems recording input signals in specific periods of data taking. These "bad TD channels" were listed during the detector calibration. The charged track should not stop in the counters where the corresponding TDs were unable to record signals properly.

- Track Fitting in UTC (UTC)

The track is successfully reconstructed in the UTC.

- Matching Between UTC and RS Tracks (RDUTM)

The track reconstructed in the UTC should point to the T•2 sector in the RS.

- Target Reconstruction (TARGET)

The target reconstruction is successfully done.

- Momentum in UTC (PDC)

The momentum measured by the UTC should be less than 280 MeV/c.

This requirement removes failures of UTC pattern recognition.

- $\pi^+ \rightarrow \mu^+$  Double-Pulse Fitting (FITPI)

$\pi^+ \rightarrow \mu^+$  double pulses were found by fitting TD pulses in the stopping counter.

- Photon Veto around the Stopping Counter (RSHEX)

No extra hit is allowed in the counter after the stopping counter and the hexants that do not have track hits.

- Sector Crossing Cut (RSHEX2)

No sector crossing is allowed in the stopping layer.

## A.2 PASS2 level

- Crude Photon Veto Cut (PVCUT)

Perform photon veto in the Barrel Veto (BV), End Cap (EC) and Range Stack (RS). Photon hits that are coincident with the charged track time are selected. Events are rejected if the energy sum of these in-time hits in each subsystem is above the threshold. The time windows and energy thresholds are summarized in Table 8.1.

| Subsystem   | Time Window  | Energy Threshold |
|-------------|--------------|------------------|
| Barrel Veto | $\pm 2.0$ ns | 1.5 MeV          |
| End Cap     | $\pm 1.5$ ns | 3.5 MeV          |
| Range Stack | $\pm 1.5$ ns | 3.0 MeV          |

Table 8.1: The time windows and energy thresholds for Barrel Veto, End Cap and Range Stack.

- Target Reconstruction Cut (TGCUT)

This cut consists of the following requirements:

- The Kaon decay vertex is inside the target.

- The time difference between the average time of the kaon fiber hits in the target (target kaon time  $t_k$ ) and the B4 Hodoscope hit time is within 4 ns.
  - The time difference between the average time of the pion fiber hits in the target (target pion time  $t_{pi}$ ) and the I-Counter hit time is within 5 ns.
  - The energy deposit in the I-Counter should be consistent with that of pions.
- Accidentals at Muon Time (TDCUT)  
Search for accidental activity in the RS that is coincident with the second pulse time (muon time) in the stopping counter. Events are rejected if the energy sum of the coincident hits exceeds a threshold.
  - Beam  $dE/dx$  & Double Beam Cut (PSCUT)  
Require that the energy deposit in the B4 Hodoscope is greater than a specific value and no extra beam particle coincident with the track time is recorded.
  - Target Photon Veto Cut (TGPVCUT)  
Require no extra activity other than kaon and pion hits in the target. This cut rejects events with photon activity in the target and events with an extra beam particle in the target.
  - Delayed Coincidence Cut (DELCO2)  
Require that kaons should decay at least 2 ns after entering the target.

Using these cuts, 6 data “SKIMS” (3 for the 1/3 and 3 for the 2/3 sample) are prepared, in order to minimize processing time. Each SKIM is rich in a different background.

- SKIM1 (5 for the 1/3), for  $K_{\pi 2}$ : TGCUT, PSCUT, TDCUT, TGPV-CUT.
- SKIM2 (6 for the 1/3), for  $K_{\mu 2}$ : TGCUT, PSCUT, PVCUT, TGPVCUT, DELCO2.
- SKIM3 (7 for the 1/3), for beam scatters: TGCUT, TDCUT, PVCUT.

### A.3 Kinematic Cuts (KCUT)

#### Fiducial Cuts

- Stopping Layer Requirement (LAYV4)  
Require that the  $\pi^+$  stopping layer is between 5 and 18, which ensures the  $\pi^+$  stops in the Range Stack as requested in the trigger.
- Layer 14 Cut (LAYER14)  
No charged track is allowed to come to rest in the RSSC second layer embedded between RS layers 14 and 15. Events are rejected if the stopping layer is 14 and a prompt RSSC hit is found in the same sector or one sector clockwise of the stopping counter.
- Polar Angle Cut (COS3D)  
Require that the cosine of the polar angle of a charged track ( $\cos \theta$ ) is within  $\pm 0.5$  ( $|\cos \theta| \leq 0.5$ ).

- Stopping Z Position Cut (ZFRF)

Require that the  $\pi^+$  stopping z position in the Range Stack ( $Z_{\pi stop}$ ) is within the fiducial volume. The cut position depends on the stopping layer of the event.

| Stopping Layer | Cut Condition                     |
|----------------|-----------------------------------|
| 11,12          | $-35 \leq Z_{\pi stop} \leq 35cm$ |
| 13             | $-40 \leq Z_{\pi stop} \leq 40cm$ |
| 14             | $-30 \leq Z_{\pi stop} \leq 30cm$ |
| 15,16,17,18    | $-50 \leq Z_{\pi stop} \leq 50cm$ |

Table 8.2: Cut conditions of  $\pi^+$  stopping z position for various stopping layers.

- Fiducial Cut in UTC (ZUTOUT)

The charged track should pass through the UTC fiducial volume. The z position at the UTC outer layer should be within the active region ( $|z| \leq 25cm$ ).

## Track Reconstruction Cuts

- Track Reconstruction in the UTC (UTCQUAL)

Reject events with poor UTC fits in either x-y or z. Events with overlapping tracks are also rejected.

- RS Track Reconstruction and Matching with the UTC Track (PRRF)

This cut rejects events with the charged track scattering in the Range Stack. It consists of the following criteria:

- $\chi^2$  Probability Cut for RS Track Reconstruction (PRRF1)

Reject events if the quality of the Range Stack track fitting in the

x-y plane is poor. The RS track fitting is performed using sector crossing positions, RSSC hit positions, and the energy deposit in the  $\pi^+$  stopping counter.

- Track Matching in RSSC Z Measurements (PRRFZ1)

Reject events if the track reaches the RSSCs and the matching in the r-z plane between the UTC extrapolation and the RSSC hit positions is poor.

- Track Matching in RS Z Measurements (PRRFZ2)

Reject events if the matching in the r-z plane between the UTC extrapolation and the track hit positions derived from end-to-end timing in the RS counters is poor.

### **dE/dx Cut in the Range Stack (RSDEDX)**

- Maximum Energy Deviation in RS (CHIMAX)

Deviations of energy deposits in the individual track counters are examined.

$$\chi_i \equiv \frac{\log E_{exp}^i - \log E_{meas}^i}{\sigma^i} \quad (\text{A.1})$$

where  $E_{meas}^i$  is the measured energy deposit in the  $i$ th track counter and  $E_{exp}^i$  is the energy in the  $i$ th track counter expected from the measured range. Reject events with the absolute value of the largest  $\chi_i$  greater than or equal to 4.

- Confidence Level in RS Energy Measurements (CLRSDEDX)

The confidence level is calculated from the energy deviations in the individual track counters. The cut position is at 0.04.

- Likelihood Cut for RS Energy Measurements (RSLIKE)

A likelihood is constructed from the energy deposits in the track counters. The likelihood value is required to be between 0 and 10.

### $\pi/\mu$ Separation in Range Stack

- Range-Momentum Consistency (RNGMOM)

The deviation of range in the Range Stack ( $\chi_{R-P}$ ) is required to be

$$\chi_{R-P} \equiv \frac{R_{meas} - R_{exp}}{\sigma_R} \leq 2.2$$

where  $R_{exp}$  is the range expected from momentum with the assumption that the charged track is a pion. This cut rejects the muon band.

### Phase Space Cuts

- Expanded (nominal) PNN2 Box (PNN2BOX)

The upper p, E and R limits are expanded from the E787 values, using the deviations from the  $K_{\pi 2}$  peak ( $P_{peak} = 205.1 MeV/c$ ,  $E_{peak} = 108.6 MeV$ ,  $R_{peak} = 30.4 cm$ ). The lower bounds are kept the same as in E787:

$$\begin{aligned} P_{dev} &\equiv \frac{P_{peak} - ptot}{\sigma_P} \geq 2.5 \implies 140 MeV/c \leq ptot \leq 199 MeV/c \\ E_{dev} &\equiv \frac{E_{peak} - etot}{\sigma_E} \geq 2.5 \implies 60 MeV \leq etot \leq 100.5 MeV \\ R_{dev} &\equiv \frac{R_{peak} - rtot}{\sigma_R} \geq 2.75 \implies 12 cm \leq rtot \leq 28 cm \end{aligned}$$

where  $\sigma_P$ ,  $\sigma_E$  and  $\sigma_R$  are the resolutions of the  $K_{\pi 2}$  peak momentum, energy and range respectively .

## A.4 Beam Cuts (PSCUT06)

### Single-Beam Cuts

- dE/dx in B4 Hodoscope (B4DEDX)

Kaon identification is performed by examining the dE/dx in the B4 Hodoscope, which is required to be greater than or equal to 1.85 MeV.

- Kaon Stop Requirement: Delayed Coincidence Cut (DELC)

The target pion time,  $t_\pi$ , is required to be at least 2 ns later than the target kaon time,  $t_K$  ( $t_\pi - t_K \geq 2ns$ ). The cut position is tightened if either target kaon or pion times have a large uncertainty

- $t_\pi - t_K \geq 5ns$  if the discrepancy between the target kaon time and B4 hit time is greater than 1 ns.
- $t_\pi - t_K \geq 6ns$  if the discrepancy between the target pion time and track time is greater than 1.5 ns.
- $t_\pi - t_K \geq 5ns$  if  $t_\pi$  is obtained from the time of the I-Counter hit, not from the target pion fiber hits.
- $t_\pi - t_K \geq 4ns$  if the energy deposit of a kaon in the target is less than or equal to 50 MeV.
- $t_\pi - t_K \geq 3ns$  if there are less than 4 target pion fibers found.
- $t_\pi - t_K \geq 3ns$  if the beam likelihood value is less than 200 (to be explained in the Pathology Cuts section).



- $t_\pi - t_K \geq 4ns$  if the discrepancy between any of the individual kaon fiber times and the average kaon time is greater than 2 ns.
- $t_\pi - t_K \geq 4ns$  if the discrepancy between any of the individual pion fiber times and the average pion time is greater than 3.5 ns.
- Additional Kaon Stop Requirement: Delayed Coincidence Cut (DELCO3)  
Require that kaons should decay at least 3 ns after entering the target.

### Double-Beam Cuts

- Double-Pulse Fitting in B4 Hodoscope (B4CCD)  
Pulses recorded in the B4 CCD are fitted with a double-pulse assumption. Reject events if hit modules have a signature of double pulses, and the average time of the fitted second pulses is within  $\pm 3.5$  ns of the track time. The signature of double pulses is a ratio of the single-pulse fit  $\chi^2$  to the double-pulse fit  $\chi^2$  that is greater than a certain value, and the energy of the fitted second pulse exceeds a threshold.
- Timing in B4 Hodoscope (B4TRS)  
Events are rejected if the average TDC time of hit modules in the B4 Hodoscope is within  $\pm 2.5$  ns of the track time, or the average CCD time of hit modules is within  $\pm 1.5$  ns of the track time when the energy sum is above a threshold.
- Timing in BWPCs (BWTRS)  
Events are rejected if the time of a hit cluster in any Beam Wire Chamber is within  $\pm 4.5$  ns of the track time.

- Timing in Kaon Čerenkov Counter (CKTRS)

Events are rejected if the average TDC or CCD time of hits in the Kaon ČerenkovCounter is within  $\pm 2$  ns of the track time.

- Extra Timing Cut in Kaon Čerenkov Counter (CKTAIL)

The average time of hits in the Kaon Čerenkov Counter, obtained from the trailing edge of the pulses (minus the TDC width), should not be coincident with the track time. The time windows for this cut is dependent on the value of  $t_\pi - t_K$ .

- $t_\pi - t_K < 15ns$ : events are rejected if there are any hits within  $\pm 3$  ns of the track time.
- $15 \leq t_\pi - t_K < 25ns$ : events are rejected if there are any hits within  $\pm 3.5$  ns of the track time.
- $t_\pi - t_K \geq 25ns$ : events are rejected if there are any hits within  $\pm 2$  ns of the track time.

- Timing in Pion Čerenkov Counter (CPITRS)

Events are rejected if the average TDC or CCD time of hits in the Pion Čerenkov Counter is within  $\pm 2$  ns of the track time.

- Extra Timing Cut in Pion Čerenkov Counter (CPITAIL)

The average time of hits in the Pion Čerenkov Counter, obtained from the trailing edge of the pulses (minus the TDC width), should not be coincident with the track time. The event is rejected if there are any hits within  $\pm 2$  ns of the track time.

- Timing in USPV and RV (RVUPV)

Events are rejected if the TDC or CCD time of hit modules in the RV closest to the track time is within  $\pm 4.0$  ns of the track time. If the TDC time of the hit module in the USPV closest to trs is within  $(-3.75, 2.5)$  ns of trs, or the CCD time closest to trs is within  $(-3.5, 2.4)$  ns of trs, the event is also vetoed.

## Pathology Cuts

- Consistency Cut between B4 Hodoscope Analyses (B4ETCON)

Requires a consistency between TDC and CCD, and ADC and CCD values in B4 Hodoscope.

- Double-beam Cut in Target (TGGE0)

Timing information in the I-Counter is used to reject Double Beam background with the following signature:

1. Both particles enter the target from a target edge or an I-Counter
2. the first particle or its decay product deposits a large energy pulse in the I-Counter
3. the first particle enters the target, decaying downstream or decaying very late (i.e., the decay product is not detected).

The second particle is scattered upstream of the beam line and misses some beam counters. Later, by multiple scattering, it enters the target and intersects the hit fibers of the first beam particle. These signatures fool the target reconstruction.

- Target Reconstruction (TGQUALT)

The kaon vertex is reconstructed inside the target.

- Timing Consistency between Target and B4 Hodoscope (TIMCON)

Require the consistency between the target kaon time ( $t_K$ ) and the time of hit in the B4 Hodoscope ( $t_{B4}$ ), and between the target pion time ( $t_\pi$ ) and the track time ( $t_{RS}$ ).

$$|t_K - t_{B4}| \leq 3.0 \text{ ns} \quad \text{and} \quad -4.5 < t_\pi - t_{RS} < 4.0 \text{ ns} \quad (\text{A.2})$$

- Timing Consistency among Target Kaon Fibers (TGTCN)

Require consistency between the average time of the kaon fiber hits and the times of the individual kaon fiber hits in the target.

- Photon Veto in Upstream Photon Veto and Ring Veto (RVUPV)

Reject events with any activity at track time in the Upstream Photon Veto or in the Ring Veto.

## A.5 Target Quality Cuts (TGCUT06)

- Beam Likelihood Cut (B4EKZ)

A likelihood is constructed from the energy deposit in the B4 Hodoscope, the energy sum of the kaon fibers and the  $K^+$  stopping z position. The likelihood value is required to be greater than 10. The cut is tightened if the pion time is given by the I-Counter instead of the target. In this case, the likelihood value is required to be greater than 20.

- Target Fiducial Cut (TGZFOOL)

Require the z position of the kaon decay vertex obtained from the UTC extrapolation to be within the target fiducial volume ( $tgz \geq -5cm$ ). This cut ensures that the kaon decays in the target.

- Energy Cut on Target Pion Fiber (EPITG)

Require that any target pion fiber should have an energy of less than or equal to 3 MeV.

- Energy Cut on Target Pion Fiber near Decay Vertex (EPIMAXK)

Require that the target pion fiber closest to the decay vertex should have an energy of less than 3 MeV.

- Target Gap Cut between Kaon and Pion Fibers (TARGF)

Reject events where the kaon cluster does not touch any pion fiber. The maximum distance allowed is 0.6 cm.

- Matching between Target and UTC (DTGTTP)

Require that the target and UTC tracks are well matched to each other at the target radius. This cut eliminates events in which the UTC track does not intersect the target edge.

- Quality on Target Path Length Calculation (RTDIF)

Require a small uncertainty in the calculation of the pion path length in the target. This is equivalent to the pion path hidden under the kaon fibers, and it is required to be less than 1.5 cm.

- Target Kink (DRP)

The maximum and minimum distance from the center of the target pion

fibers to the center of the circle that is fitted to the track path by the UTC are examined. Reject events if the distribution of the pion fibers is broad, namely

$$\frac{d_{max} - d_{min}}{R_{tg}} > 0.35 \quad (\text{A.3})$$

where  $d_{max}$  and  $d_{min}$  are the maximum and minimum distances, respectively, and  $R_{tg}$  is the range of the track in the target.

- Time Consistency with the B4 (TGKTIM)

The time in each target kaon fiber is required to be consistent with the kaon time in the B4 counter and the track time in the Range Stack.

- I-Counter Energy Cut (EIC)

Require consistency between the measured ( $E_{meas}$ ) and estimated by the pion path length ( $E_{est}$ ) energy deposit in the I-Counter.

$$|E_{meas} - E_{est}| \leq 5 \text{ MeV and } (E_{meas} - E_{est}) \leq 1.75 \text{ MeV} \quad (\text{A.4})$$

- Timing Consistency between Range Stack and I-Counter (TIC)

Require timing consistency between the track time ( $t_{RS}$ ) and I-Counter hit time ( $t_{IC}$ ).

$$|t_{RS} - t_{IC}| \leq 5.0 \text{ ns}$$

- Energy in Target Edge Fibers (TGEDGE)

Reject events with more than 4 MeV energy in any of target edge fibers within  $\pm 5$  ns of the track time.

- Target dE/dx Cut (TGDEDX)

The  $dE/dx$  of pions in the PNN2BOX (140 MeV/c to 195 MeV/c) changes from 3.08 MeV/cm to 2.47 MeV/cm in plastic scintillator. A likelihood function was created by using the total measured momentum (ptot), target range (rtg) and the target energy (etg) of beam pion events. The target range was quantified in 5 momentum bins and 15 target energy bins. For each bin, the mean target range and sigma was stored and a likelihood function was created assuming a Gaussian distribution. This cut rejects events if this likelihood,  $tgdedx\_like \leq 0.05$ .

- Extreme Target Pion Energies (TGENR)

This cut rejects events if the total pion energy in the target is either too large ( $E_{tg} > 28 MeV$ ) or too small ( $E_{tg} < 1 MeV$ ).

- Target Gap between Pion Fibers (PIGAP)

Reject events with a gap between target fibers classified as pion fibers greater than 1.5 cm. This cut is tightened to 1.0 cm when the cosine of the polar angle is negative and the z position of the track in the I-Counter is less than -7 cm.

- Kaon Cluster and Decay Vertex Position Consistency with the B4 and the Pion Fibers (TGB4)

- Consistency between the B4 Hodoscope and Target Hit Positions (DB4)

Reject events with a distance from the xy hit position in the B4 Hodoscope to the nearest target kaon fiber of more than 1.8 cm.

- Extra Consistency Cut between B4 Hodoscope and Target Hit Positions (DB4TIP)

Reject events with a distance from the xy hit position in the B4 Hodoscope to the nearest tip of a kaon cluster of more than 1.8 cm.

- Target Gap Cut among Kaon Fibers (DVXTIP)

Reject events with a distance between the kaon decay vertex and the nearest tip of the kaon cluster of more than 0.7 cm.

- Target Gap between Kaon and Pion Fibers (DVXPI)

Reject events with a distance between the kaon decay vertex and the closest pion fiber of more than 1.5 cm.

- Back-to-back Track Cut in Target (PHIVTX)

Reject events with back-to-back tracks in the target.

- Opposite-side Pion Fibers (OPSVETO)

The energy sum of the target fibers which are on the opposite side of the pion fibers relative to the decay vertex and are coincident with the target pion time (within  $\pm 4.0$  ns), is required to be less than 1 MeV. The cut is tightened to 0.5 MeV when the beam likelihood value is less than 200.

- Target Likelihood Cut (TGLIKE)

Events with extra energy hidden in the pion fibers, either from photons or pion scatters, should be removed.

- A likelihood is constructed from times and energies of the target pion fibers and distances between the UTC extrapolation path and



the target pion fiber hit positions (LIKE). The likelihood should be 3.2 or less.

- Another likelihood is constructed only by the distances between the UTC extrapolated track and the target pion fiber hit positions (LIKE2). This likelihood should be 2.3 or less.

- Time, Energy and Position Cut for Kaon Fibers (TIMKF)

This cut requires that the times of kaon fibers are consistent with the energy and position of the fiber.

- Pion Fiber Number Cut (NPITG)

If the number of pion fibers in the target is less than 1, then the event is rejected.

- CCD Pulse Fits in the Kaon Fibers (ALLKFIT)

This cut requires that all the kaon fibers which have energy more than 3 MeV should have a CCD pulse fit.

- Pion Fiber Time Distribution Width (TPICS)

This cut rejects events for which the standard deviation of the pion time distribution in the target is greater than 4 ns.

- Pion Energy Under a Kaon Fiber Found by SWATHCCD (EPIONK)

If the target reconstruction routine (“SWATHCCD”) has found a pion fiber overlapping a kaon fiber, then the pion fiber is required to have energy less than 1.5 MeV. This cut removes an inconsistency caused by the use of SWATHCCD. SWATHCCD can find pion hits in kaon fibers for  $t_{pi-tk} > 15\text{ns}$ . The cuts on pion fiber energy EPITG and EPIMAXK are

at 3 MeV, whereas the cut on pion energy under a Kaon fiber (CCDPUL, explained later) is at 1.25 MeV. Therefore, if a fiber is classified as both kaon and pion and is not properly fit by the CCDPUL algorithm, then the pion energy cut on these fibers would be 3 MeV.

- Target Fitter Matching with Individual Pion Fibers (CHI567)

A  $\chi^2$ -like quantity is formed based on

- the observed and expected energy in all the fibers which have a hit and are a part of the reconstructed pion track in the target ( $\chi_5^2$ )
- the minimum distance between the track and the corners of every fiber that has no energy but the track is projected to go through it ( $\chi_6^2$ )
- the distance between the track and every fiber that has energy but the track is not projected to go through it ( $\chi_7^2$ )

The cut CHI567 rejects events if the probability of the sum of these three quantities is less than 0.015, where the number of degrees of freedom is  $n_{free} = n_{fib} + 2$ , where  $n_{fib}$  is the number of fibers used in the fit. The details of these target track fitting quantities can be found in Appendix B of [39].

- Target Fitter Matching with Vertex Fiber (VERRNG)

This cut rejects events if the fitted track in the target does not intersect the vertex fiber identified by SWATHCCD. If  $verrng$  is the projected range of the track in the vertex fiber, then this cut removes events for which  $verrng < 0.05cm$ .

- Maximum Contribution to the Target Fitter  $\chi_5^2$  (CHI5MAX)  
If the contribution from any individual fiber to  $\chi_5^2$  is more than 10, then the event is rejected.
- SWATHCCD and UTC Track Fitting Consistency (ANGLI)  
This cut rejects events if the range of the charged track in the target is less than 2cm and the angle between the SWATHCCD reconstructed track and the UTC extrapolated track in the target is greater than 0.01 radian.
- Kaon Time in I-Counter (KIC)  
Events are rejected if target kaon fibers are found near the I-Counter and a hit time in the I-Counter is coincident with the target kaon time.
- Kaon Fiber CCD Pulse Fitting Quality (CCDBADFIT)  
Cut event if both the single and double pulse probability of a fitted fiber with more than the minimum pion energy (1.5MeV) is zero.
- Pion Energy from the CCD Pulse Fitting (CCDPUL)  
Reject events with Kaon fibers whose second pulse found by the CCD fitter has more than 1.25 MeV energy within [-7.5,10.0]ns of pion time.
- Inverted TARGF (KPIGAP)  
For the beam and CEX background studies, a cut is needed to tag events with separated Kaon and pion clusters. A simple inversion of TARGF is not enough, as it allows photon fibers between the clusters, therefore a new cut was devised, that requires  $\overline{TARGF}$  and no photon fibers adjacent to the decay side of the Kaon cluster.

## A.6 $\pi^+ \rightarrow \mu^+ \rightarrow e^+$ Decay Sequence Cuts (TDCUT02)

- Pion Time Consistency (TDTCON)

Events in which an accidental hit plus a sequential hit of a muon track fake the  $\pi^+ \rightarrow \mu^+$  double pulses in the stopping counter should be removed. The first pulse time in the stopping counter, obtained from the TD Double-Pulse Fitting ( $t_{\pi,TD}$ ), is required to be within  $\pm 2.5$  ns of the track time ( $t_{RS}$ ).

$$|t_{\pi,TD} - t_{RS}| \leq 2.5 \text{ ns}$$

This cut is called from within FITPI in PASS2, so their acceptance is measured together.

- $\mu^+ \rightarrow e^+$  Decay Requirement (EV5)

A signature consistent with the  $\mu^+ \rightarrow e^+$  decay is required in and around the stopping counter. A cluster of hits coincident with the third pulse time of the stopping counter is searched for around the stopping counter. Reject events if the cluster has hits in counters on both sides of the stopping counter.

- Cut on Muon Time Accidental (ELVETO)

Events with accidental activities coincident with the second pulse time in the stopping counter should be removed. The accidental hits are searched for in the Range Stack, Barrel Veto, Barrel Veto Liner, and End Cap. Reject events if the energy sum of the coincident hits in any subsystem is above a threshold. The time window and energy threshold for each category are shown in Table 8.3.

| Category                           | t Window (ns) | E Threshold (MeV) |
|------------------------------------|---------------|-------------------|
| Both-end hit category              |               |                   |
| Range Stack (RS)                   | $\pm 3.00$    | 0.20              |
| RS (TD)                            | $\pm 0.25$    | 5.20              |
| Barrel Veto (BV)                   | $\pm 1.25$    | 0.20              |
| Barrel Veto Liner (BVL)            | $\pm 2.75$    | 0.20              |
| Single-end hit category            |               |                   |
| RS single energy, both time        | $\pm 7.00$    | 0.20              |
| RS both energy, single time        | $\pm 4.50$    | 9.40              |
| RS single energy, single time      | $\pm 8.75$    | 6.60              |
| RS no energy, both time            | $\pm 5.00$    | -                 |
| RS (TD) single energy, single time | $\pm 3.00$    | 3.20              |
| BV single energy, both time        | $\pm 3.00$    | 1.60              |
| BV both energy, single time        | $\pm 0.25$    | 0.40              |
| BV single energy, single time      | $\pm 3.00$    | 1.80              |
| BV no energy, both time            | $\pm 5.75$    | -                 |
| BVL both energy, single time       | $\pm 0.75$    | 0.10              |
| BVL single energy, single time     | $\pm 5.00$    | 1.00              |
| BVL no energy, both time           | $\pm 5.50$    | -                 |
| Other category                     |               |                   |
| End Cap (EC)                       | $\pm 0.25$    | 22.00             |

Table 8.3: Time window and energy threshold for each category of the muon time accidental cut for the ELVETO cut.

- Cut on Muon Time Accidental in the Track Counters (TDFOOL)

Events with accidental activities overlapping the track counters and creating the second pulse in the stopping counter should be removed. TD pulses in the two layers prior to the stopping counter are fitted with a double-pulse assumption. Reject events if the fitted pulses are consistent with double pulses and the fitted time of the second pulse is coincident with the second-pulse time in the stopping counter.

- Neural Net  $\pi^+ \rightarrow \mu^+$  Decay Cut (TDVARNN)

Tail fluctuation background as well as muon time background should be removed. A Neural Net function with five variables is constructed from the single-pulse fit  $\chi^2$ 's, the ratios of a single-pulse fit  $\chi^2$  to that of a double-pulse fit, the energy and time of the fitted second pulse, and the difference of the second pulse times between both ends. The cut position on the NN function is set to 0.76.

## **A.7 Photon Veto Cuts (PVCUTPNN2)**

Any activity whose timing is coincident with the track time is searched for in all the subsystems, in order to remove events with photons. The time window and energy threshold for each category are shown in Table 8.4. Hits in the BV, BVL, and RS counter outside the charged track are further categorized into subcategories, depending on whether the counter has hits in both ends or only in single end. Time windows for the "single-end hit categories" are widened.

| Category                      | t window (ns) | E threshold (MeV) |
|-------------------------------|---------------|-------------------|
| Both-end hit category         |               |                   |
| Barrel Veto (BV)              | $\pm 7.95$    | 0.20              |
| Barrel Veto Liner (BVL)       | $\pm 7.55$    | 0.30              |
| Range Stack (RS)              | $\pm 4.30$    | 0.30              |
| Single-end hit category       |               |                   |
| BV single energy, single time | $\pm 8.50$    | 1.60              |
| BV single energy, both time   | $\pm 1.50$    | 1.40              |
| BV both energy, single time   | $\pm 15.95$   | 1.00              |
| BVL both energy, single time  | $\pm 11.80$   | 8.19              |
| RS single energy, single time | $\pm 1.22$    | 3.40              |
| RS single energy, both time   | $\pm 1.35$    | 0.00              |
| RS no energy, both time       | $\pm 5.00$    | 0.40              |
| RS both energy, single time   | $\pm 0.70$    | 5.20              |
| Other category                |               |                   |
| End Cap (EC)                  | $\pm 6.15$    | 0.40              |
| EC inner ring (EC1)           | $\pm 4.64$    | 0.20              |
| EC second pulse (EC2)         | $\pm 4.07$    | 10.60             |
| Target (TG)                   | $\pm 2.40$    | 2.00              |
| I-Counter (IC)                | $\pm 3.25$    | 5.00              |
| V-Counter (VC)                | $\pm 4.15$    | 6.80              |
| Collar (CO)                   | $\pm 2.95$    | 0.60              |
| Microcollar (MC)              | $\pm 3.90$    | 3.00              |
| BV early loose veto (BV1)     | $(-30., 0.)$  | 30.               |
| Active Degrader (AD)          | $\pm 5.0$     | 0.60              |

Table 8.4: Time window and energy threshold for each category of the Photon Veto Cuts.

## B The $\pi\nu\overline{\nu}(2)$ Photon Veto

### B.1 Choosing the cuts

The Photon Veto rejection in the  $\pi\nu\overline{\nu}(2)$  region was extensively studied. Since the BVL TD signals were not used before, the PV subsystems' parameters had to be re-optimized, taking the extra hits added by the BVL TDs into account. The goal was to maximize the background rejection, while retaining a reasonable signal acceptance. To search for the best set of parameters for the 19 main PV subsystems (all apart from the BV1 and AD), the same optimization process as in the  $\pi\nu\overline{\nu}(1)$  analysis was used ([44]). Appropriate rejection ( $K_{\pi 2}$ ) and acceptance ( $K_{\mu 2}$ ) samples were prepared. Given an initial set of parameters (time offsets, time windows and energy thresholds for all the subsystems), the reference rejection and acceptance were measured. Then the parameters of one subsystem at a time were changed by given step sizes, and the rejection and acceptance were remeasured. A new set of parameters was chosen if it improved both the rejection and acceptance (best choice), or either of them without decreasing the other. The process was iterated, until no further improvement could be found. A schematic of the optimization process is shown in Fig. 8.1. Due to the large size of the parameter space (3×19 free parameters), care was taken to avoid falling in a local minimum. Repeating this process for 9 different “goal acceptances”, the optimal set of parameters was found for each of these acceptances, that produced the best rejection-acceptance profile.

Two new PV cut categories were added in the  $\pi\nu\overline{\nu}(2)$  analysis, which were not optimized with the previously mentioned procedure:



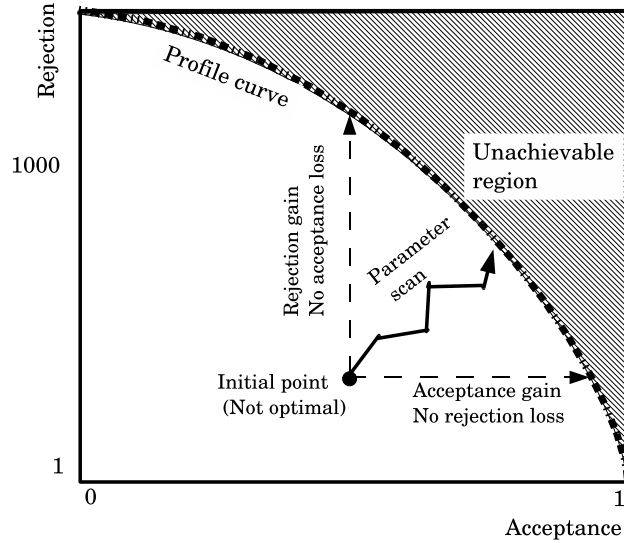


Figure 8.1: Schematic of the PV optimization process.

- Additional early BV (BV1): It was observed that for a wide time range (around 30 ns) before the prompt peak in the BV at RS time, there were very high energy hits in the  $K_{\pi 2}$  sample, but not in the  $K_{\mu 2}$  one. These were most likely due to early accidentals, that blinded the BV TDCs, so that they could not register the photon hits in time with the decay. Since the ADC gates are pretty wide ( $\sim 50$  ns), the energy of both the accidental and the photon hit was measured, therefore these blinded BV modules had unusually high energy. Such events were vetoed with an additional BV cut at 30 MeV.
- Active Degrader (AD): To use the AD as a Photon Veto detector, care had to be taken not to veto on beam activity at Kaon time. The study and optimization of this detector is described in appendix C.

Due to the lack of statistics in the 12 rejection classes of  $K_{\pi 2}$  TG-scattered

events defined in Table 5.1, the optimization was done in the  $K_{\pi 2}$  peak. The result in the  $K_{\pi 2}$  peak, broken down to each subsystem contribution, is shown in Fig. 8.2. Then the same PV was applied to the 12 TG-scatter classes, and the profiles of Fig. 8.3-Fig. ?? were obtained. The values at 60% acceptance were chosen, a tighter choice than the cut used in  $\pi\nu\overline{\nu}(1)$ , based on the expected background for every set of parameters.

## B.2 Limits of the Photon Veto rejection

There are several factors that cause photon detection inefficiency: lack of radiation length and dead material in the detector, sampling fluctuations, photonuclear interactions and masking of photon hits due to earlier accidentals (“veto blindness”).

The weak photon detection areas that existed in the barrel of the E787 detector, seem to have been drastically improved with the addition of the BVL, as shown in Fig. 8.8. Nonetheless, some polar angle dependence of the PV power of the detector still exists due to dead material of the UTC endplate, and causes position dependent inefficiencies. The area close to the beam is also still more inefficient than the barrel region.

Sampling fluctuations depend on the photon energy. The detection efficiency increases with increased energy and larger detector modules. However, the latter requirement competes with the effect of veto blindness: the larger the PV element, the more probability there is for accidental energy deposits, that can render the TDCs unable to register following hits. This inefficiency has been partly compensated by the addition of TDs, that provide the infor-

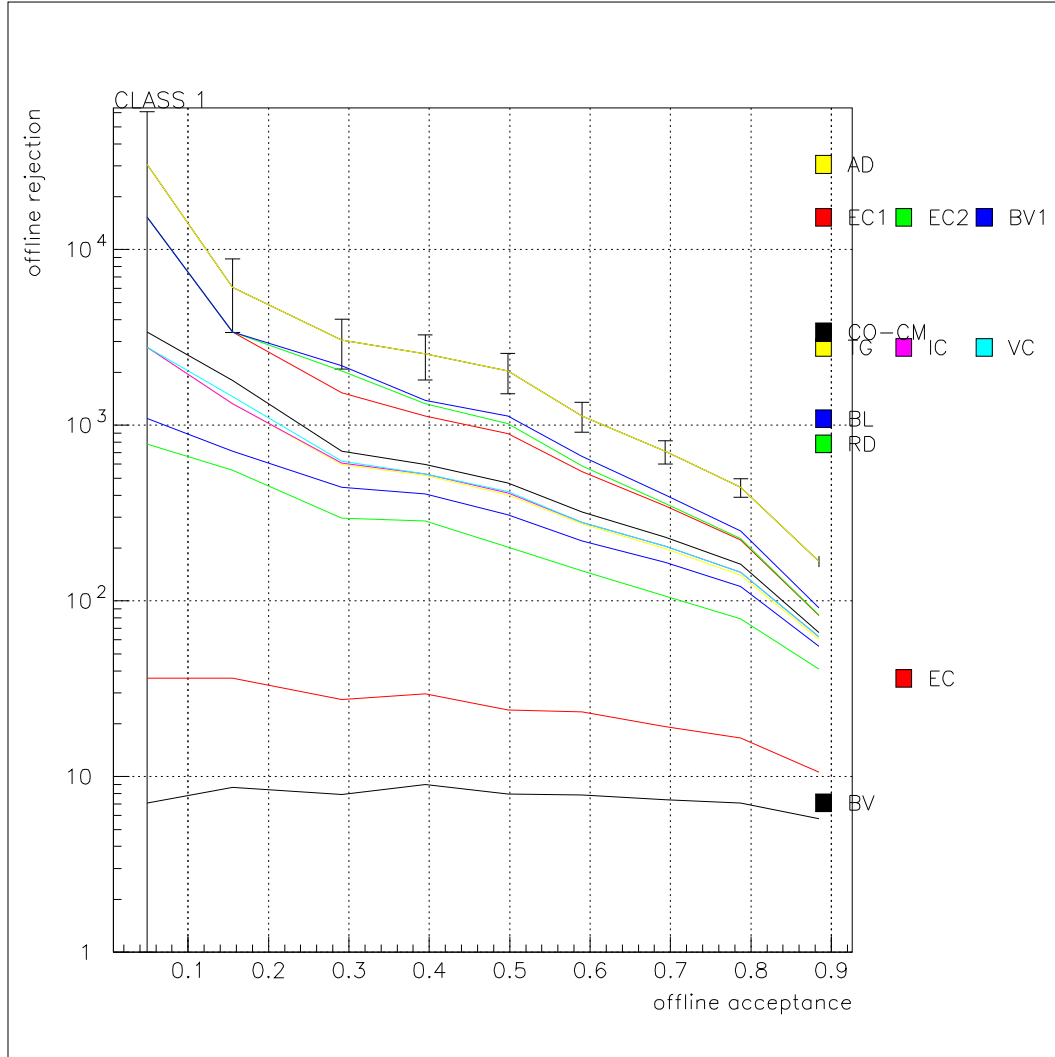


Figure 8.2: Offline rejection vs acceptance profile for the  $K_{\pi 2}$  peak, with each subsystem contribution.

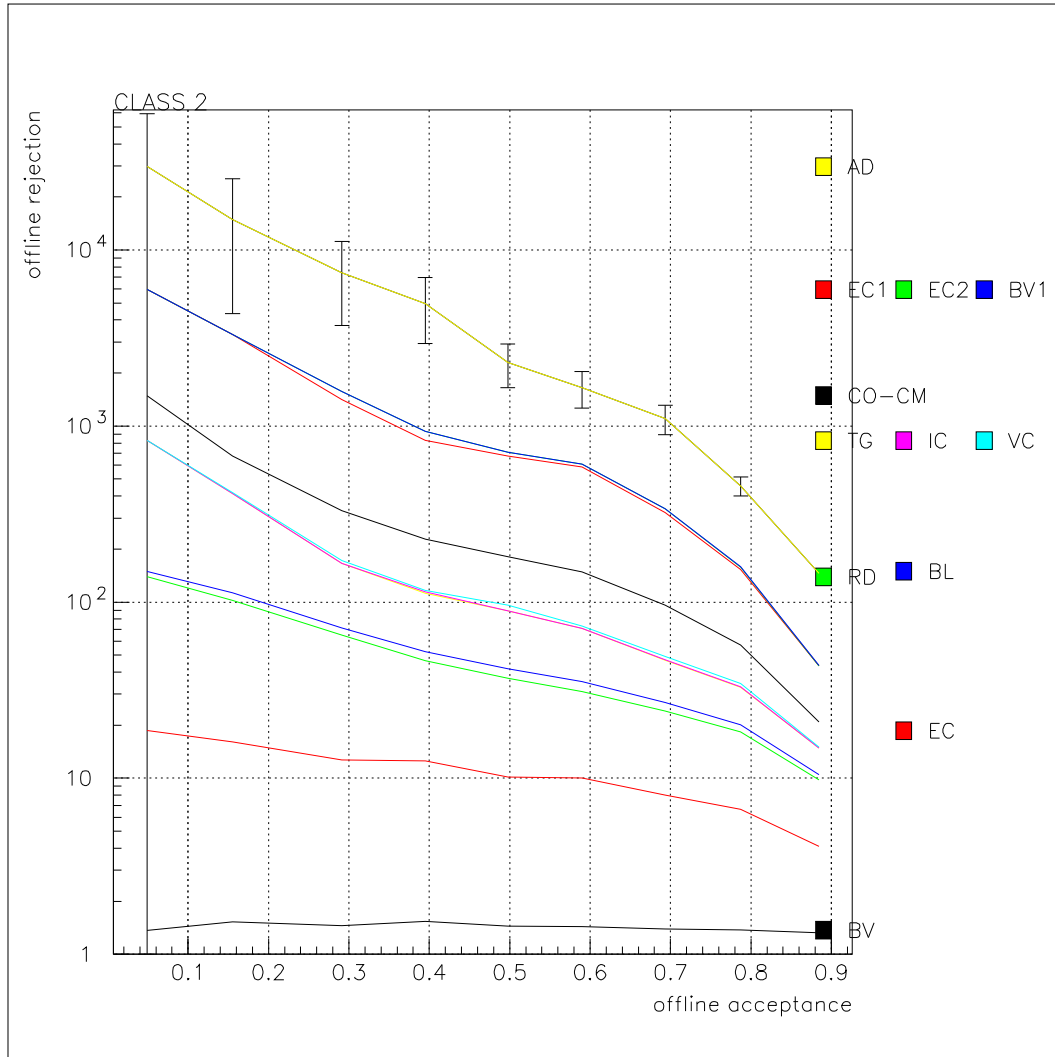


Figure 8.3: Offline rejection vs acceptance profile for the CLASS 2, with each subsystem contribution.

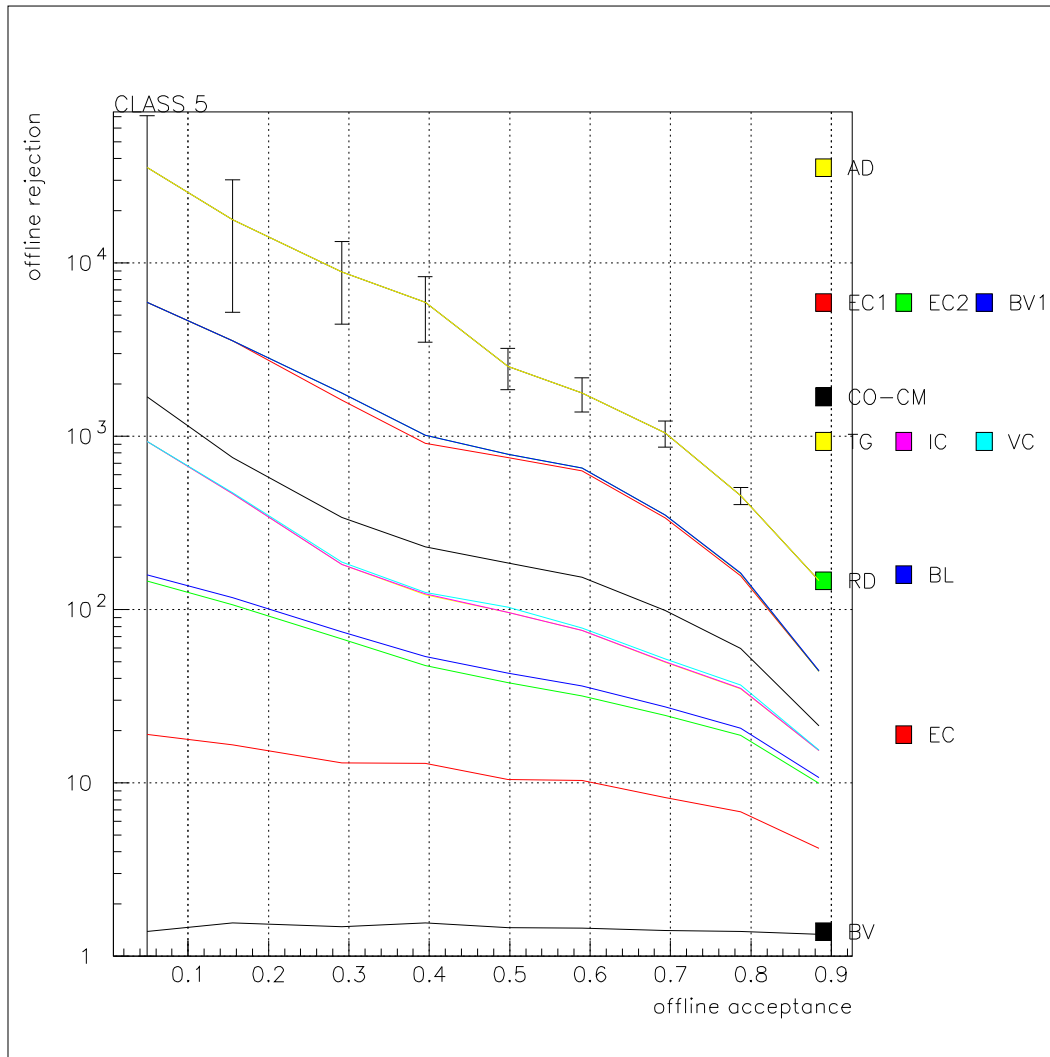


Figure 8.4: Offline rejection vs acceptance profile for the CLASS 5, with each subsystem contribution.

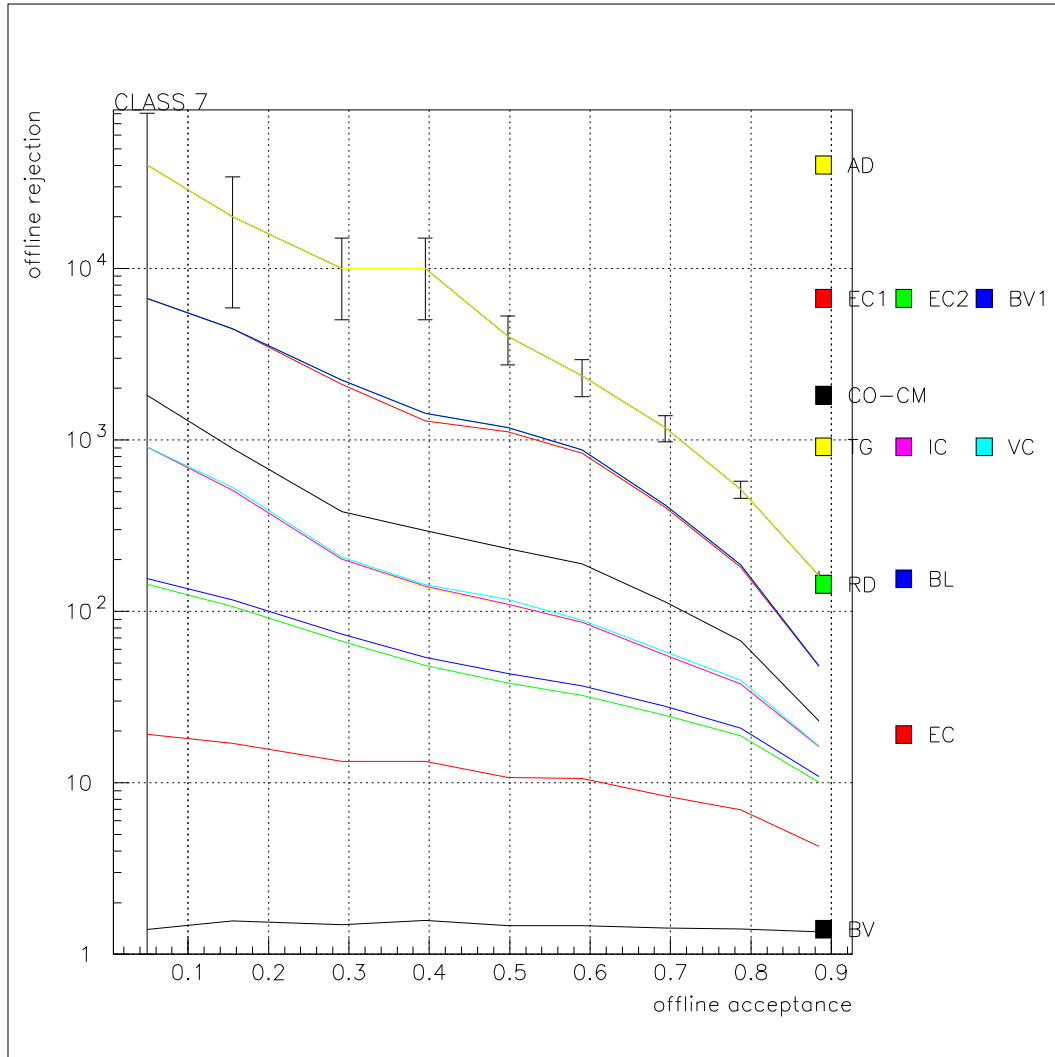


Figure 8.5: Offline rejection vs acceptance profile for the CLASS 7, with each subsystem contribution.

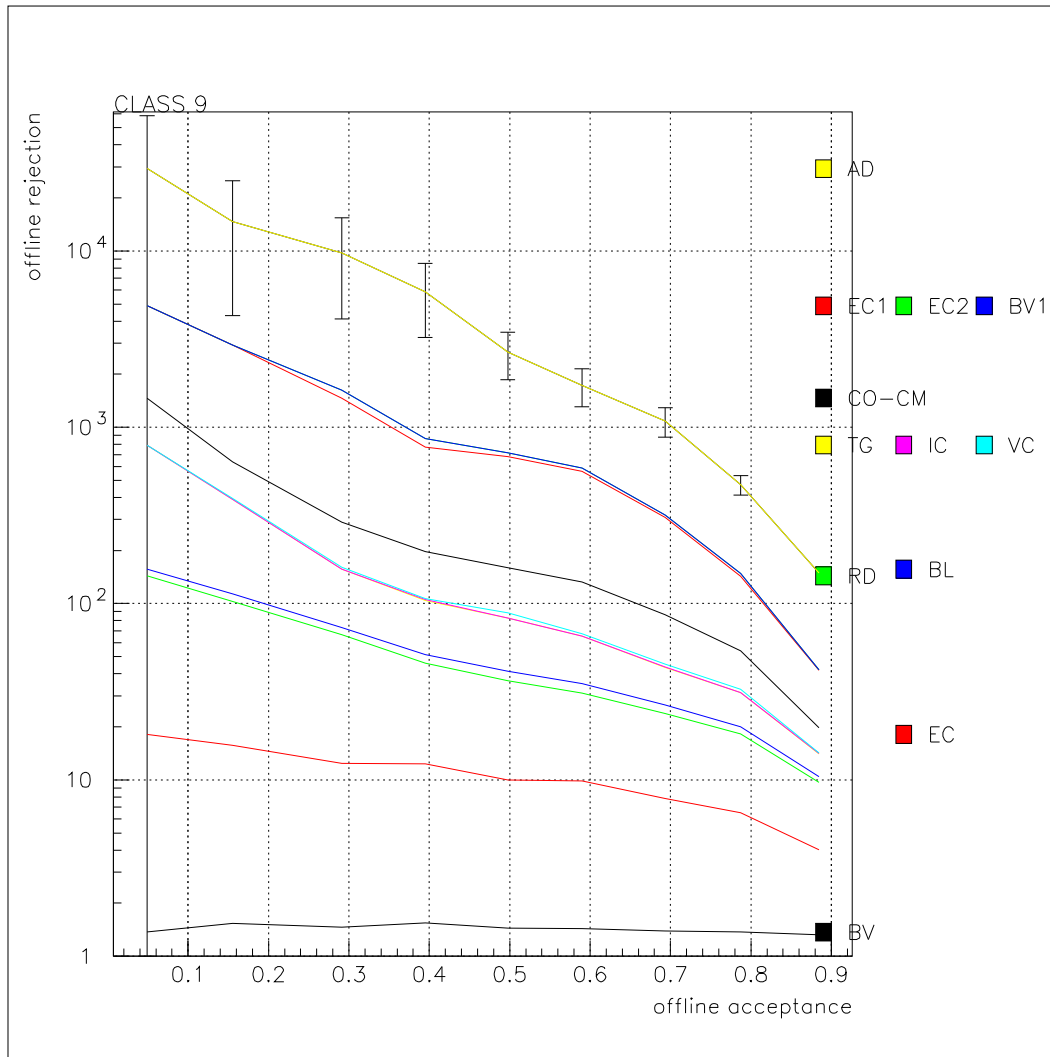


Figure 8.6: Offline rejection vs acceptance profile for the CLASS 9, with each subsystem contribution.

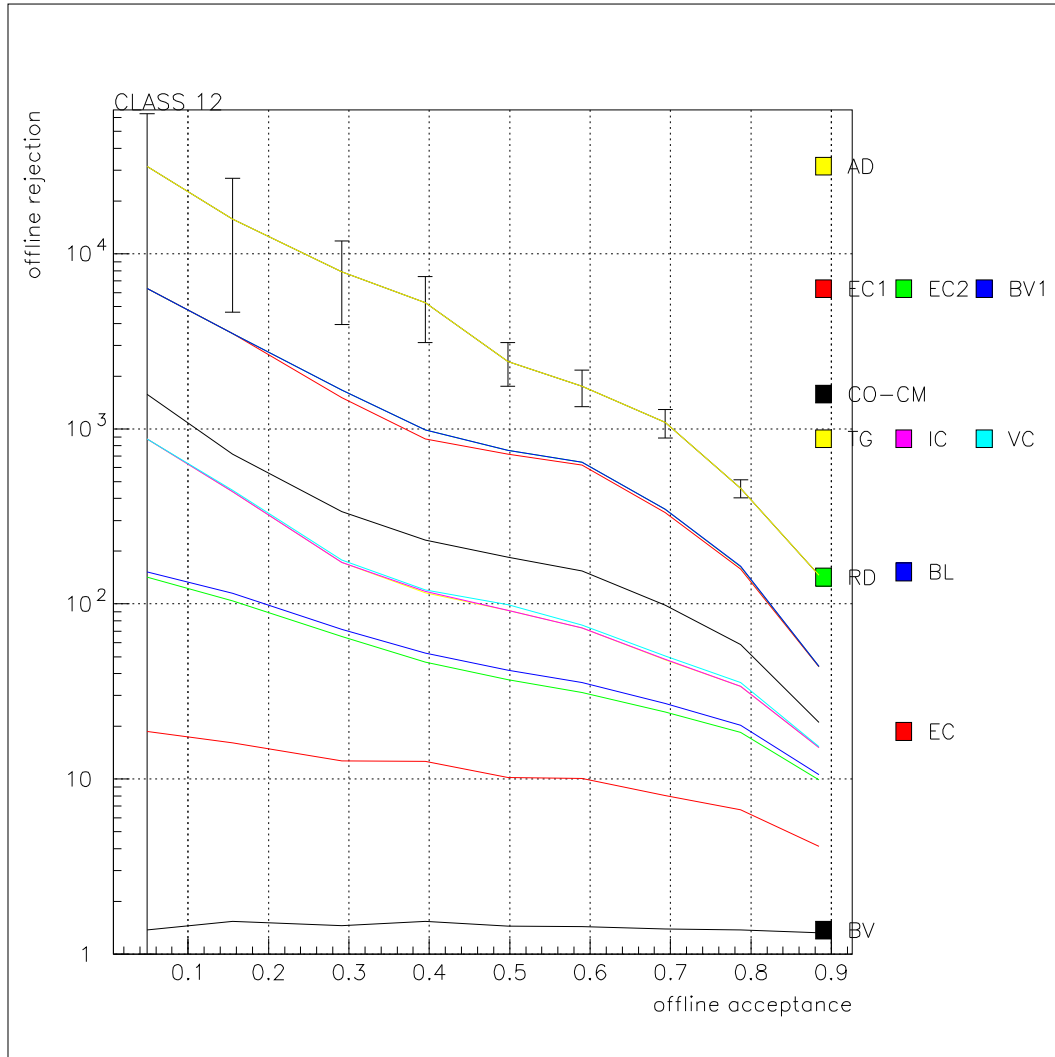


Figure 8.7: Offline rejection vs acceptance profile for CLASS 12, with each subsystem contribution.



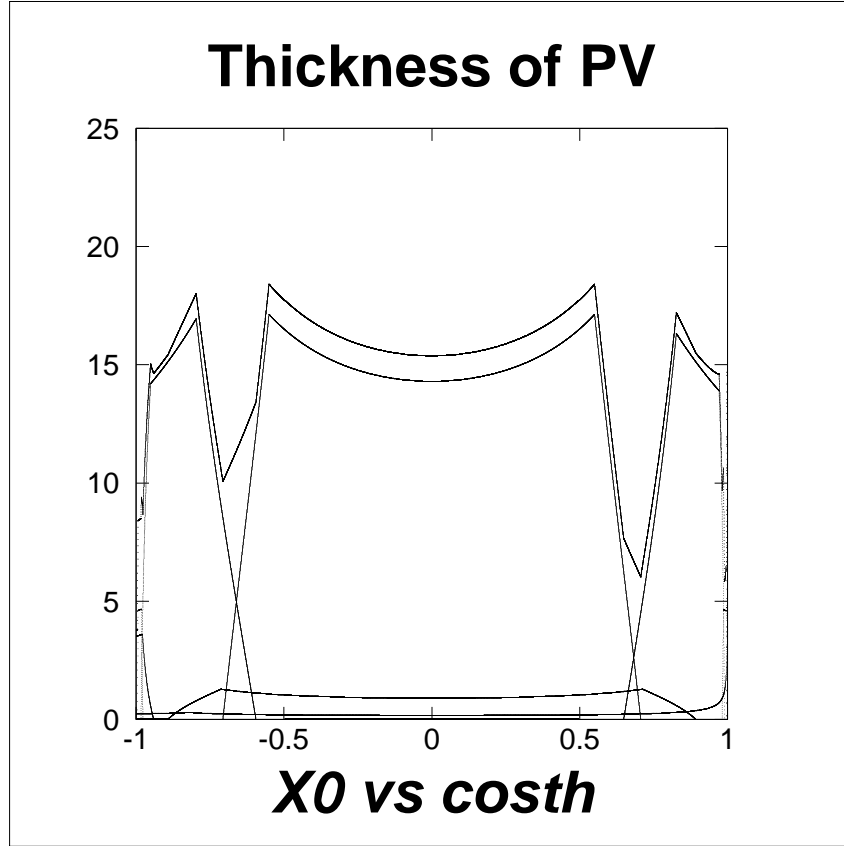


Figure 8.8: Radiation length of the material of the E949 detector as a function of polar angle. The higher curve is after the addition of the BVL, which adds crucial radiation lengths in the weak region around 45 degrees.

mation to distinguish between multiple hits, and the BV1 cut, that exploits the fact that the accidental hits will deposit their energy in the ADC gate, in addition to the photon energy.

Finally photonuclear interactions can cause photon hits later than the nominal veto time, therefore their energy deposit can go undetected. This mechanism cannot even be reliably simulated, unlike the electromagnetic processes, and limits the photon detection ability of the detector.

## C The Active Degrader

The Active Degrader (AD), described in section 3.3.1, has not been used in the PNN1 analysis, but is essential for PNN2, given the expected photon angular distribution from target-scattered  $K_{\pi 2}$  events ([41]). Its performance was extensively studied, and its function as Photon Veto was optimized as described in this section.

In the following, “energies” are in arbitrary units. In order to find the energy in MeV, the Kaon and pion energy peaks from simulation ([45]) were used and compared with the ones from data. For the ADCs, the value of 6.49 units/MeV was obtained from pions, and 6.22 units/MeV from Kaons ([46]). For the CCDs, the value of 8.30 units/MeV was found from Kaons. Therefore a calibration constant of 6.34 ADC units/MeV (the average of the Kaon and pion results) can be used to translate the ADC energy plots to MeV, and 8.30 CCD units/MeV for the CCD.

Beam particle track extrapolation was done to find which AD sectors are expected to be transversed by the incoming K, and thus have some energy deposit associated with the beam. The possibility of excluding these sectors for PV purposes was investigated. The incoming xy point was found by extrapolating the line defined by the hit points in BWC1 and BWC2 to the upstream face of the AD. The outgoing point was the one given by the B4 hit coordinates. Every sector between these 2 points was assigned to the K path. This algorithm has the flaw that it does not take into account the transverse uncertainty to the entering K point caused by multiple scattering in the Inactive Degrader, which is exacerbated by the geometry of the AD: since the

beam is centered where all the sectors meet, a small perturbation in the path causes more/other sectors than expected to be hit.

The samples used in this study are:

- Acceptance sample:  $K_{\mu 2}$  decays from  $K_{\mu 2}$  monitors, where no photon or beam activity is expected.
- Rejection sample 1:  $K_{\pi 2}$  peak events from SKIM5, with a loose PV cut.
- Rejection sample 2:  $K_{\pi 2}$  TG-scatter events identified by special target reconstruction software ([47]). These events (“kinks”) have failed the normal target reconstruction (“SWATHCCD”), therefore they were not included in any background study and there is no danger in examining the ones in the PNN2 kinematic box. This sample is expected to be rich in TG scatters.

## C.1 Timing peaks in the AD

In fig.8.9-8.12, the time distributions of hits in the AD are shown for the acceptance and the rejection samples. All the histograms are normalized to the number of events and have no energy threshold imposed. As can be seen in fig. 8.9, which is for sectors on the K path, the behavior of the three samples is effectively the same in terms of K activity: in the time distributions with respect to Kaon time (tk), an on-time peak is obvious, and the ones with respect to decay (pion) time (tpi), show a decay lifetime shape. Fig. 8.10 shows the same distributions for sectors off the K path. In the time distributions with respect to tpi, a strong photon peak is present for the rejection samples only.

A decay lifetime shape for the same samples is present in the time distributions with respect to tk. Fig. 8.11 and fig. 8.12 show the same for the CCDs. In addition to the photon peak in fig. 8.10 and 8.12, some K activity remnants in time with tk are present, that are the same for all samples. These are due to the inefficiencies in extrapolating the K path mentioned earlier.

The photon time distributions for  $K_{\pi_2}$ peak events and kinks are compared in fig. 8.13, where it can be seen that there is more photon activity in the AD for kinks. Comparing the number of events in the 3 bins of the photon peak for  $K_{\pi_2}$ peak and kinks, there is an approximate 72% more activity in the kink sample measured by the TDCs and 60% by the CCDs.

Time closest to tk/tpi vs total energy distributions for the same samples are shown in fig. 8.14 (fig. 8.15 for CCDs) and energy distributions for the two timing peaks in fig. 8.16 (fig. 8.17 for CCDs). The K energy peak in time with tk is prominent for all samples, whereas most of the energy in time with tpi is at zero for the acceptance sample, and near zero with long high-energy tails for the rejection ones, as expected for showering photons.

## C.2 Applying the cut

Based on the time and energy distributions in the AD, different ways to apply a PV cut were investigated. The main idea is to add the energy deposited either in whole sectors (for ADCs) or individual hits (for CCDs) and veto events based on this sum. For the ADCs, the different schemes are using sectors

- (a) with at least one TDC hit out of time with tk ( $>5\text{ns}$ ) and in time with tpi ( $-2\text{ns}$  to  $8\text{ns}$ )

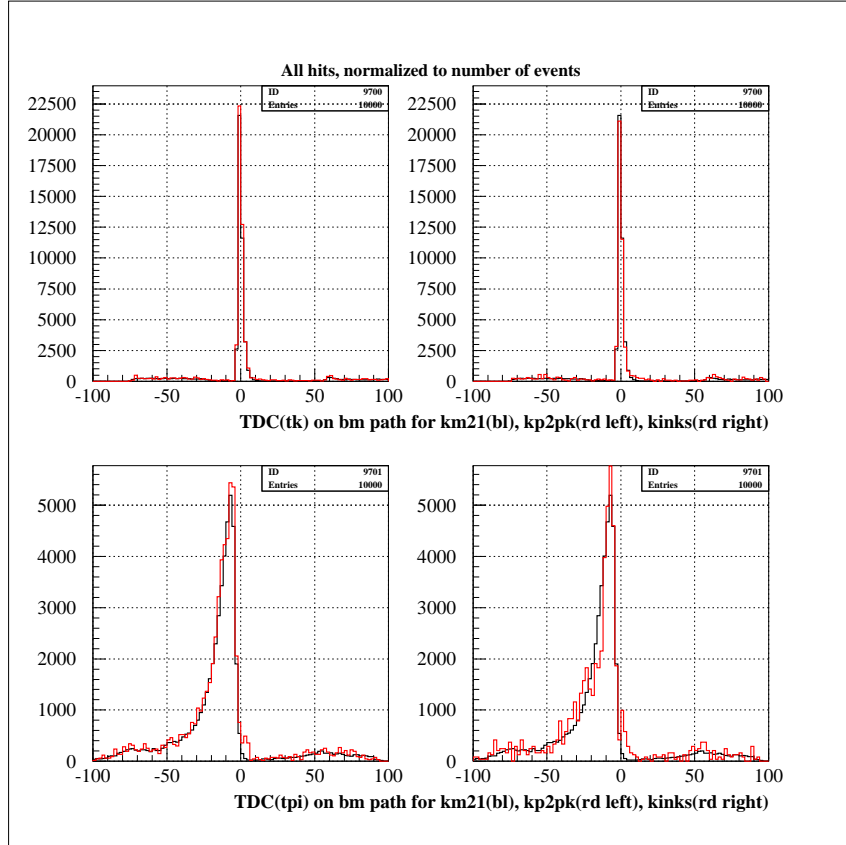


Figure 8.9: Time distributions (in ns) of the AD TDC hits with respect to tk (top row) and tpi (bottom row) for sectors on the incoming Kaon path. Black histograms are for the acceptance sample and red for the two rejection samples ( $K_{\pi 2}$  peak on the left and kinks on the right). The units on the vertical axis are arbitrary.

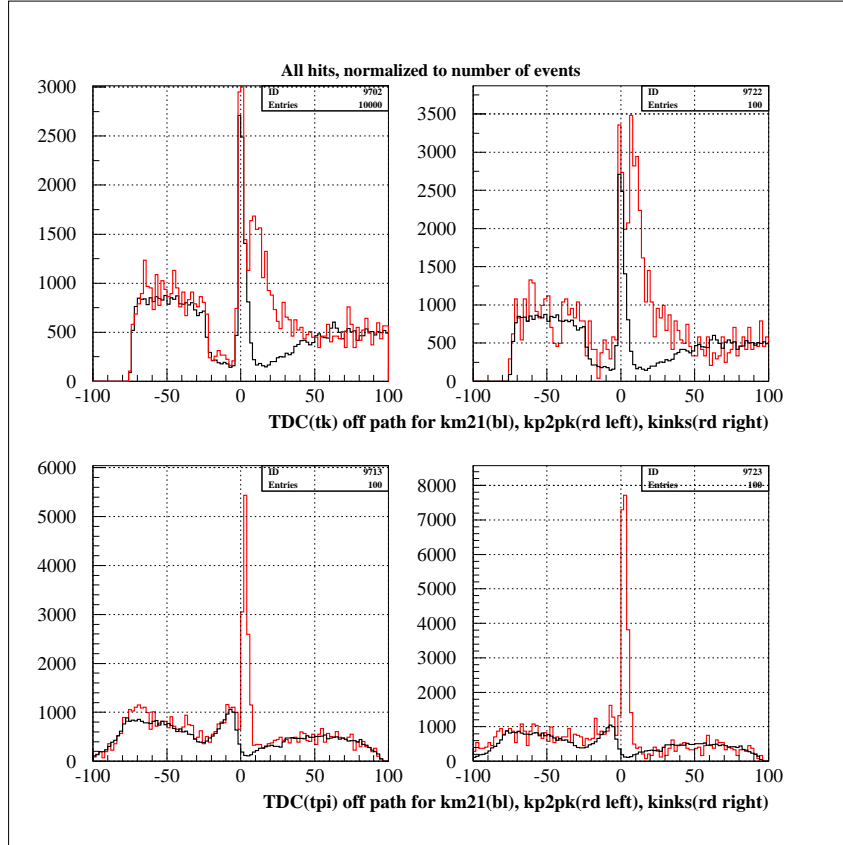


Figure 8.10: Time distributions (in ns) of the AD TDC hits with respect to tk (top row) and tpi (bottom row) for sectors off the incoming Kaon path. Black histograms are for the acceptance sample and red for the two rejection samples ( $K_{\pi 2}$  peak on the left and kinks on the right). The units on the vertical axis are arbitrary.

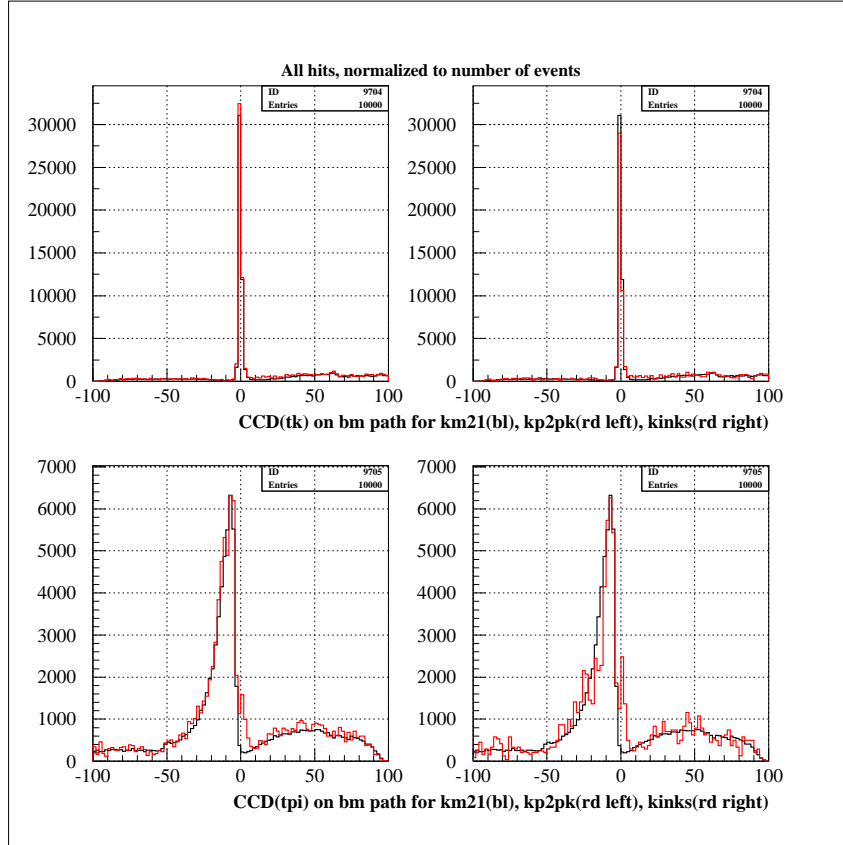


Figure 8.11: Time distributions (in ns) of the AD CCD hits with respect to tk (top row) and tpi (bottom row) for sectors on the incoming Kaon path. Black histograms are for the acceptance sample and red for the two rejection samples ( $K_{\pi_2}$  peak on the left and kinks on the right). The units on the vertical axis are arbitrary.



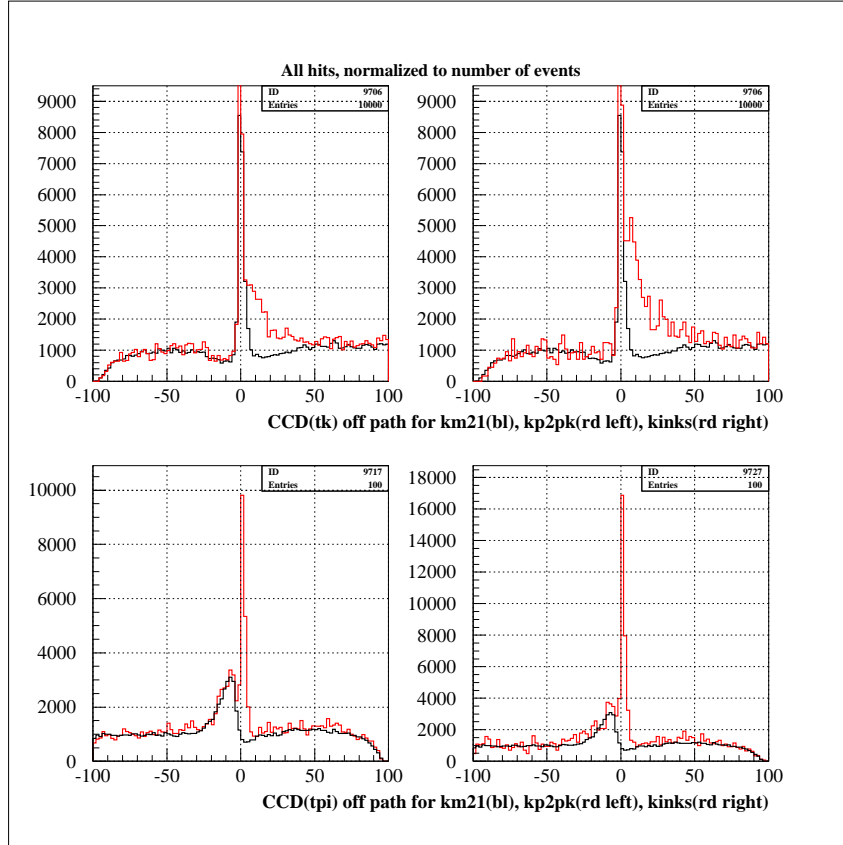


Figure 8.12: Time distributions (in ns) of the AD CCD hits with respect to tk (top row) and tpi (bottom row) for sectors off the incoming Kaon path. Black histograms are for the acceptance sample and red for the two rejection samples ( $K_{\pi_2}$ peak on the left and kinks on the right). The units on the vertical axis are arbitrary.

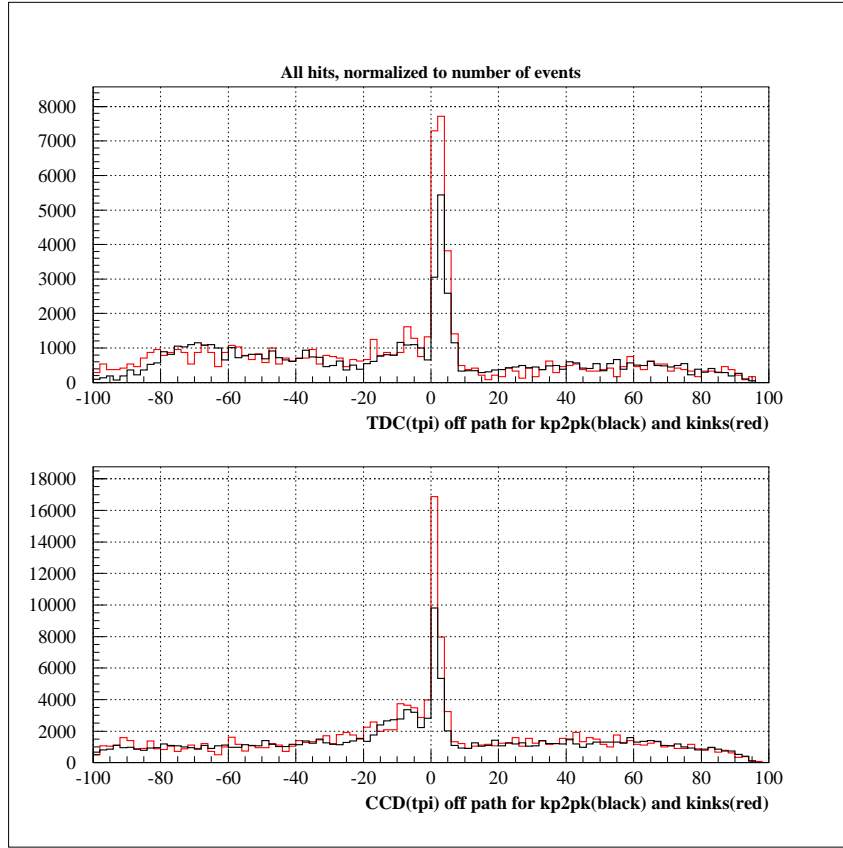


Figure 8.13: Time distributions (in ns) with respect to tpi for sectors off the incoming Kaon path, from TDCs (top) and CCDs (bottom). Black histograms are for  $K_{\pi 2}$ peak and red for kinks. The units on the vertical axis are arbitrary.

- (b) same with (a) and no TDC hit at tk ( $\pm 5$ ns)
- (c) same with (a) and the sector is also out of the K path
- (d) same with (b) and the sector is also out of the K path.

For the CCDs, hits are used that are either

- (a) in time with tpi (-2ns,8ns) and out of time with tk ( $> 5$ ns)
- (b) same with (a) and in sectors out of the K path

The results, in the form of acceptance\*rejection vs energy threshold, are shown in fig. 8.18 for the  $K_{\pi_2}$  peak and in fig. 8.19 for the kinks. For both the rejection samples, cutting on the sum of CCD “energy” at 5., irrespective of the sector the hit belongs to, seems to be the favorable case. Therefore no sector exclusion, or double-pulse fitting is necessary to mask out beam Kaon activity. The time window for this scheme was also optimized. The rejection, acceptance and rejection\*acceptance for the lowest energy threshold for all cases are summarized in table 8.5. From the values in this table, it can be seen that the AD could have added some rejection power to the  $\pi\nu\overline{p}(1)$  Photon Veto if it was used.

|                        | ADC (a),(b)    | ADC (c),(d)    | CCD (a)        | CCD (b)        |
|------------------------|----------------|----------------|----------------|----------------|
| acc                    | $0.96\pm0.001$ | $0.98\pm0.001$ | $0.94\pm0.002$ | $0.97\pm0.001$ |
| $K_{\pi_2}\text{peak}$ |                |                |                |                |
| rej                    | $1.64\pm0.03$  | $1.54\pm0.03$  | $1.79\pm0.04$  | $1.59\pm0.03$  |
| acc*rej                | $1.58\pm0.03$  | $1.51\pm0.02$  | $1.68\pm0.04$  | $1.54\pm0.03$  |
| Kinks                  |                |                |                |                |
| rej                    | $1.81\pm0.07$  | $1.73\pm0.05$  | $1.95\pm0.08$  | $1.80\pm0.07$  |
| acc*rej                | $1.76\pm0.08$  | $1.70\pm0.06$  | $1.86\pm0.08$  | $1.76\pm0.08$  |

Table 8.5: Rejection, acceptance and rej\*acc of different implementations of the AD photon veto for both rejection samples, for the lowest threshold (5.).

### C.3 Correlation with the EC

The rej\*acc of the AD as a function of the energy threshold was also measured for tighter setup PV cuts and for only the upstream EC inner ring (EC1) PV tightened, in order to investigate the correlation of this subsystem with the rest of the PV. Photon activity in the AD is expected to be heavily correlated with activity in the EC1, as shown in [48]. The plots for the  $K_{\pi_2}\text{peak}$  for

|                | loose PV         | tight PV         | tight EC1        |
|----------------|------------------|------------------|------------------|
| acc            | $0.94 \pm 0.002$ | $0.95 \pm 0.002$ | $0.95 \pm 0.002$ |
| rej            | $1.79 \pm 0.04$  | $1.95 \pm 0.14$  | $1.69 \pm 0.07$  |
| acc*rej        | $1.68 \pm 0.04$  | $1.86 \pm 0.13$  | $1.60 \pm 0.06$  |
| EC1 parameters |                  |                  |                  |
| t half-window  | 2 ns             | 5.15 ns          | 5.15 ns          |
| E threshold    | 2 MeV            | 0.2 MeV          | 0.2 MeV          |

Table 8.6: Rejection, acceptance and rej\*acc of CCD(a) for the lowest energy threshold for different setup PV cut, for  $K_{\pi 2}$  peak. The EC1 veto parameters for every setting are also given.

tight PV are shown in fig. 8.20, and for only the EC1 PV tightened in fig. 8.21. The results for the optimal case (CCD (a), at the lowest threshold) are summarized in table 8.6. The rej\*acc is a bit higher for the tight PV sample, which means that the AD still has rejection power after the rest of the PV has been applied, and a bit smaller for the only-EC1-tightened one, as expected for these two correlated subsystems. In both cases, it follows the same trend as a function of energy threshold as the loose-PV case.

Further evidence of the AD-EC correlation is shown in fig. 8.22-8.23. The fraction of events with zero energy deposit in EC1 and the remaining upstream EC is shown as a function of the AD energy deposit for the three samples. The rest of the PV has not been applied on the rejection samples, to increase statistics. From the  $K_{\mu 2}$  sample, it can be seen that the accidentals rate is at about 10% for both pieces of the upstream EC. The rejection samples show a clear correlation between both upstream EC parts and the AD. The rise of these plots in both the rejection samples for very high AD energies, is due to the online PV that has already cut events with high energy deposits in the EC. These events most likely also leave the highest energy in the AD.

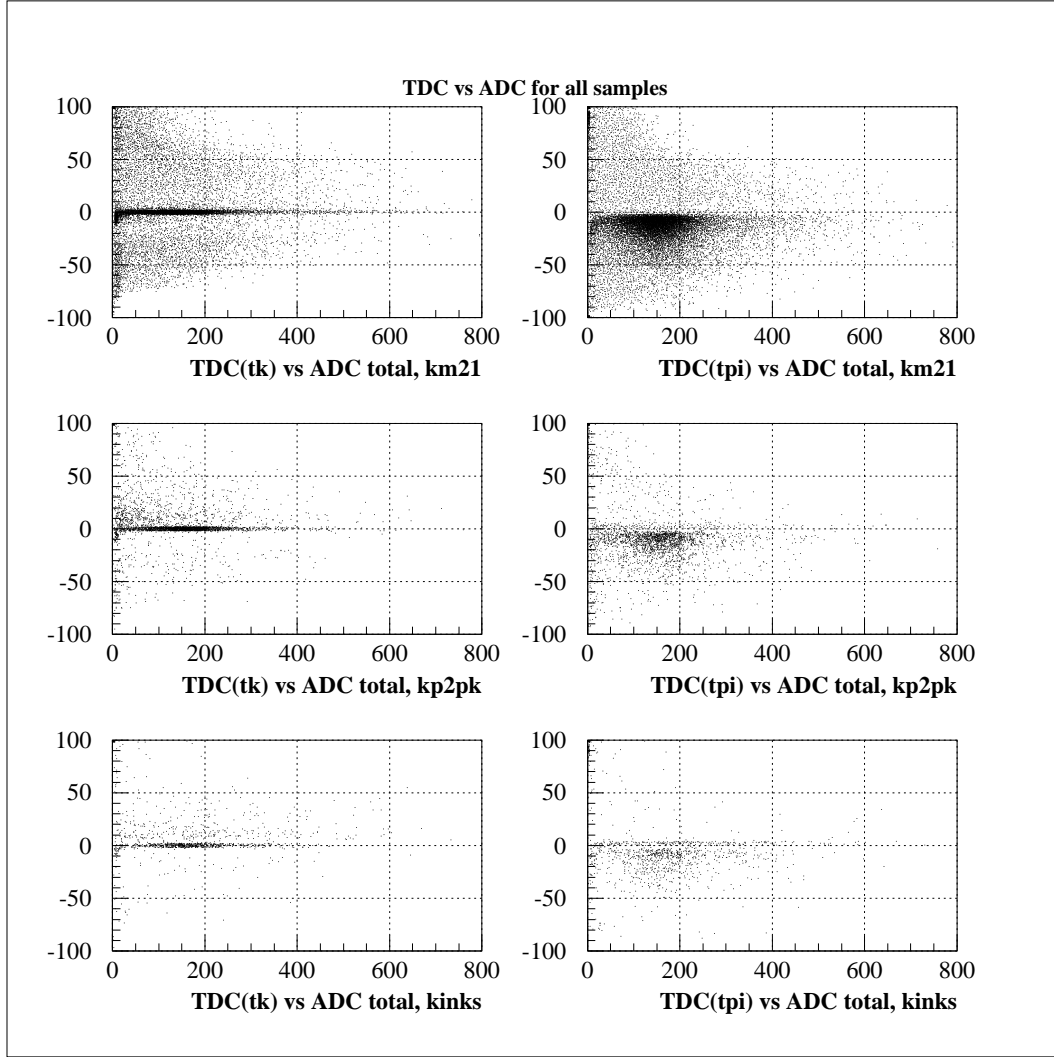


Figure 8.14: Time distributions (in ns) with respect to tk (left) and tpi (right) of the TDC hit closest to tk or tpi, vs total ADC energy for  $K_{\mu 2}$  (top),  $K_{\pi 2}$  peak (middle) and kinks (bottom).

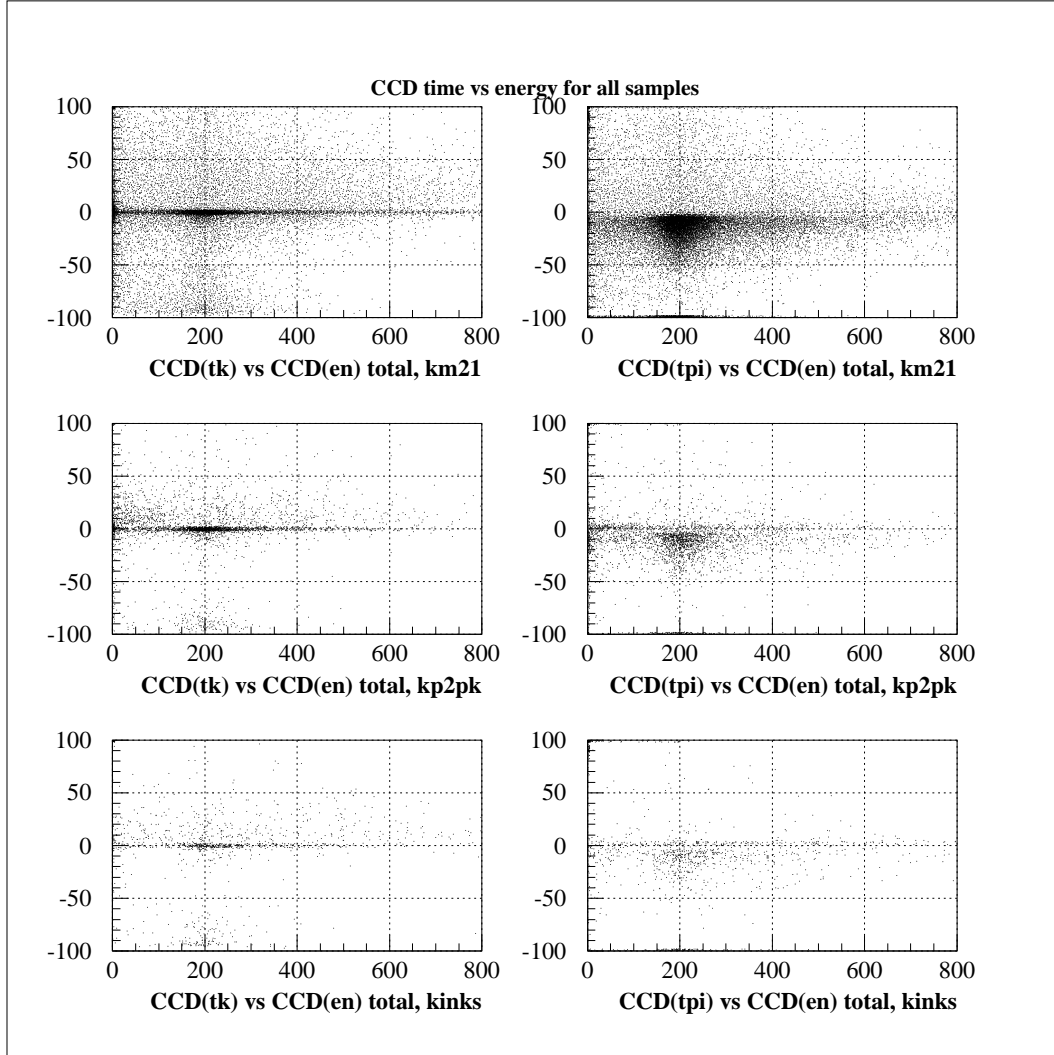


Figure 8.15: Time distributions (in ns) with respect to tk (left) and tpi (right) of the CCD hit closest to tk or tpi, vs total CCD energy for  $K_{\mu 2}$  (top),  $K_{\pi 2}$  peak (middle) and kinks (bottom).

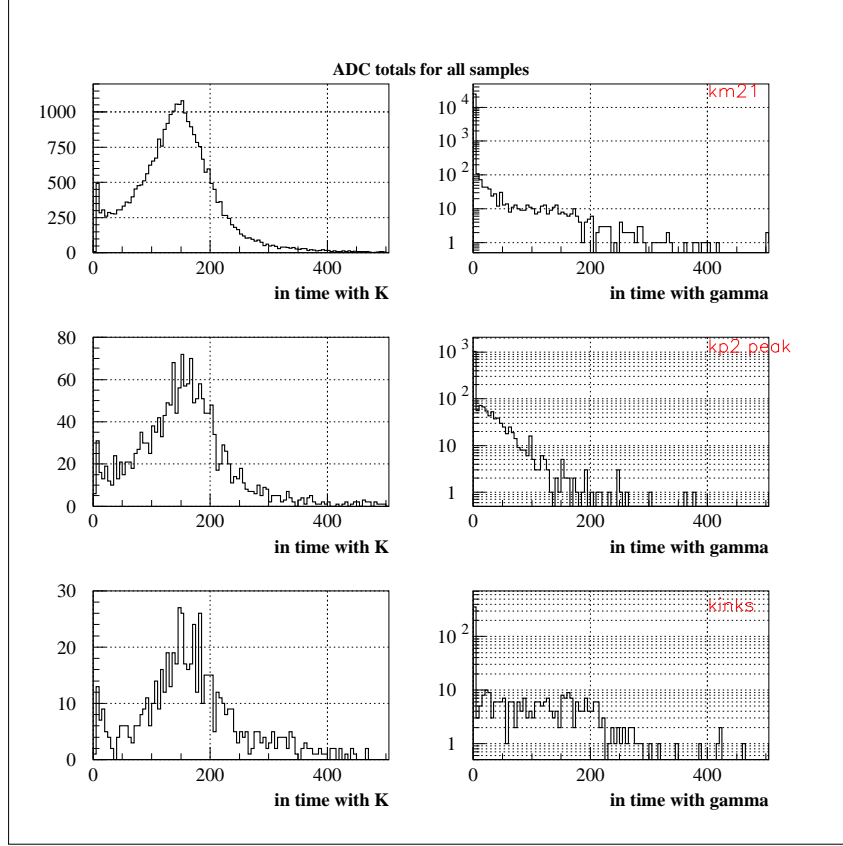


Figure 8.16: Total ADC energy in time with tk ( $\pm 5ns$ , left), and in time with the photon ( $0 - 8ns$  from tpi, right) for  $K_{\mu 2}$  (top),  $K_{\pi 2}$  peak (middle) and kinks (bottom).

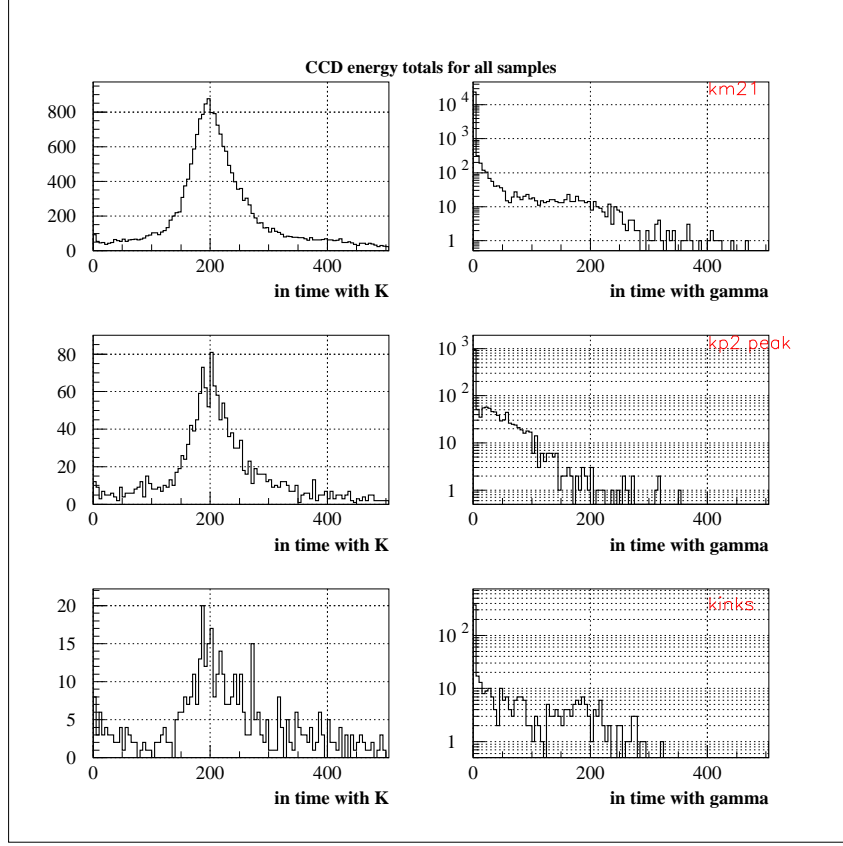


Figure 8.17: Total CCD energy in time with tk ( $\pm 5ns$ , left), and in time with the photon ( $0 - 8ns$  from tpi, right) for  $K_{\mu 2}$ (top),  $K_{\pi 2}$ peak (middle) and kinks (bottom).



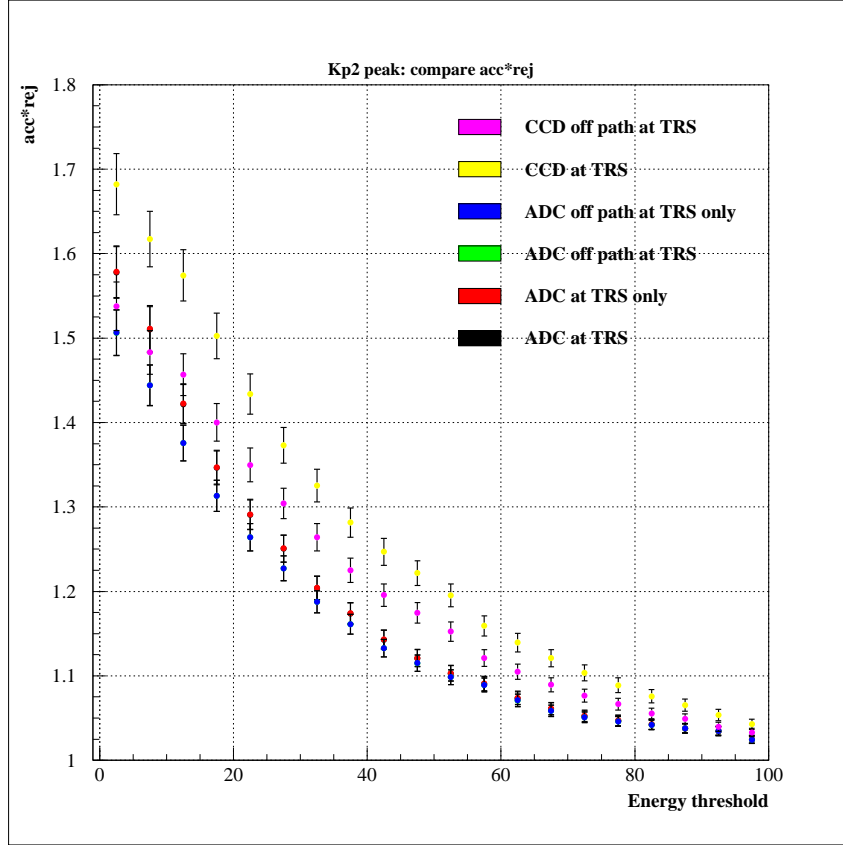


Figure 8.18: Acceptance\*rejection vs total ADC or CCD energy threshold, for  $K_{\pi 2}$  peak events. The different sets of points correspond to ADC cases a-d and CCD cases a-b explained in the text, from bottom to top. The points for ADC cases a and b (black and red), as well as c and d (green and blue), completely overlap.

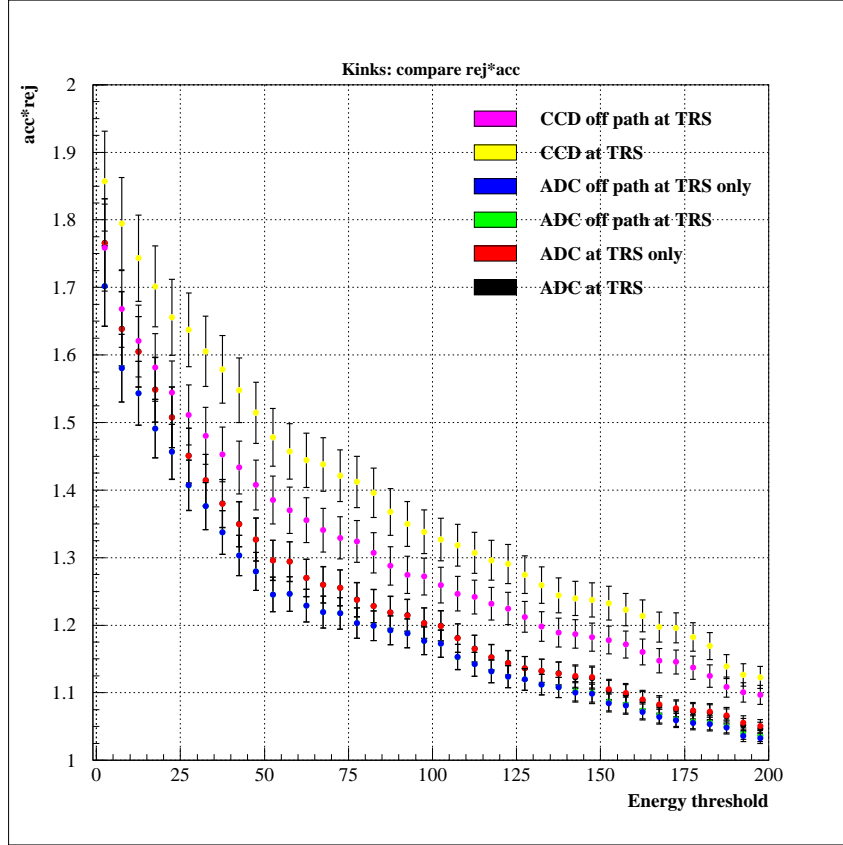


Figure 8.19: Acceptance\*rejection vs total ADC or CCD energy threshold, for different sector selection, for kink events. The different sets of points correspond to ADC cases a-d and CCD cases a-b explained in the text, from bottom to top. The points for ADC cases a and b (black and red), as well as c and d (green and blue), completely overlap.

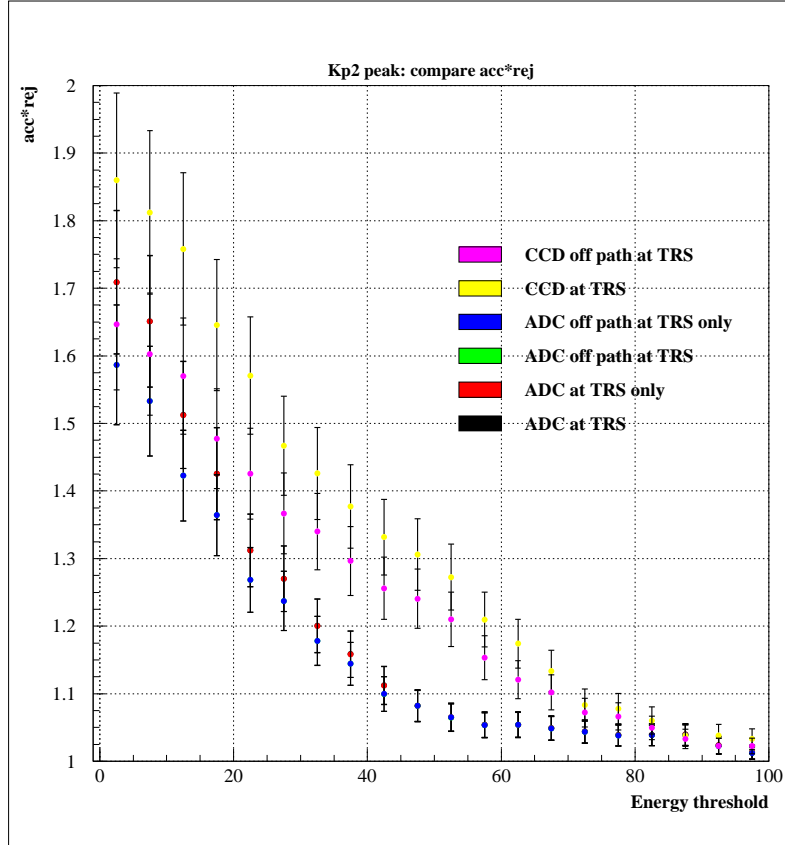


Figure 8.20: Acceptance\*rejection vs total ADC or CCD energy threshold, for  $K_{\pi 2}$  peak events with tight setup PV. The different sets of points correspond to ADC cases a-d and CCD cases a-b explained in the text, from bottom to top. The points for ADC cases a and b (black and red), as well as c and d (green and blue), completely overlap.

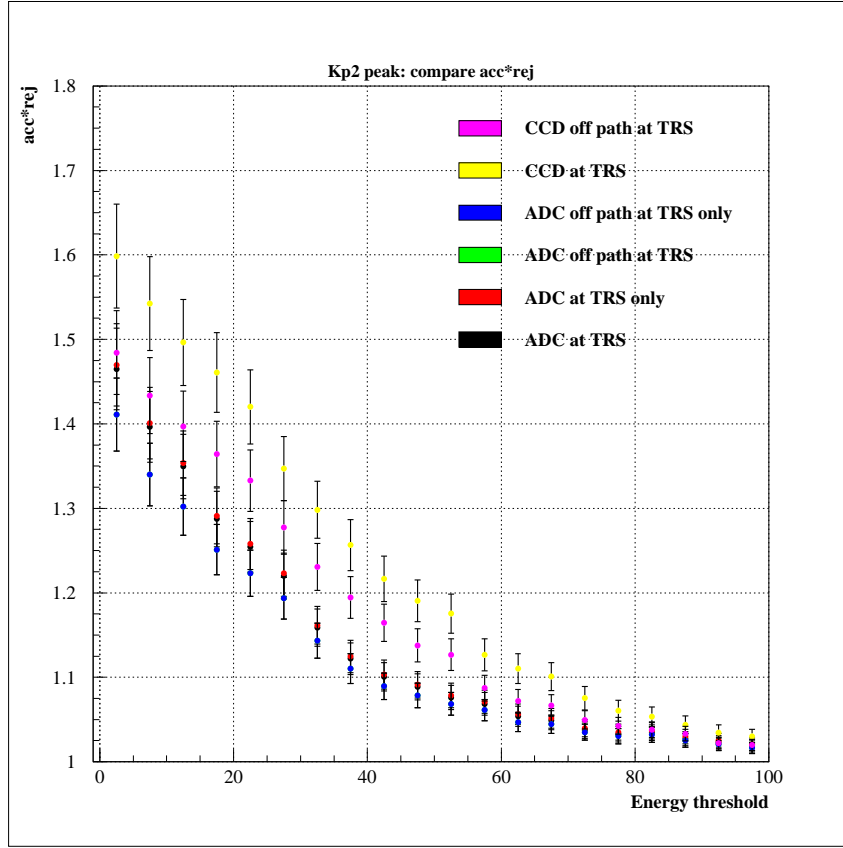


Figure 8.21: Acceptance\*rejection vs total ADC or CCD energy threshold, for different sector selection, for  $K_{\pi 2}$  peak events with tight setup EC1 PV, with the rest of the systems at a loose setting. The different sets of points correspond to ADC cases a-d and CCD cases a-b explained in the text, from bottom to top. The points for ADC cases a and b (black and red), as well as c and d (green and blue), completely overlap.

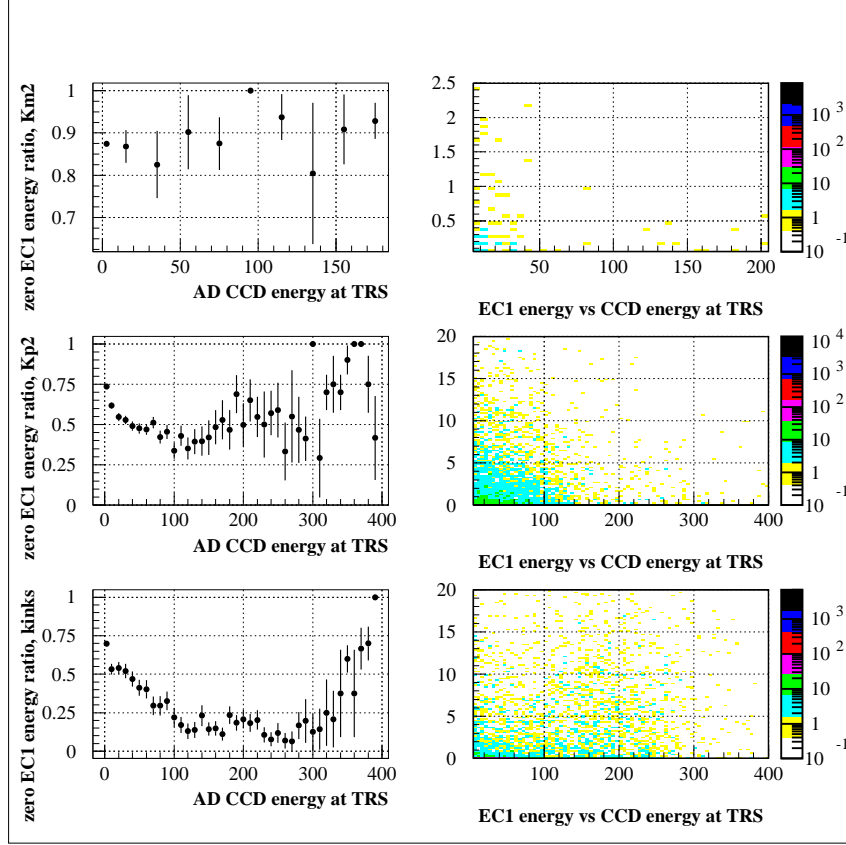


Figure 8.22: Percentage of events with zero energy deposit in the EC1 as a function of energy deposit in the AD (left) and the scatter plots of EC1 energy vs AD CCD energy that these graphs were created from (right), for  $K_{\mu 2}$ (top),  $K_{\pi 2\text{peak}}$  (middle) and kinks (bottom).

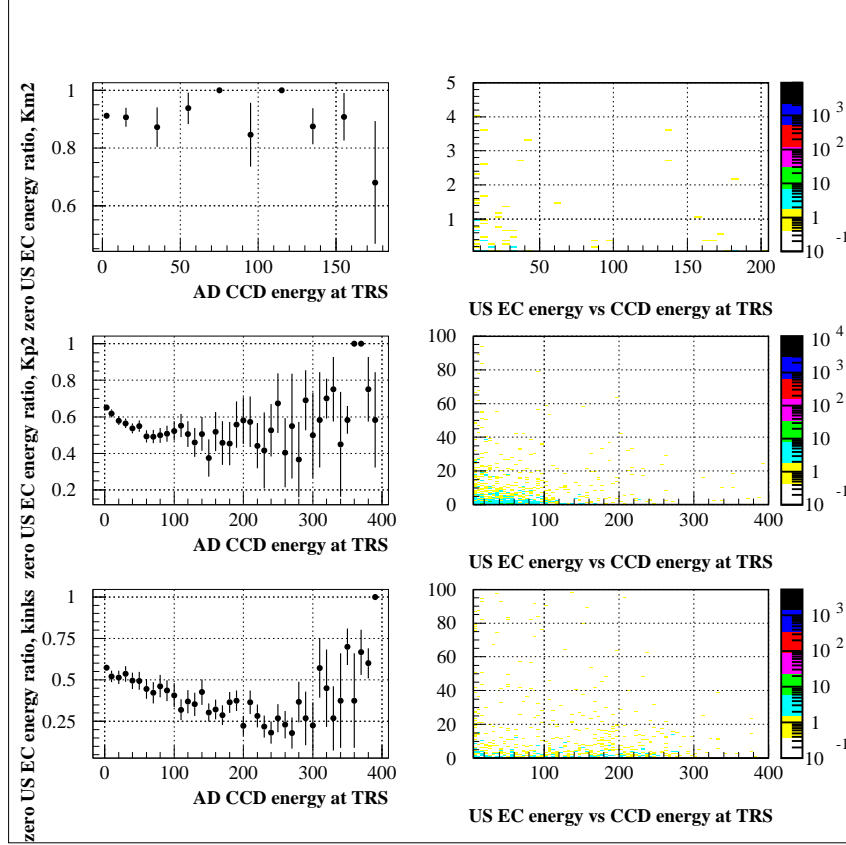


Figure 8.23: Percentage of events with zero energy deposit in the upstream EC (without the inner ring) as a function of energy deposit in the AD (left) and the scatter plots of EC1 energy vs AD CCD energy that these graphs were created from (right), for  $K_{\mu 2}$ (top),  $K_{\pi 2}$ peak (middle) and kinks (bottom).

# Bibliography

- [1] D. Griffiths, “Introduction to elementary particles”, John Wiley & Sons Inc. (1987).
- [2] J.H. Christenson, J.W. Cronin, V.L. Fitch and R. Turlay, Phys. Rev. Lett. **13**, 138 (1964).
- [3] M. Kobayashi and T. Maskawa, Prog. Theor. Phys. **49**, 652 (1973).
- [4] Z. Maki, M. Nakagawa and S. Sakata, “Remarks on the unified model of elementary particles”, Prog. Theor. Phys. **28**, 870 (1962).
- [5] S.L. Glashow, J. Iliopoulos, and L. Maiani, Phys. Rev. **D2**, 1285 (1970).
- [6] N. Cabibbo, Phys. Rev. Lett. **10**, 531 (1963).
- [7] L. Wolfenstein, Phys. Rev. Lett. **51**, 1945 (1983).
- [8] Particle Data Group, W.-M. Yao *et al.*, Journal of Physics G **33**, 1 (2006)
- [9] CKMfitter Group (J. Charles *et al.*), Eur. Phys. J. C41, 1-131 (2005) and <http://ckmfitter.in2p3.fr>
- [10] A.J. Buras, F. Schwab, and S. Uhlig, arXiv:hep-ph/0405132 (2004).

- [11] A.J. Buras, M. Gorbahn, U. Haisch and U. Nierste, arXiv:hep-ph/0603079 (2006).
- [12] W.J. Marciano and Z. Parsa, Phys. Rev. **D53**, 1 (1996).
- [13] Particle Data Group, S. Eidelman *et al*, Phys. Lett. **B592** (2004) 1, and 2005 partial update for edition 2006 available at <http://pdg.lbl.gov>.
- [14] J.S. Hagelin and L.S. Littenberg, Prog. Part. Nucl. Phys. **23**, 1 (1989);
- [15] D. Rein and L.M. Sehgal, Phys. Rev. **D39**, 3325 (1989); M. Lu and M.B. Wise, Phys. Lett. **B324**, 461 (1994); S. Fajfer, arXiv:hep-ph/9602322 (1996); C.Q. Geng, I.J. Hsu, and Y.C. Lin, Phys. Rev. **D54**, 877 (1996).
- [16] A. Belyaev *et al.*, Kaon Physics working Group Report "Kaon Physics with a High-intensity Proton Driver", arXiv:hep-ph/0107046 (2001); G. Isidori, arXiv:hep-ph/0110255 (2001); G. Buchalla, arXiv:hep-ph/0110313 (2001).
- [17] A.J. Buras, arXiv:hep-ph/0402191 (2004); G. Isidori, arXiv:hep-ph/0301159 (2003).
- [18] A.J. Buras *et al.*, arXiv:hep-ph/0402112 (2004); A.J. Buras *et al.*, arXiv:hep-ph/0408142 (2004).
- [19] T. Inami and C.S. Lim, Prog. Theor. Phys. **65**, 297 (1981).
- [20] Y. Grossman and Y. Nir, Phys. Lett. **B398**, 163 (1997).
- [21] B. Bassalleck *et al.*, E949 proposal, BNL-67247, TRI-PP-00-06 (1999), <http://www.phy.bnl.gov/e949/> .



- [22] M.S. Atiya *et al.*, “A Detector to search for  $K^+ \rightarrow \pi^+ \nu \bar{\nu}$ ”, NIM **A321**, 129 (1992).
- [23] V.V. Anisimovsky *et al.*, Phys. Rev. Lett. **93**, 031801 (2004).
- [24] S. Chen *et al.*, “2002  $\pi \nu \bar{\nu}(1)$  Data Analysis”, E949 technical note K-034, 2003.
- [25] T. Yoshioka *et al.*, IEEE Trans. Nucl. Sci. **51**, 199 (2004).
- [26] J. Doornbos *et al.*, Nucl. Instr. Meth. **A444**, 546 (2000).
- [27] D.A. Bryman *et al.*, Nucl. Instr. Meth. **A396**, 394 (1997).
- [28] M. Atiya *et al.*, Nucl. Instr. Meth. **A279**, 180 (1989).
- [29] E.W. Blackmore *et al.*, Nucl. Instr. Meth. **A404**, 295 (1998).
- [30] R.A. McPherson, ”Chasing the Rare Decay  $K^+ \rightarrow \pi^+ \nu \bar{\nu}$ ”, Princeton University, Ph.D. Thesis, November, 1995.
- [31] I.H. Chiang *et al.*, IEEE Trans. Nucl. Sci. **42**, 394 (1995).
- [32] T.K. Komatsubara *et al.*, Nucl. Instr. Meth. **A404**, 315 (1998).
- [33] C. Caso *et al.*, European Physical Journal **C3**, 1 (1998).
- [34] P. Meyers, ”A modified Version of the UMC Multiple Scattering Routine MSCAT1”, E787 Technical Note No.77 (1985). Unpublished.
- [35] A.J. Stevens, ”Nuclear Interactions in CH revisited”, E787 Technical Note No.140 (1987). Unpublished.

- [36] W.R. Nelson *et al.*, "The EGS4 Code System", SLAC 265, SLAC (1985).
- [37] J.B. Birks, Proc. Phys. Soc. **A64**, 874 (1951).
- [38] T. Sekiguchi, 'Measurement of the  $K^+ \rightarrow \pi^+ \nu \bar{\nu}$  Branching Ratio', PhD thesis, 2004.
- [39] B. Bhuyan, 'Search for the Rare Kaon Decay  $K^+ \rightarrow \pi^+ \nu \bar{\nu}$ ', PhD thesis, 2003.
- [40] S. Chen *et al.*, "Further 2002  $\pi \nu \bar{\nu}(1)$  analysis", E949 technical note K-038, 2004.
- [41] V. Jain, 'Simulation of elastic scatters of  $\pi^+$  in the target from Kp2 decays', E787 technical note 375, 1999.
- [42] B. Lewis, "PNN2 1/3 Beam Background", E949 technical note K-061, 2006.
- [43] C. Witzig, " $\pi^-$  absorption in the RS", E787 technical note 278, 1994.
- [44] K. Mizouchi, 'Experimental Search for the Decay  $\pi^0 \rightarrow \nu \bar{\nu}$ ', PhD thesis, 2006.
- [45] Coombes *et al.*, "Tests of prototype E949 beam instrumentation", E949 technical note K-020, 2001.
- [46] D.E. Jaffe, "Estimate of number of photoelectrons in the AD", E949 technical note K-057, 2006.
- [47] B. Lewis, "A new Target Reconstruction and Target Scatter Algorithm", E949 technical note K-063, 2006.

- [48] T. Numao, “Monte Carlo study of the Active Degradar”, E949 technical note K-008, 1999